REMOVAL OF MERCURY FROM WATER BY A REACTIVE ADSORBENT-PYRITE

A Dissertation

by

YUHANG DUAN

Submitted to the Office of Graduate and Professional Studies of
Texas A&M University
in partial fulfillment of the requirements for the degree of

DOCTOR OF PHILOSOPHY

Chair of Committee,	Bill Batchelor
Co-Chair of Committee,	Ahmed Abdel-Wahab
Committee Members,	Qi Ying
	Youjun Deng
Head of Department,	Robin Autenrieth

May 2016

Major Subject: Civil Engineering

ABSTRACT

Pyrite has been demonstrated to be an excellent absorbent in removing mercury in many studies. Most of them used natural pyrites that were ground to micro-scale size or even larger. This study investigated methods to produce nano-scale pyrite particles. $FeCl_3$ and NaSH were used as the source chemicals to synthesize pyrite. Several aging methods, including hydrothermal, ultrasonic and microwave irradiation, were studied in order to reduce the particle size. Surface analysis showed that microwave irradiation was the most effective way to produce near nano-scale pyrite crystals (100-200 nm).

Several experimental variables were investigated in a batch reactor system for mercury removal, including pyrite dose, mercury concentration, and impact of salts and humic acids (HAs). Results of batch experiments revealed an initially fast adsorption kinetics, followed by a release and resorption of mercury behavior. The presence of salts decreased the removal efficiency by about 20%. The mercury loading tests showed that the maximum uptake Hg(II) onto pyrite could reach 900 μmol Hg(II)/ g FeS_2. Both salts and HAs inhibit the removal of Hg(II) by pyrite. But mercury removal increased at higher HAs concentrations. The XPS analysis revealed the presence of HgS on the surface.

A column system was employed to conduct experiments under different pH and hydraulic retention time, in the presence or absence of salts or HAs. The system consists of pyrite-coated sand that was formed by electrostatic attraction or polymers. For

electrostatic attraction/pyrite-coated sand, the removal capacity of mercury decreased at lower influent pH or at lower HRT or in the presence of salts, but faster removal kinetics were observed. HAs slowed the removal of mercury, but the removal capacity was increased as the concentration of HAs increased.

For polymer/pyrite-coated sand, much higher removal capacity was observed. The presence of salts increased the rate of mercury removal, but slightly decreased the amount of mercury removed. However, HAs slower the mercury removal kinetics and lower the total removal capacity of Hg(II).

This study provides fundamental information for a feasible scale-up of the column to produce high quality water from mercury-contaminated water and to produce stable solids for landfill disposal.

DEDICATION

This dissertation is dedicated to my parents and my husband who offered me unconditional love and support throughout my studies.

ACKNOWLEDGEMENTS

I owe my deepest gratitude to my committee, my friends, and my family, without whom this dissertation would not have been possible.

I would like to thank my committee chair, Dr. Bill Batchelor, who provided me an opportunity to be a research group member and let me involved into a great research project, patiently corrected my writing, and financially supported my research which is very important to an international student. Also, thanks to my committee co-chair, Dr. Ahmed Abdel-Wahab, and committee members, Dr. Qi Ying, Dr. Youjun Deng, for their guidance and support throughout the course of this research. They all provided their positive guidance and intellectual background to help push this project to complete on time.

Specially, I would like to acknowledge the research fund for my dissertation, supported by Qatar National Research Fund under National Priorities Research Program.

I would like to extend my gratitude to the staffs in the MCF (Materials Characterization Facility) and MIC (Microscopy & Imaging Center) at Texas A&M University that taught me how to operate spectroscopic instruments. I also would like to thank Dr. Deng's group at Department of Soil & Crop Sciences at Texas A&M University, for XRD analysis. I would like to show my special gratitude to the research group members, Dr. Han Dong Suk, Dr. Xu Liu, Mr. Venkata Sai Vamsi Botlaguduru, Mr. Guofan Luo, and Mr. Li Wang, who shared their ideas and opinions throughout the course of this research, for friendship as well.

I would like to thank my friends, for the exhilarating time we spent together and our great friendship, without whom I would have a boring time.

Also, I would like to thank the department faculty and staff for making my time at Texas A&M University a great experience.

Finally, thanks to my grandfather and my parents for their lovely concerns and encouragement. Thanks also go to my younger brother and my cousins who always provide their best wishes. I would like to extend my gratitude to my husband, who has always taken care of my health and sincere support for me to achieve a Ph.D. degree.

NOMENCLATURE

BET	Brunauer, Emmett and Teller
CAA	Clean Air Act
CVAAS	Cold-Vapor Atomic Absorption Spectroscopy
CWA	Clean Water Act
DI	Deionized
DWEL	Drinking Water Equivalent Level
EDS	Energy Dispersive X-ray Spectroscopy
EPA	Environmental Protection Agency
GFP	Goodness of Fit Parameter
HAs	Humic Acids
HRT	Hydraulic Retention Time
IA	Immunoassay
ICDD	International Center for Diffraction Data
ICP/MS	Inductively Coupled Plasma/Mass Spectrometry
MCL	Maximum Contaminant Level
MCLG	Maximum Contaminant Level Goal
nRA	Nano-scale Reactive Adsorbent
PAA	Polyacrylic Acid
PAH	Polyallylamine Hydrochloride
PMF	Polyelectrolyte Multilayer Films

P/S	Pyrite to Sand ratio
PZC	Point of Zero Charge
RACS	Reactive Adsorbent-Coated Support
RCRA	Resource Conservation and Recovery Act
RfD	Reference Dose
SDWA	Safe Drinking Water Act
SEM	Scanning Electron Microscopy
SSR	Sum of Squared Residuals
TEM	Transmission Electron Microscopy
UHP	Ultra-High Purity
XPS	X-ray Photoelectron Spectrometer
XRD	X-ray Diffraction
XRF	X-ray Fluorescence

TABLE OF CONTENTS

Page

LIST OF FIGURES

Page

LIST OF TABLES

Page

CHAPTER I

INTRODUCTION*

1.1 Background of Mercury

Mercury has aroused great concerns because of its high risks for both the environment and human health. Unlike other elemental metals, pure mercury is a silver-white liquid at room temperature and can volatize to a colorless and odorless gas that has high toxicity. Mercury could be generated by several sources and result in contamination of both atmospheric and aquatic systems. Natural sources of mercury include rocks, crude oil, and natural gas. Cinnabar (mercury sulfide) is one of the prevalent ores that contain mercury.[1] Natural processes such as weathering and sedimentation would release mercury to the environment. Anthropogenic sources of mercury contamination are chlorine production, coal and oil-fired power plants, incinerator facilities, gold mining, and electric arc furnaces.[1-4] Among them, coal and oil-burning power plant are the major sources, contributing 50% of total U.S. mercury emissions as of 2005.[2] Gas-phase mercury will ultimately return to contaminate water resources and land. In water, mercury exists primarily as divalent mercury, and other oxidation states occur depending on redox condition and pH.[5, 6] Mercury generally tends to complex with sulfides (HgS_2^{2-}, $Hg(HS)_2$, HgS_2H^-) in reduced condition, while under oxidized condition, hydroxides

*Part of this chapter is reprinted with permission from Synthesis, characterization, and application of pyrite for removal of mercury by Duan, Y.; Han, D.S.; Batchelor, B.; Abdel-Wahab, A., *Colloids and Surfaces A: Physicochemical and Engineering Aspects* **2016**, *490*, 326-335, Copyright [2016] by Elsevier B.V.

($Hg(OH)^{+}$, $Hg(OH)_{2(aq)}$), chlorides ($HgClOH_{(aq)}$, $HgCl_{2(aq)}$, $HgCl_3^-$), and sulfate ($HgSO_4$) complexes of mercury are the dominant species.[5, 7, 8]

Removal of inorganic mercury is important because most inorganic mercury could be transformed to methylmercury (MeHg) by microorganisms in aquatic ecosystems. Methylmercury is highly toxic and can be bioaccumulated in fish and wildlife via their food chains.[1, 9] Exposure to high levels of methylmercury could lead to death, reduced reproduction, and abnormal behavior of wildlife. It could also cause nervous system damage to unborn babies and young children.[1] Research also shows that mercury exposure at high levels cause damage to the brain, kidney, and immune system and inhibit enzyme activity of people of all ages.[1, 10-12] The Environmental Protection Agency (EPA) classified elemental mercury in cancer group D, which is not classifiable as to human carcinogenicity. No human data indicate that environmental exposures to either inorganic mercury or methylmercury are likely to cause cancer.[13] However, mercury chloride and methylmercury are classified as cancer group C, which means they are possible human carcinogen.[14, 15]

EPA has established regulations, such as the Clean Air Act (CAA), Clean Water Act (CWA), Safe Drinking Water Act (SDWA), and Resource Conservation and Recovery Act (RCRA), to control human exposure to mercury in air, water, and waste. Under RCRA, wastes that contain mercury are classified as "listed hazardous wastes" and cleanup goals are set to prohibit land disposal of contaminated waste or soil.[1] EPA proposed the reference values for inorganic mercury in drinking water that are listed in Table 1.[1, 12, 16]

Table 1.1 EPA reference values for inorganic mercury in drinking water.

Maximum Contaminant Level Goal (MCLG)	0.002 mg/L
Maximum Contaminant Level (MCL)	0.002 mg/L
Reference Dose (RfD)	0.0003 mg/kg/day
Drinking Water Equivalent Level (DWEL)	0.01 mg/L
Life-time Health Advisories	0.002 mg/L

1.2 Analytical Methods

The most common method that is used to analyze mercury in soil and water is cold-vapor atomic absorption spectroscopy (CVAAS). Different modifications of this method have been developed by EPA as EPA/SW-846 Methods 7000A/7470A/7471A.[1, 17] This is the method used in this research to quantitatively analyze mercury. Other primary laboratory analytical procedures for mercury include atomic fluorescence spectrometry using EPA Method 245.7, which can measure total mercury, and inductively coupled plasma/mass spectrometry (ICP/MS) using EPA/SW-864 Method 6020A.[1] Nonaqueous samples usually need to go through a digestion step before analysis.

Other methods, such as immunoassay (IA) test and X-ray fluorescence (XRF), are applicable to the identification and quantitation of mercury in different matrices and are able to greatly reduce analytical times. IA is a method that uses antibodies to bind mercuric (+2) ions in soil and water and uses a color change to quantify concentrations of mercury.[1] XRF is a method that uses the intensity of the energy dispersive X-ray

fluorescence spectra to identify the concentration of mercury on solid media. Both IA and XRF are field-based analytical methods for easy onsite application that can support quicker decision-making.[1]

1.3 Current Treatment Technologies

1.3.1 Bioremediation and Phytoremediation

Popular treatment technologies for mercury removal include biological/biochemical treatment and adsorption. Organic or inorganic mercury can be converted to other species that are accumulated in the biomass or can be easily removed by other treatment technologies, such as precipitation and adsorption.[1, 18-21] For example, strains of *Pseudomonas* are able to convert the soluble ionic form of mercury into insoluble elemental mercury in a reaction that is catalyzed by microbial enzymes generated in the cytoplasm of the bacteria.[1, 18] This process is attractive, because the produced elemental mercury will diffuse out of the cell and collect as small droplets in the medium instead of generating large volumes of mercury-containing biomass.[18] *Escherichia coli* carrying *mer-ppk* fusion plasmid pMKB 18 can convert organic mercury, such as $C_6H_5Hg^+$, to Hg^{2+} using an organomercurial lyase enzyme and then chelate the inorganic ionic mercury (Hg^{2+}) with polyphosphate kinase gene (*ppk*)-specified polyphosphate to form Hg-polyP complex, which can accumulate in the cells.[19, 21]

In addition to bacteria, plants are also able to remove, transfer, stabilize, and destroy mercury in soil and water. The willow species *Salix viminalis* × *S. schwerinii*

can accumulate bioavailable mercury in their roots and thereby limit mercury movement in the rhizosphere.[21] Photoautotrophic macrophytes, including *Scirpus tabernaemontani, Canna indica, Zizania latifolia, Juncus minimus, Cyperus alternifolius, Zantedeschia aethiopica,* and *Acorus calamus* can bioaccumulate mercury in their biomass at a rate of 0.7 μg $kg^{-1}yr^{-1}$.[22] Plants that contain mercuric reductase, which is same as the enzyme in *Pseudomonas* strains, can also reduce ionic mercury to elemental mercury.[18, 21]

Bioremediation and phytoremediation techniques for mercury are both effective methods to remove mercury from various media, but they normally take a long time and require additional monitoring and treatments, such as adsorption and precipitation, to avoid secondary environmental contamination. Also, biological growth may cause fouling problems and phytoremediation is limited to mercury that is bioavailable and present in the root zone.[1, 21]

1.3.2 Abiotic Treatment

Mercury in the aqueous phase could also be removed by various abiotic methods, such as adsorption, precipitation, or combinations of them. Modified active carbon has been widely applied as an effective adsorbent for heavy metals in water and can be regenerated via a thermal process.[23-25] Active carbon is rich in –OH and C=O functional groups, which are the sites for mercury sorption.[23] A low cost activate carbon isolated from agricultural by-product/wastes was found to have aqueous mercury removal capacities ranging from 22.9 mg/g to 25.9 mg/g.[23] Another study investigated active carbon that was modified by sulfur impregnation. It has been demonstrated that

elemental and organic sulfur formed after sulfur impregnation are the active sites for elemental mercury and mercury chloride adsorption.[25] The main reason for this is that Hg(II) species are soft Lewis acids and favor bonding with soft Lewis bases, such as surface sulfur, to form insoluble mercury sulfide species that remain in the pores of the carbon particles.[23, 25]

Many minerals have been proven to be effective mercury adsorbents, including goethite, modified silica, and sedimentary clays that contain high levels of aluminum oxide, iron oxide, and magnesium oxide.[26-29] Goethite showed 70% mercury removal at base conditions and 92% removal in the presence of fulvic acid. The enhancement of removal by fulvic acid could be due to the sulfur groups in fulvic acid.[29] Recent studies applied nanotechnology to prepare adsorbents, such as gold nanoparticles mixed with Al_2O_3, multifunctional magnetic mesoporous silica nanocomposites, titanium oxide nanoparticles, and magnetic silica nanocomposites. They all have high specific surface area, have high affinity toward mercury,[30-33] and most of them could be easily regenerated and have excellent recyclability.[30, 31]

1.4 Background of Mercury Removal by Iron Sulfides

Sulfur groups enhance the removal of mercury[25, 29] and sulfide minerals play important roles in controlling dissolved metal concentrations in anoxic environments.[34-36] Pyrite (FeS_2), commonly known as "Fool's Gold", is the most abundant metal sulfide on the surface of the earth and has been chosen as a reactive absorbent in this research for mercury immobilization. Previous studies demonstrated that pyrite and other iron

sulfides species, such as mackinawite (FeS), have strong adsorption capability for mercury.[37-42] Since nanoparticles provide high specific surface area and thus high adsorption capacity, methodologies for synthesis of nano-scale pyrite were investigated.

Mercuric ions are soft Lewis acids, they have a strong affinity for soft Lewis bases, such as reduced-S ligands.[23, 37, 40, 43] Therefore, insoluble mercury sulfides species or surface complexes of mercury and reduced-S ligands are expected to form and the resulting mercury-laden solids could be removed by filtration. Studies have shown that both surface precipitation and adsorption of mercury can occur on the surface of pyrite.[34] At acidic pH, the pyritic site (≡S-H) is the dominant functional group on the surface of pyrite. After mercury is sorbed onto this site, it forms surface complexes, such as ≡S-Hg-Cl and ≡S-Hg-OH.[34, 37, 44] At alkaline pH, the surface of pyrite is oxidized and covered by a layer of Fe (III) oxyhydroxide.[40, 44] The oxyhydroxide site (≡O-H) is the major function group on the pyrite surface at basic pH and produces more complex aqueous chemistry.[27, 40, 44] One hypothesis for mercury removal under this situation is that mercury goes into the interface of pyrite-oxyhydroxide and forms surface complexes between mercury and both pyritic and oxyhydroxide sites.[37, 44] Some X-ray photoelectron spectrometer (XPS) studies of mercury sorption onto pyrite point out that the formation of HgS is excluded due to the absence of S(II) on S 2p spectra.[44]

Excess soluble HS^- can convert some of the insoluble mercury species into soluble mercury-sulfide species, which would increase the concentration of mercury in solution. If elemental sulfur were also present, polysulfides would form and that would

form soluble mercury-polysulfide complexes.[39, 45-47] The typical reactions are described in Reaction 1.1-1.5.[45, 47]

$$HgS(s) + HS^- \rightarrow HgS_2^{2-}(aq) + H^+ \quad (1.1)$$

$$HgS(s) + HS^- \rightarrow HgS_2H^-(aq) \quad (1.2)$$

$$HgS(s) + HS^- + 2(x-1)S(0) \rightarrow Hg(S_x)_2^{2-}(aq) + H^+ \quad (1.3)$$

$$HgS(s) + HS^- + (x-1)S(0) \rightarrow Hg(S_x)(SH)^-(aq) \quad (1.4)$$

$$HgS(s) + (x-1)S(0) + H_2O \rightarrow Hg(S_x)OH^-(aq) + H^+ \quad (1.5)$$

Although pyrite has been demonstrated to be an excellent absorbent for removing mercury from water and to form stable residuals, such as solid precipitates, the pyrites used in those studies are all of macro-scale size or even larger,[34, 37, 39, 40, 44, 47, 48] which limited the removal capacity for mercury. In this research, we developed methods and techniques to produce pyrite particles that were nearly at the nano-scale, which can be described as nano-scale reactive adsorbent (nRA)-pyrite. These particles can not only remove mercury by adsorption, but also produce stable forms (mercuric sulfides) for ultimate disposal. Small particles provide more surface area, which results in greater sorption capacity that would improve mercury removal efficiency. In order to provide good contact with the water being treated, pyrite particles were coated onto sand, which operates as a macro-sized support media. This reactive adsorbent-coated support (RACS) system was developed to treat mercury-containing water in the presence of salts ($NaNO_3$, Na_2SO_4) or humic acids (HAs).

1.5 Background of Coating Methods

Mercury-containing nano-scale pyrite in suspension should not be allowed to flow out of a treatment system with the treated water. One approach for retaining synthetic pyrite particles within the treatment system would be to attach them to larger particles, such as sand. One method of attaching particles to the surface of a support media is through electrostatic forces. Studies investigating the coating of silica sand with goethite found that the maximum adsorption of goethite occurred around pH 7.9, which is the point of zero charge (PZC) of pure goethite. The amount of goethite sorbed to the sand increased as the pH increased up to the pH_{pzc}, while the amount of goethite sorbed decreased sharply when the pH was increased beyond the pH_{pzc}.[49] Han et al. (2011) have successfully coated FeS on both untreated sand and chemically-treated sand at pH 5.5, which is the PZC of FeS.[50] The amount attached to the sand decreased at pH greater or less than pH 5.5. Both cases indicate that pH is a critical factor for optimal coating. This is true because the surface charges on both the smaller particles (goethite, iron sulfide) and the larger particle (sand) change as pH changes.[49, 50] Both silica sand and goethite have negative surface charge at pH higher than their pH_{pzc}, which will lead to repulsion between sand and goethite particles.[49] Furthermore, aging time and initial concentration could also affect coating efficiency, but they are not as important as pH.[50, 51] The other method for attaching nano-scale pyrite particles to sand particles uses a polymer-based coating and leads to formation of polyelectrolyte multilayer films (PMF) to incorporate nanoparticles. The polyelectrolytes are charged, water-soluble macromolecules and in the presence of oppositely charged substrate, they could form a uniform film of polymer,

layer by layer. The layer-by-layer adsorption could immobilize the nanoparticles on the surface of the sand.[52-54]

1.6 Research Objectives and Methodology

The overall goal of this research is to investigate interactions between pyrite and mercury under anoxic conditions in order to better understand mercury removal and its behavior in treatment systems, and to develop the RACS system into a successful technology to produce high quality water from mercury-contaminated wastewater, while producing stable final residuals. To achieve this goal, four experimental tasks will be accomplished as follows.

1.6.1 Task 1. Develop Experimental and Analytical Procedures

The analytical method for mercury should be sufficiently sensitive, accurate and precise to achieve the goals of this research. The analytical method for mercury was CVAAS, in which mercury is reduced to the elemental form before AAS analysis. The method detection limit, accuracy and precision of the CVAAS method were measured. A RACS reactor was set up with a glass column that is designed to contain the pyrite-coated sand. Surface analysis techniques, including X-ray Diffraction (XRD), X-ray Photoelectron Spectrometer (XPS), Scanning Electron Microscopy (SEM)/Energy Dispersive X-ray Spectroscopy (EDS), and Transmission Electron Microscopy (TEM), were applied to solid phases (pyrite, sand, pyrite-coated sand) before and after contact with mercury. These analyses determined surface morphology and ion composition as

well as identify functional groups on the surface and the oxidation states of surface elements.

1.6.2 Task 2. Develop Techniques to Produce Nano-Scale Reactive Adsorbent and to Produce Reactive Adsorbent-Coated Support (RACS) System

Ferric chloride ($FeCl_3$) and sodium hydrosulfide (NaSH) were used as iron and sulfur sources to synthesize pyrite.[55, 56] Different temperatures, aging times, and levels of energy input (hydrothermal, ultrasonic, and microwave[43]) were studied for their ability to form pyrite particles that are less than 200 nm. Particle size is an important factor that would affect performance in a treatment system. Different energy inputs could increase the rate of nucleation, which is the key factor affecting formation of smaller particles.[43, 56] The surface of synthesized pyrite was characterized by XRD, XPS, SEM/EDS, and TEM/EDS to choose the best synthetic methodology.

The RACS system was produced by attaching pyrite to the surface of sand through electrostatic attraction and polymer-based coating. The sand was washed with DI water, sodium dithionite, concentrated HCl, and H_2O_2 in order to remove any natural minerals and impurities that were on the sand surface.[50] Washing effects were evaluated by results of XRD, SEM/EDS. The pH effect and different ratios of pyrite to sand were used to investigate the coating efficiency.

Since Han et al. (2011) successfully coated FeS on sand and FeS is a precursor of pyrite, it may be possible to form pyrite on the surface of the sand.[50] FeS could be transformed to pyrite at high temperature, so pyrite would form on the surface of FeS-

coated sand via microwaving or heating. The other method to be investigated is an in-situ incorporation technique that uses a polymer-based coating and leads to formation of polyelectrolyte multilayer films (PMF). Polyacrylic acid (PAA) was used for the first layer and polyallylamine hydrochloride (PAH) was used for the second layer.[53] Solubility of pyrite attached to the sand was evaluated by measuring the concentration of Fe or S in solution after contact with solutions at pH 5, 7, and 9. The surface of pyrite-coated sand was characterized by SEM/EDS.

1.6.3 Task 3. Characterize Effects of Time and Initial Concentration on Removal of Mercury by Pyrite

Batch experiments were conducted with synthesized pyrite in order to investigate effects of time and pyrite dose on mercury removal. In the kinetic tests, the effects of pyrite dose (0.1 g/L and 0.01 g/L) and background salts (0.01 mol/L $NaNO_3$ and Na_2SO_4) were evaluated at pH 8. The Hg(II) concentration was measured at 10 sampling times (5 min, 10 min, 20 min, 30 min, 1 hr, 2 hrs, 3 hrs, 6 hrs, 12 hrs, and 24 hrs). In tests to evaluate the effect of concentration on adsorption capability of pyrite, 10 initial mercury concentrations were used that ranged from 1 mg/L to 100 mg/L. These tests used a 0.1 g/L dose of pyrite in a solution at pH 8 with samples taken after 1, 3, and 7 days. The effects of background salts (0.01 mol/L $NaNO_3$ and Na_2SO_4) and humic acids (5, 10, 20 mg/L) were evaluated. Values of pH were recorded for each sample. Surface characterization of selected mercury-containing pyrite samples after concentration-effect removal tests were investigated with SEM/EDS and XPS.

1.6.4 Task 4. Characterize Column-Based Mercury Removal

The kinetics of mercury removal by the RACS system were evaluated at different pH (5, 7, 9), hydraulic retention times (HRT), in the presence or absence of salts (0.01 mol/L $NaNO_3$ and Na_2SO_4) and humic acids (10, 20 mg/L). Mercury in the liquid-phase was determined by CVAAS, while the solid-phase was characterized by XPS and SEM/EDS.

The dissertation is organized as follows: Chapter 2 describes the methodology of synthesis of near nano-scale pyrite and surface characterization of synthetic pyrite. Chapter 3 focuses on kinetic removal of mercury by synthesized pyrite in batch sorption experiments. Chapter 4 presents the methodology of attaching pyrite to the surface of sand through electrostatic attraction and polymer-based coating and surface characterization of pyrite-coated sand. Also, the kinetics of mercury removal by the RACS system under different pH, HRT, and in the presence or absence of salts or humic acids were studied in Chapter 4.

CHAPTER II

SYNTHESIS AND CHARACTERIZATION OF PYRITE*

2.1 Introduction

Pyrite (FeS_2), commonly known as "Fool's Gold", is the most abundant metal sulfide on the surface of the earth and has been chosen as a reactive absorbent in this research for mercury immobilization.[57-59] Marcasite is a dimorph of pyrite, which has the same chemical composition as pyrite but has a different crystal structure. Pyrite has a NaCl-derivative structure with the FeS_6 octahedra linked at their apices by S-S bonds, while in marcasite the FeS_6 octahedra are linked along edges by 2 S-S bonds. Pyrite and marcasite commonly occur together.[60, 61] In natural systems, pyrite is formed in anoxic sediments or sedimentary rocks from the reaction of reactive detrital iron minerals and dissolved sulfide.[62, 63] Roberts et al. (1969) pointed out that pyrite in sediments is formed predominantly by direct reaction of ferrous iron and disulfide.[58] However, disulfide ion is not prevalent in natural waters. Research by Schoonen and Barnes (1991) further demonstrated that the formation mechanism described by this hypothesis was insignificant.[64] Later, several studies suggested that the main mechanism of pyrite formation in sediments is the transformation of iron monosulfide (FeS) precursors.[62, 63] Aqueous hydrogen sulfide ($H_2S_{(aq)}$), which formed mainly by bacterial reduction of dissolved sulfate, plays an important role in pyrite formation. $H_2S_{(aq)}$ could react with

*Part of this chapter is reprinted with permission from Synthesis, characterization, and application of pyrite for removal of mercury by Duan, Y.; Han, D.S.; Batchelor, B.; Abdel-Wahab, A., *Colloids and Surfaces A: Physicochemical and Engineering Aspects* **2016**, *490*, 326-335, Copyright [2016] by Elsevier B.V.

various detrital iron-bearing minerals to form iron sulfides (Reaction 2.1), including amorphous FeS ($Fe_{1.09}S$-$Fe_{1.11}S$),[59] mackinawite ($FeS_{0.93}$-$FeS_{0.96}$),[59] and greigite (Fe_3S_4). Unstable amorphous FeS and the FeS component of mackinawite (expressed as FeS* in reaction) would be finally transformed to pyrite.[62] There are two transformation mechanisms that have been offered. One is the reaction between iron monosulfide and sulfur (Reaction 2.2, S° represents a source of sulfur).[62, 65] The other is the rejection of iron from iron monosulfide (Reaction 2.3).[59]

$$Fe^{2+} + H_2S_{(aq)} \rightarrow FeS^*(s) + 2H^+ \quad (2.1)$$

$$FeS^*(s) + S^\circ \rightarrow FeS_2 \quad (2.2)$$

$$2FeS^*(s) + 2H^+ \rightarrow FeS_2(s) + Fe^{2+} + H_2 \quad (2.3)$$

Another pyrite formation mechanism was proposed by Rickard (1975), who stated that pyrite was formed directly by reaction between dissolved ferrous ion and polysulfide ions (Reaction 2.4).[65, 66] Ferrous ion and polysulfide ions (S_n^{2-}) are produced by dissolution of FeS and reaction of elemental sulfur and dissolved sulfide (Reaction 2.5), respectively.[65-67]

$$Fe^{2+} + S_n^{2-} + HS^- \rightarrow FeS_2 + S_{n-1}^{2-} + H^+ \quad (2.4)$$

$$(n-1)S^0 + HS^- \rightarrow S_n^{2-} + H^+ \quad (2.5)$$

In addition, Luther (1991) proposed that both solid FeS and the soluble complex $Fe(HS)^+$ could act as precursors for pyrite formation and could directly react with polysulfide to form pyrite,[68] as shown in Reaction 2.6 and 2.7.[65, 67-69]

$$FeS + S_n^{2-} \rightarrow FeS_2 + S_{n-1}^{2-} \quad (2.6)$$

$$Fe(HS)^+ + S_n^{2-} \rightarrow FeS_2 + S_{n-1}^{2-} + H^+ \quad (2.7)$$

It takes years for pyrite to form in natural systems, but in the laboratory, pyrite can be synthesized in days or even minutes. Pyrite formation in solution below 100°C could occur via either nucleation of FeS_2 or via FeS precursors.[59, 64] The rate of FeS_2 nucleation was insignificant below 100°C under acidic condition,[64] but pyrite nucleation could be accelerated over several months in the presence of metastable iron sulfides.[67] Formation of pyrite from a FeS precursor was successful. With the aging temperature below 100°C, pyrite formed gradually from amorphous FeS and mackinawite under alkaline conditions, but much faster in acidic solution with marcasite as the predominant product.[59, 60] In addition, pyrite would not be formed when hydrogen sulfide or bisulfide is the only sulfur source.[59] However, formation of pyrite took only several minutes when the temperature of the solution was increased up to 150°C in the presence of elemental sulfur or polysulfides.[70] Pyrite would be formed even with only hydrogen sulfide or bisulfide present within 1 hour at 300°C.[70] More recently, Wei and Osseo-Asare (1996) demonstrated that pyrite particles with an average size of 1.5 μm were produced at room temperature with $FeCl_3$ and NaHS in the pH range of 3.6-5.7 in 5 days. With pH below 3.6 or above 5.7, pyrite was barely formed due to the availability of FeS precursor.[55]

The goal of this research is to evaluate a variety of synthesis methods that would produce smaller pyrite particles in a short time. These synthesis methods were modifications of the method of Wei and Osseo-Asare' (1996). Ferric chloride and sodium hydrosulfide were also chosen as iron and sulfur sources to synthesize pyrite, but different aging times and aging methods, including hydrothermal, ultrasonic, and microwave, for pyrite formation were investigated.

2.2 Materials and Methods

2.2.1 Anaerobic Condition

All experiments and related work were conducted in an anaerobic chamber (Coy Laboratory Products Inc.) that was filled with ultra-high purity (UHP) nitrogen. The anaerobic chamber was vacuumed and refilled with nitrogen gas once the door was opened in order to keep the anaerobic conditions inside the chamber. The deionized water (Milli-Q, Millipore) used in all experiment was deoxygenated by sparging with UHP nitrogen for 2 hours outside the chamber and then for 24 hours inside the chamber.

2.2.2 Methodology for Pyrite Synthesis

Iron(III) chloride hexahydrate (97%, Sigma-Aldrich) and sodium hydrosulfide hydrate (Sigma-Aldrich) were used as iron and sulfur sources to synthesize pyrite.[55, 56] Different temperatures, aging times, and levels of energy input (hydrothermal, ultrasonic, and microwave[43, 61]) were studied for their ability to form pyrite particles that are less than 200 nm.

Pyrite particles were synthesized by mixing 15 mL of 0.1 mol/L $FeCl_3$ with 15 mL of 0.2 mol/L NaHS and adding sufficient 1 mol/L NaOH to achieve pH 4.5. For hydrothermal aging, a stirrer/hotplate (Corning) was used to keep the mixture at 60°C for 24 hours. Several ultrasonic methods were investigated, including sonication of the mixed solution with 60°C water bath for 3 hours with a sample taken every 1 hour (which is called U1); sonication of the mixture directly in the bath of the sonicator (Branson 5210) without any container for 3 hours (which is called U2); sonication of the

synthetic pyrite suspension (dry pyrite particles were suspended in deoxygenated DI water) for 7 hours and vacuum filtered the suspension to obtain the solids (which is called U3); Sonication of mixed $FeCl_3$ and NaHS solution for 6 hours (which is called U4). For microwave aging, a commercial microwave (Emerson MW8779W, output 800 W, 2450 MHz) was used with six combinations of power levels and reaction times (20% power for 2 min, 4 min, and 6 min, respectively, 40% power for 2 min, 60% power for 1 min, and 100% power for 1 min). A microwave digestion bomb (45 mL, Parr Instrument Company) was used as the container to avoid possible explosion due to the high pressure and temperature. After aging, 10 mL concentrated HCl (J.T. Baker) was added to the mixture to dissolve excess FeS without destroying crystalline pyrite.[62] Then, the solid phase was collected by vacuum filtration with a 0.02-μm anodisc type 13 membrane filter (47 mm-diameter, Whatman) and washed several times with acetone (99+%, Alfa Aesar) and carbon disulfide (J.T. Baker) to removal residual sulfur from the solid surface.[43] Then, the synthesized solids were dried in the anaerobic chamber.

The specific surface area of selected sample was determined using N_2 adsorption and applying the Brunauer, Emmett and Teller (BET) theory at 77.4 K.

2.2.3 Microscopic and Spectroscopic Characterization of Pyrite

The synthesized pyrite was characterized by XRD (Department of Soil & Crop Sciences, TAMU), XPS (Materials Characterization Facility, TAMU), SEM/EDS (Materials Characterization Facility, TAMU), and TEM/EDS (Microscopy & Imaging Center, TAMU). The X-ray diffraction patterns of the samples were recorded on a D8

Bruker Advance X-ray diffractometer (XRD) with Cu Kα X-ray radiation. The measured XRD data were compared to International Center for Diffraction Data (ICDD) database.

A Kratos (Manchester, UK) Axis Ultra X-ray Photoelectron Spectrometer (XPS) with a monochromatized Al-Kα (1253.6 eV) source was used to obtain the oxidation status of Fe, S, O, and C, and the chemical composition of the surface of pyrite. The survey scans were recorded with pass energy of 160 eV and the narrow scans used 40 eV for higher resolution. The spectra peak of C 1s with a binding energy of 284.5 ± 0.1 eV was used as a reference to correct expected charging effects. The narrow scan spectra of Fe 2p, S 2p, and O 1s were fitted with XPSPEAK41 fitting program with a Gaussian-Lorentzian peak function through background-subtraction corrections using a Shirley or Linear-type optimization.

A scanning electron microscopy (SEM) equipped with an energy dispersive x-ray spectroscopy (EDS) (JSM-7500F, Tokyo, Japan) was utilized to study the morphology and chemical composition of synthesized pyrite. The image was collected at a working distance of 15 mm or 8 mm under acceleration voltage range of 3 kV to 7 kV at a magnification of 10,000×.

A transmission electron microscopy (TEM) equipped with EDS (JEOL JEM-2010, Tokyo, Japan) was also used to study the morphology and chemical composition of pyrite. The solid sample was suspended in ethanol under sonication and then placed on a carbon film on 400-mesh copper grid (Electron Microscopy Sciences) for analysis.

2.3 Results and Discussion

2.3.1 Yield

After being dried in the chamber, the pyrite particles were collected and the weights were recorded as listed in Table 2.1. Aging method U1 (1 hour) did not generate any pyrite and all particles were amorphous and dissolved in concentrated HCl. Higher yields were observed with hydrothermal and ultrasonic aging methods, but the aging times required to produce particles were much longer than those with microwave irradiation. Microwave irradiation accelerated the rate of pyrite formation and reduced the aging time to a few minutes but with much lower yield of pyrite. It has been reported that pyrite could be efficiently decomposed to highly porous pyrrhotite-like Fe-S phases and elemental sulfur (Reaction 2.8) when exposed to microwave. And the decomposition rate increased with microwave irradiation time.[61] Therefore, shorter aging times were applied for those higher microwave irradiation power levels in order to minimize decomposition of pyrite.

$$(1\text{-}x)\ FeS_2 \rightarrow Fe_{1-x}S + (1\text{-}2x)\ S^0 \qquad (2.8)$$

2.3.2 Surface Characterization for Hydrothermal Synthesized Pyrite

The dry particles produced by the hydrothermal methods were characterized by SEM/EDS, XRD, and XPS. The particles analyzed by SEM/EDS had an octahedral or cubic shape, as shown in Figure 2.1 (a). The morphology of pyrite has been reported to change from cubic to octahedral to spherulitic with increased degree of supersaturation of the solution.[67] However, the size of the particles was around 1 μm, which is much

larger than the goal. Figure 2.1 (b) shows the EDS spectra of the sample and indicates that the Fe to S ratio was around 1:2, which confirmed pyrite in the sample.

Table 2.1 Particle production by various synthesis methods.

Preparation Method	Description	Ratio of Mass Produced to Theoretical (%)
Hydrothermal	Replicate 1, 24 hrs	45.0
	Replicate 2, 24 hrs	42.8
	Replicate 3, 24 hrs	42.8
	Replicate 4, 24 hrs	42.8
	Replicate 5, 24 hrs	40.0
Ultrasonic	U1 1 hr	0
	U1 2 hrs	42.8
	U1 3 hrs	45.6
	U1 2 hrs + another 19 hrs hydrothermal	45.6
	U1 3 hrs + another 19 hrs hydrothermal	46.1
	U2	31.1
	U4	47.8
Microwave	20% power, 2 min	2.2
	20% power, 4 min	38.3
	20% power, 6 min	37.2
	40% power, 2 min	36.7
	60% power, 1 min	32.8
	100% power, 1 min	36.7

The XRD pattern indicates that both pyrite and marcasite were present in the sample with a rough ratio of 1:1, as shown in Figure 2.2. The presence of marcasite is reasonable since marcasite occurs mainly at pH below 5.[59, 60] There were no other solid phases identified.

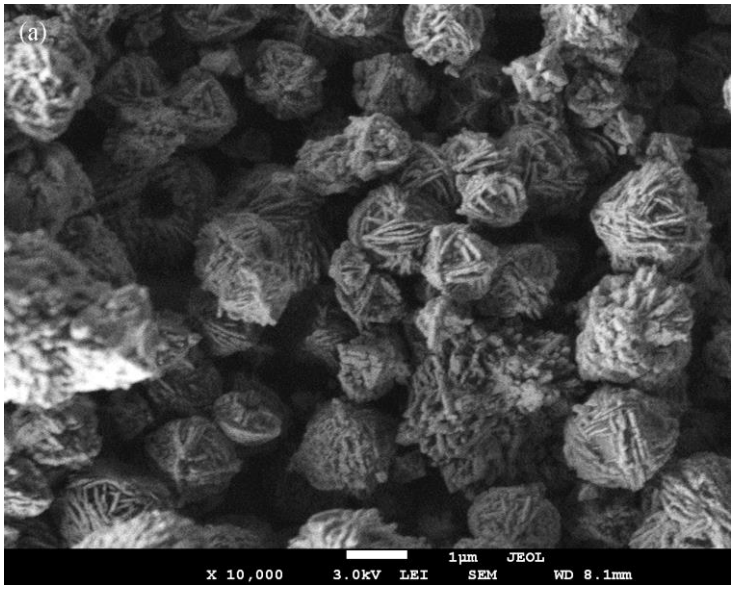

Figure 2.1 (a) SEM image, (b) EDS spectra of particles produced by the hydrothermal method.

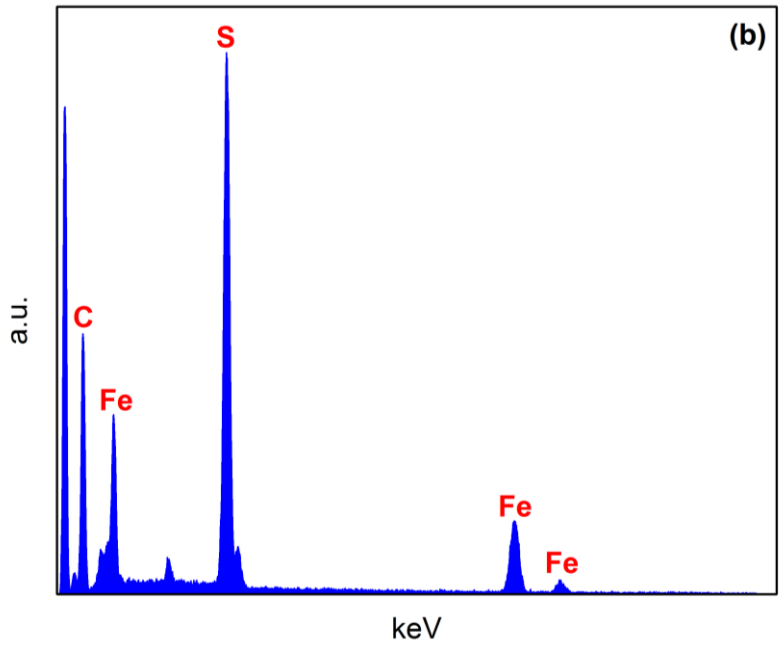

Figure 2.1 Continued.

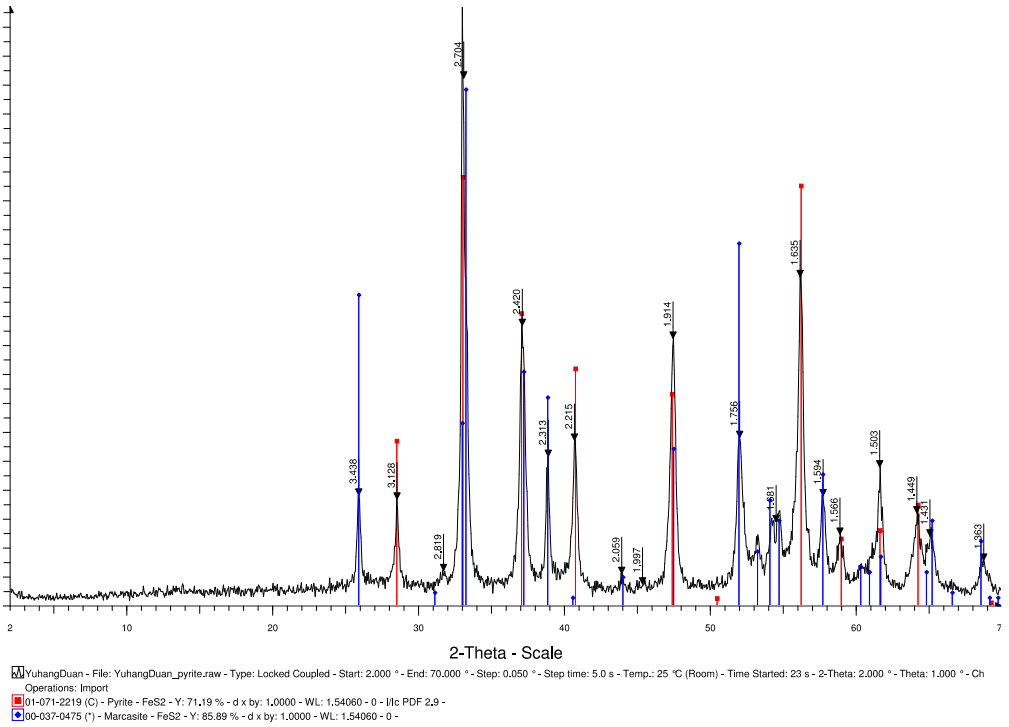

Figure 2.2 XRD patterns of hydrothermal synthesized particles.

XPS analysis of the sample using broad and narrow scans was also done to investigate the surface species. The broad scan of the sample, as shown in Figure 2.3, reveals that the surface of the particles contains iron, sulfur, oxygen, and carbon. Carbon was mainly from the carbon tape, which was used to hold particles on the sample holder. Sulfur to iron atomic concentration ratio was found to be around 2.6 (Table 2.2). The particles were mainly pyrite with a small amount of elemental sulfur or other sulfur-containing compounds.

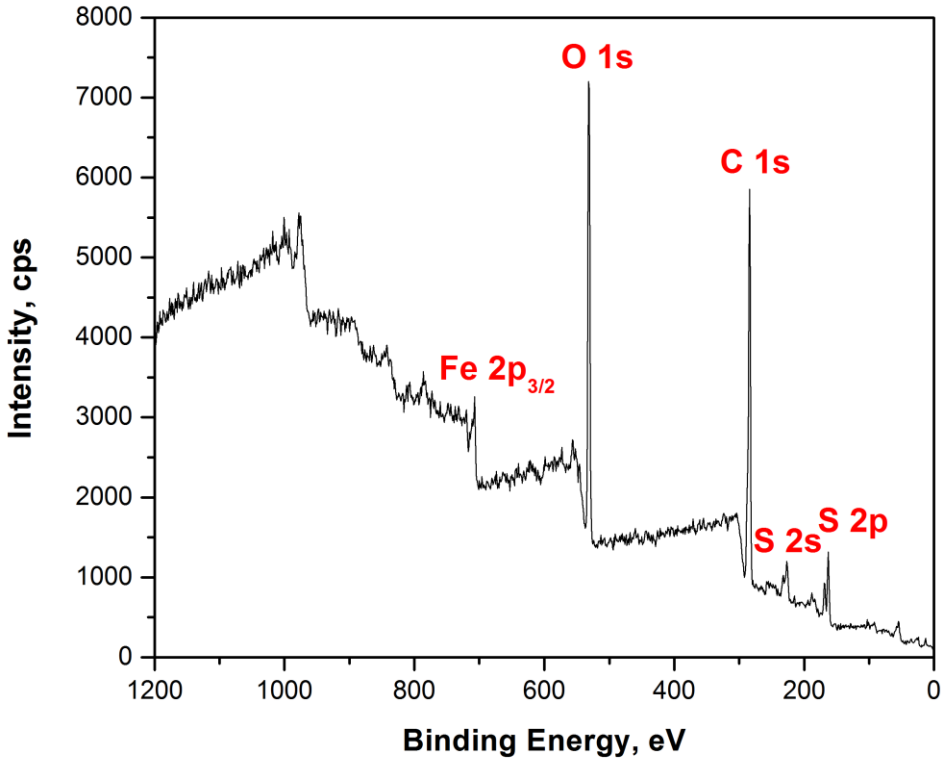

Figure 2.3 XPS Broad scan of particles produced by the hydrothermal method.

Table 2.2 Atomic concentration of particles produced by the hydrothermal method.

Atomic Concentration %			
Fe 2p	O 1s	C 1s	S 2p
2.87	27.69	61.98	7.45

Figure 2.4 shows the Fe 2p and S 2p spectra of the particles obtained by narrow scans and the parameters for the peaks are shown in Table 2.3. The XPS data were fitted using a curve-fitting program called XPSPEAK41. The binding energy at 707.34 eV and

162.59 eV are two major peaks of Fe $2p_{3/2}$ and S $2p_{3/2}$ spectra, and were identified to be the characteristic peaks of pyrite.[57, 71-73] The other two smaller peaks in the Fe 2p spectra at 709.66 eV and 711.75 eV represent FeO/Fe(III)-S and Fe(OH)O/$FeCl_3$, respectively.[71, 74] The peak at 163.75 eV in the S 2p spectra indicates the presence of polysulfide or elemental sulfur and the peak at 168.88 eV indicates the presence of a sulfate compound.[57, 71, 73] These two narrow scan spectra indicate that the surface of pyrite might be slightly oxidized as shown by the presence of oxidized iron and sulfur.

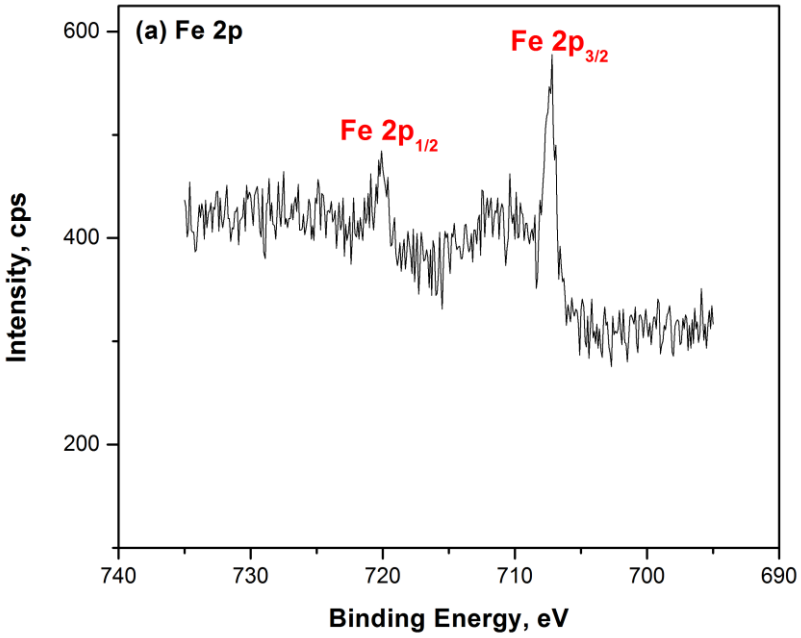

Figure 2.4 XPS spectra of particles produced by the hydrothermal method (a) Fe 2p. (b) S 2p.

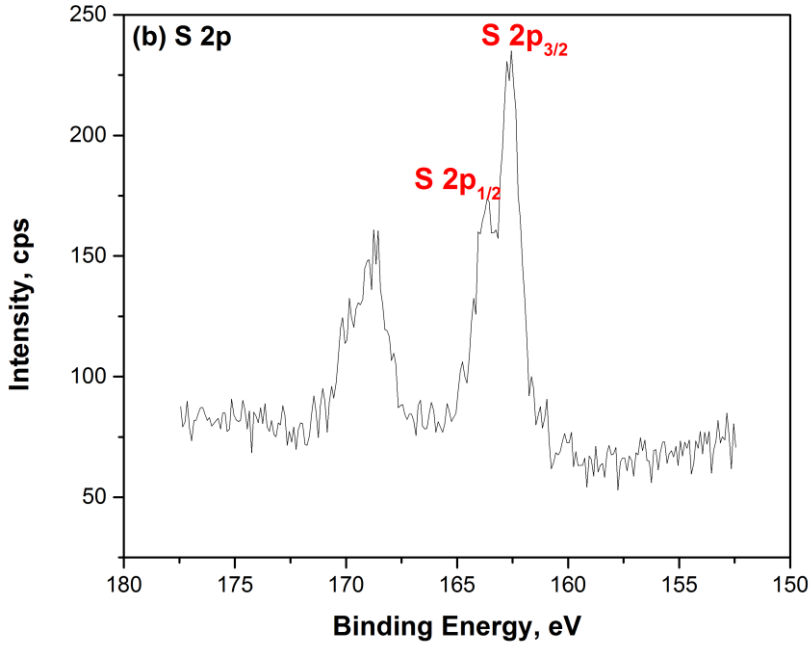

Figure 2.4 Continued.

Table 2.3 XPS peak parameters of particles produced by the hydrothermal method.

Binding Energy (eV)		FWHM (eV)	Area %	Surface species
Fe $2p_{3/2}$	707.34	0.941	57.2	FeS_2
	709.66	1.635	26.1	FeO/Fe(III)-S
	711.75	1.319	16.7	$Fe(OH)O/FeCl_3$
S $2p_{3/2}$	162.59	0.871	49.6	FeS_2
	163.75	0.777	21.7	Polysulfide (S_8)/S
	168.88	1.203	28.7	$FeSO_4$

2.3.3 Surface Characterization for Ultrasonic Synthesized Pyrite

Pyrite particles were successfully generated with different ultrasonic aging methods and had an octahedral or cubic shape (Figure 2.5). But with method U1, there were more small size particles (compare Figure 2.5 (a)-(d)) with Figure 2.1 (a). Methods U2-U3 produced more uniform and smaller particles with sizes around 300 nm to 600 nm. Many fragments of pyrite crystals were observed in Figure 2.5 (f), which is believed to have been caused by additional sonication of the particles.

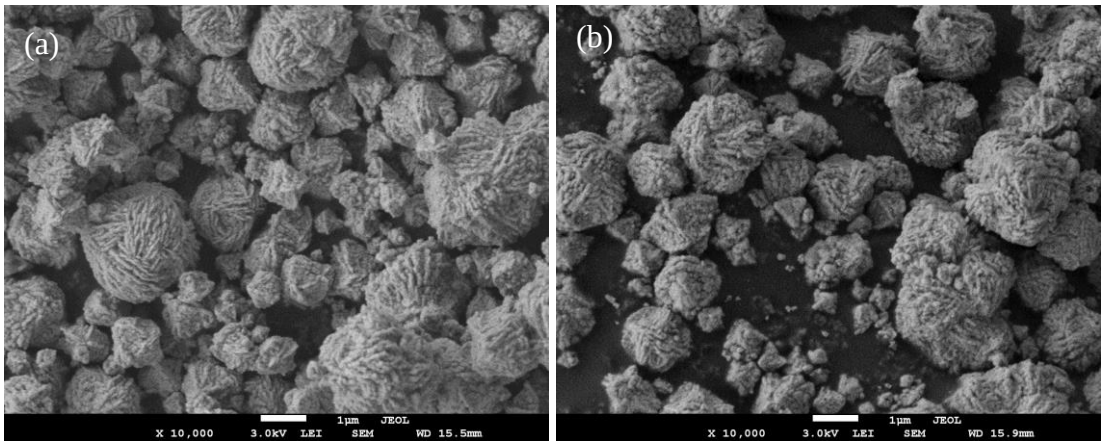

Figure 2.5 SEM images of particles produced by the ultrasonic method. (a) U1 (2 hour), (b) U1 (3 hour), (c) U1 (2 hour with an additional 19 hours of hydrothermal aging), (d) U1 (3 hour with an additional 19 hours of hydrothermal aging), (e) U2, (f) U3, (g) U4.

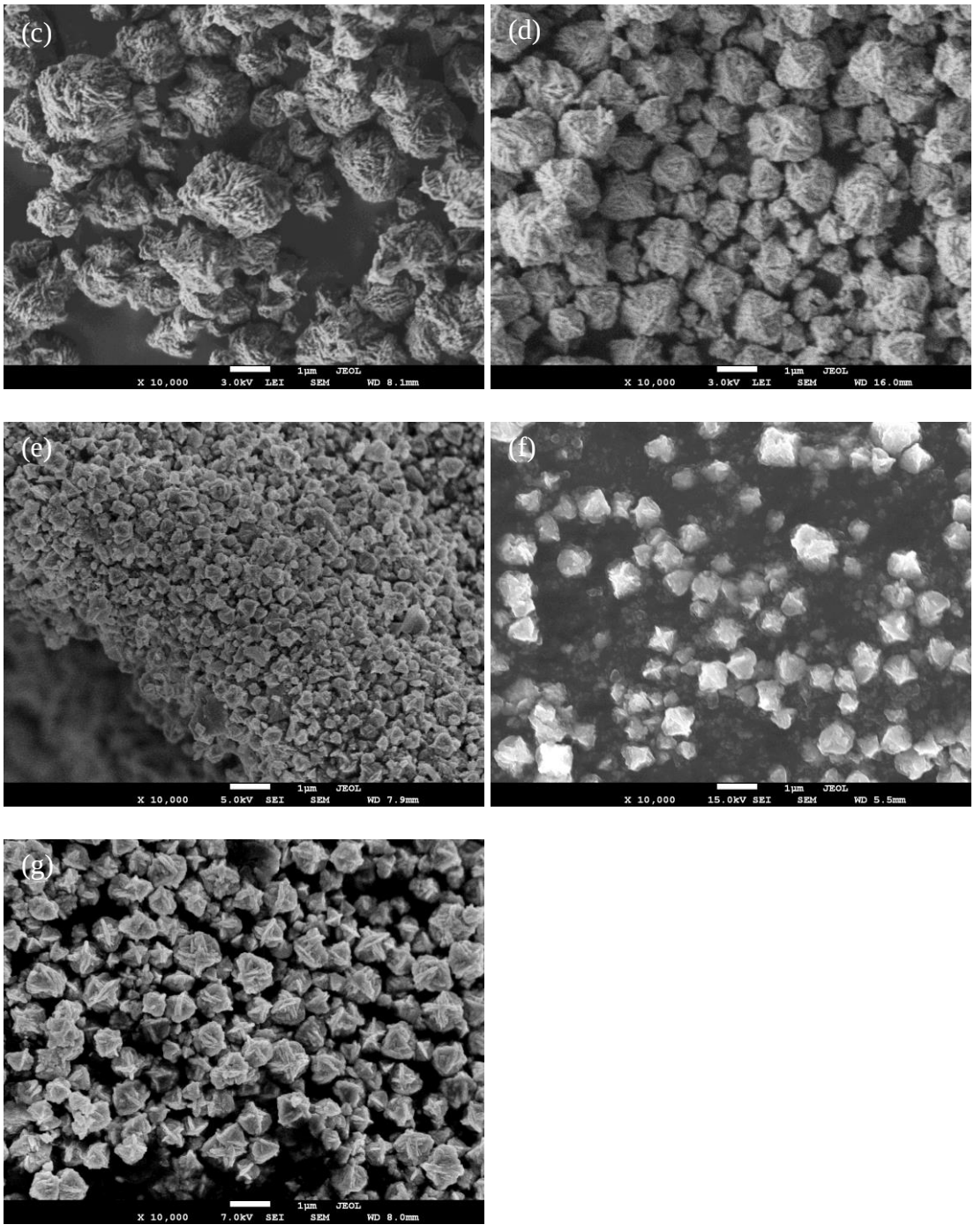

Figure 2.5 Continued.

Since method U2 generated the smallest particles, they were chosen for XRD analysis. The XRD pattern indicates that pyrite was the primary compound as shown in Figure 2.6. There were no other solid phases identified.

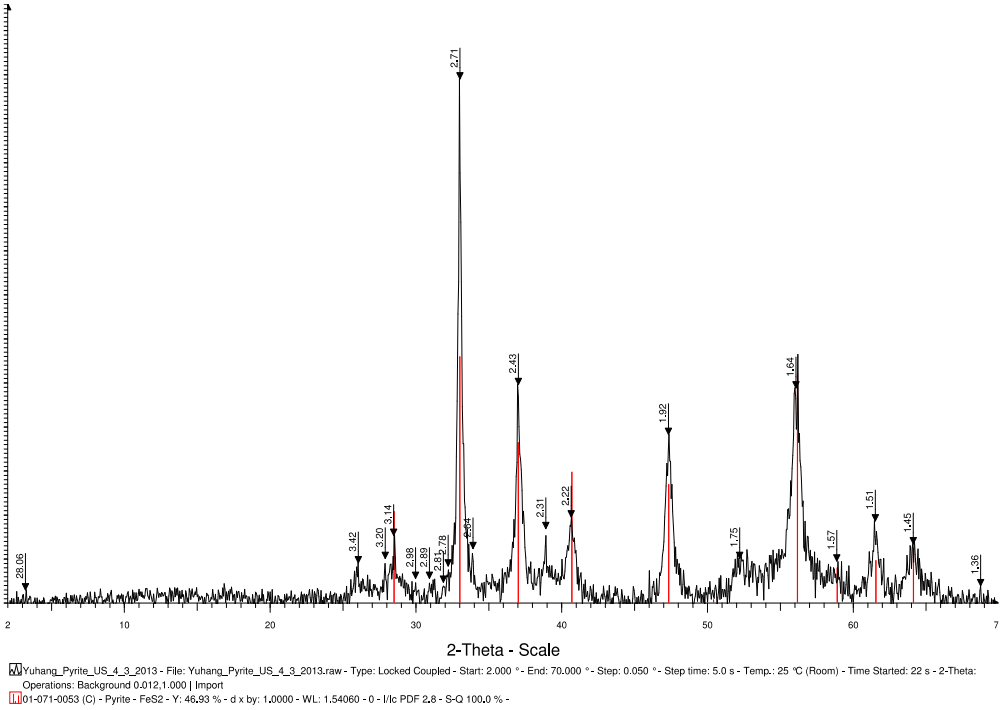

Figure 2.6 XRD patterns of U2 synthesized particles.

The particles synthesized by method U2 were also investigated by XPS. Figure 2.7 shows the broad scan of the sample, which indicates that the surface of the particles contains iron, sulfur, oxygen, and carbon. Carbon was mainly from the carbon tape, which was used to hold particles on the sample holder. Sulfur to iron atomic

concentration ratio was found to be 7, which is very high, indicating the possibility of elemental sulfur in the sample.

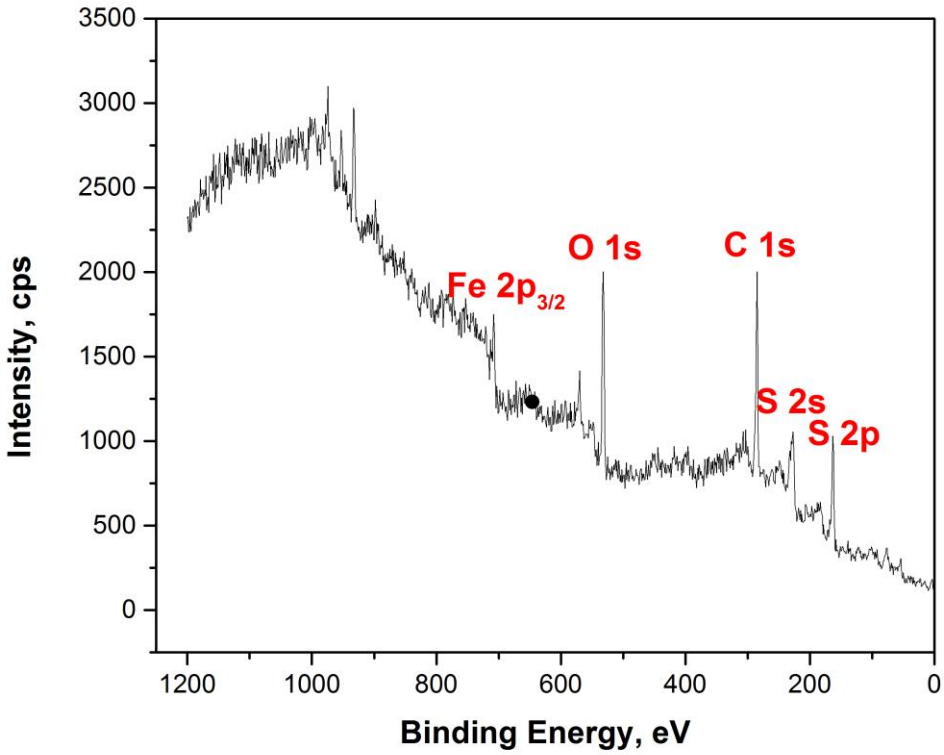

Figure 2.7 XPS Broad scan of particles produced by method U2.

Figure 2.8 shows the Fe 2p and S 2p spectra from the narrow scan of the particles and the parameters for the peaks are shown in Table 2.4. The binding energy at 707.2 eV and 162.3 eV are the two major peaks of Fe $2p_{3/2}$ and S $2p_{3/2}$ spectra and they were

identified to be the characteristic peaks of pyrite.[57, 71-73] The minor peak in the Fe 2p spectra at 708.2 eV also represents Fe(II)-S. The other minor peak at 711.8 eV represents Fe(III)-OH.[71, 74] The other peak at 163.2 eV in S 2p spectra indicates polysulfide.[57, 71, 73] The surface of pyrite might be slightly oxidized, but without highly oxidized sulfur since peaks associated with sulfate were not found.

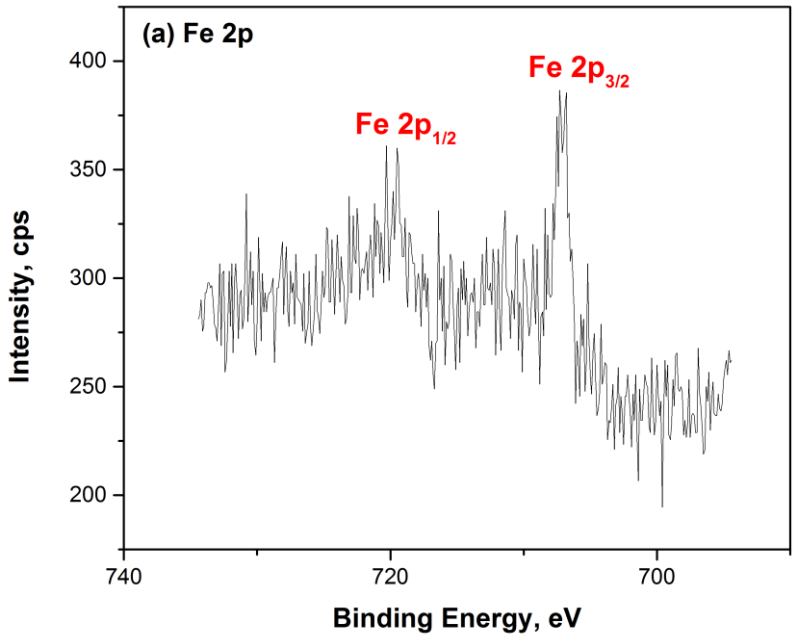

Figure 2.8 XPS spectra of particles produced by method U2 (a) Fe 2p. (b) S 2p.

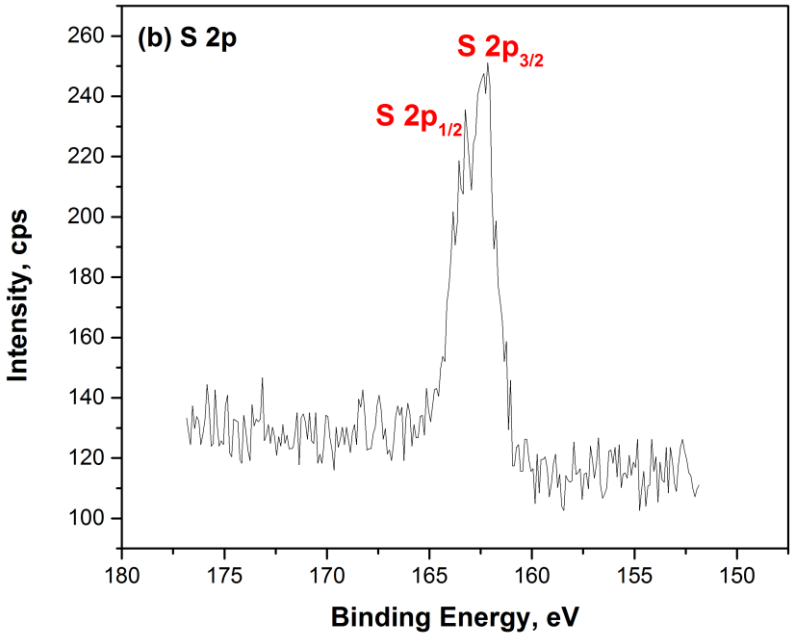

Figure 2.8 Continued.

Table 2.4 XPS peak parameters of particles produced by method U2.

Binding Energy (eV)		FWHM (eV)	Area %	Surface species
Fe $2p_{3/2}$	707.2	1.03	37.6	Fe(II)-S
	708.2	1.2	8.6	Fe(II)-S
	711.8	3.55	25.3	Fe(III)-OH
S $2p_{3/2}$	162.3	1.08	55.0	FeS_2
	163.2	1.3	45.0	Polysulfide

2.3.4 Surface Characterization of Microwave Synthesized Pyrite

SEM micrographs and EDS spectra of particles synthesized by various microwave methods are shown in Figure 2.9 and Figure 2.10. Figure 2.9 (a) was taken at magnification of 5,000×, while the others were taken at magnification of 10,000×. The particles in Figure 2.9 (a) were amorphous and particle size was obviously larger than others (Figure 2.9 (b)-(f)). The S/Fe ratio was measured to be 6.35 (Figure 2.10 (a)), which is higher than expected for pyrite. The other five microwave methods successfully produced small, highly crystalline pyrite particles with uniform morphology.

When comparing Figure 2.9 (b) to (f), particles synthesized by the methods of 40% power for 2 min, 60% power for 1 min, and 100% power for 1 min were smaller than those produced by the methods of 20% power and also smaller than those produced by ultrasonic method (Figure 2.5). EDS results were similar for these five combinations, as shown in Figure 2.10 (b)-(f). The S/Fe molar ratios were measured around 2, which is the expected value for pyrite.

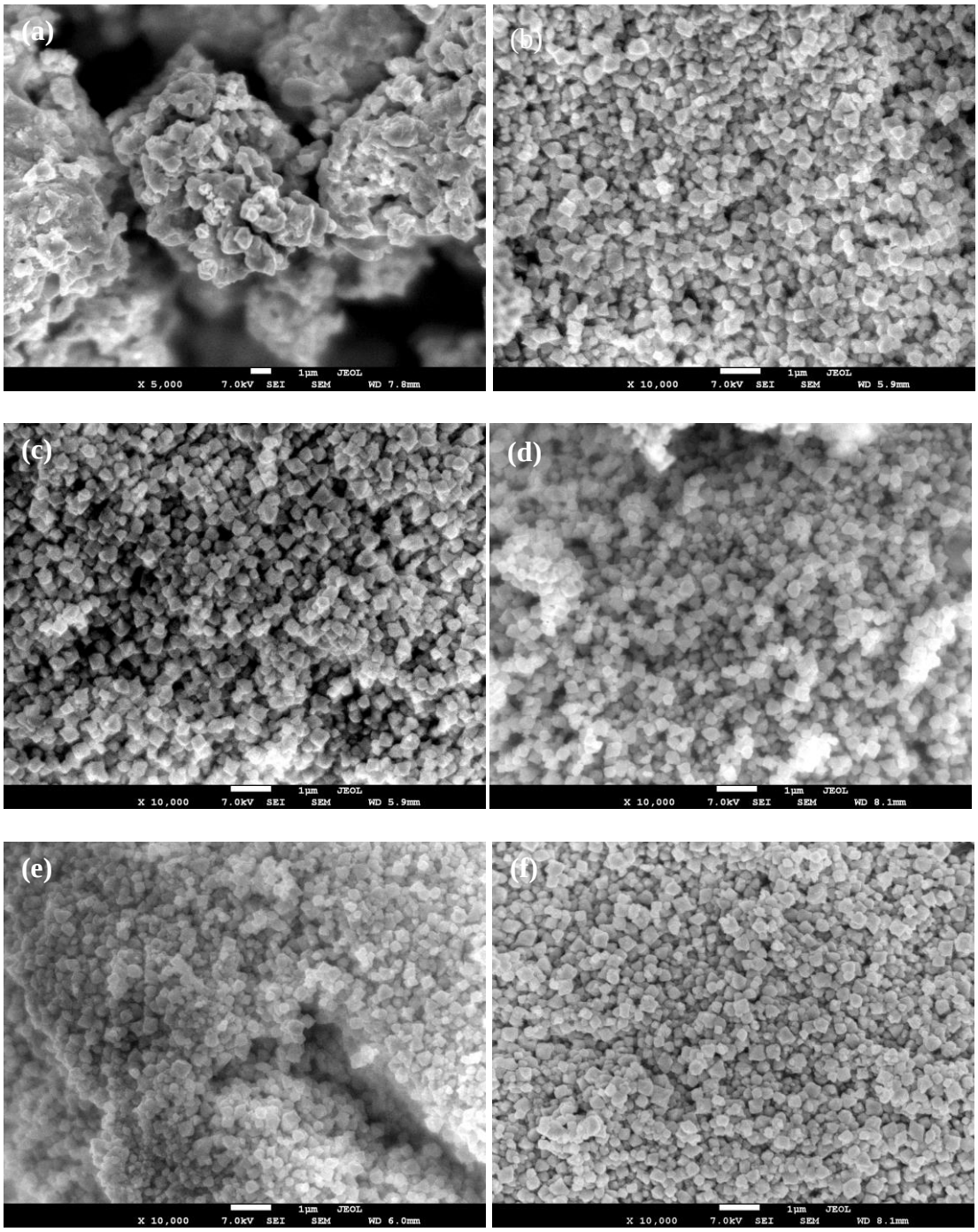

Figure 2.9 SEM images of the particles produced by microwave irradiation at (a) 20% power for 2 min, (b) 20% power for 4 min, (c) 20% power for 6 min, (d) 40% power for 2 min, (e) 60% power for 1 min, and (f) 100% power for 1 min.

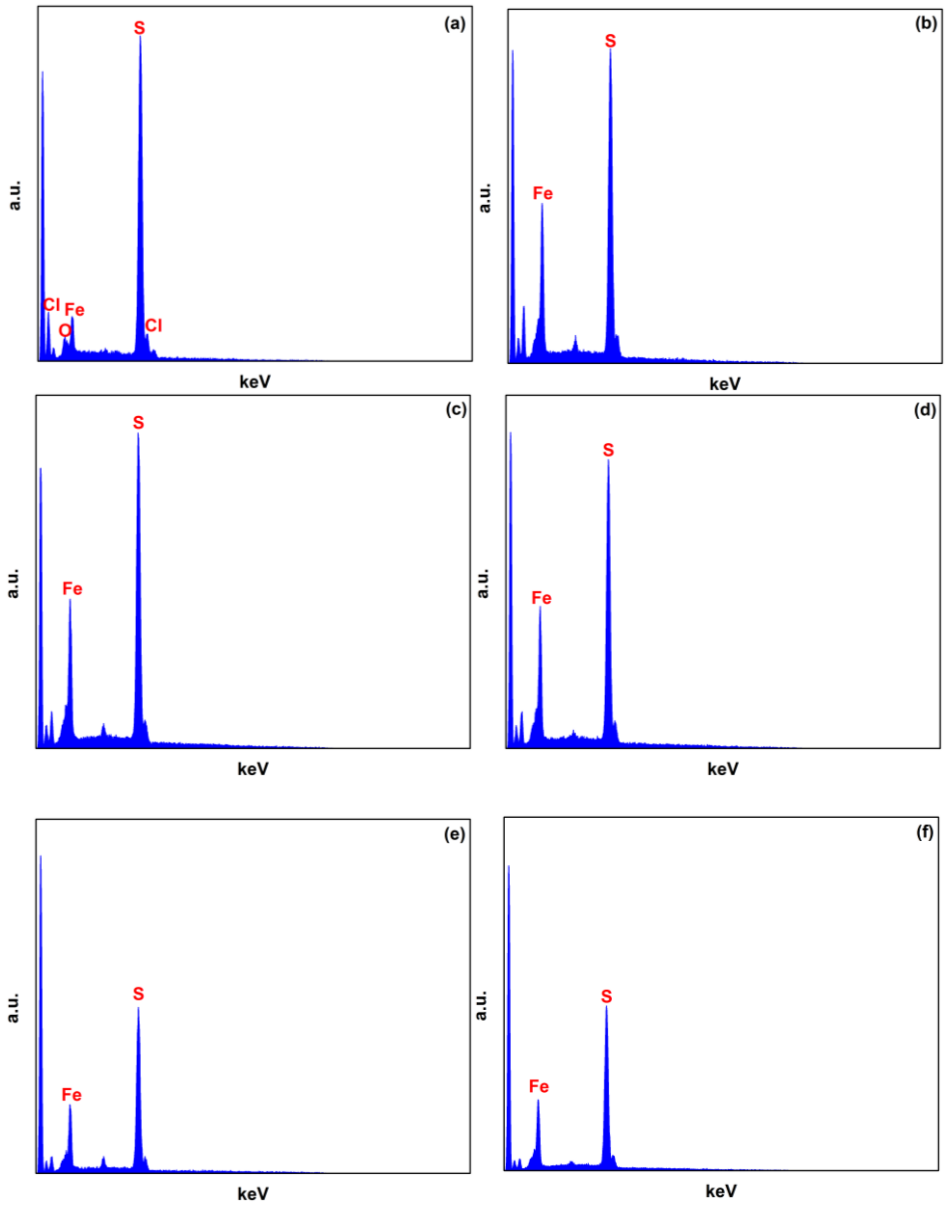

Figure 2.10 EDS spectra of synthetic pyrite produced by microwave irradiation at (a) 20% power for 2 min, (b) 20% power for 4 min, (c) 20% power for 6 min, (d) 40% power for 2 min, (e) 60% power for 1 min, and (f) 100% power for 1 min.

The microwave method that uses 100% power for 1 min was selected to generate pyrite particles for additional testing with TEM/EDS. Figure 2.11 (a)-(b) shows the TEM micrograph of the particles at different magnifications. Beautiful lattice fringes and moiré patterns were observed under TEM. Electron diffraction in TEM (Figure 2.11 (c)) showed a spotty pattern and indicated that the synthesized particles were highly crystalized pyrite. The size of the particles was estimated to be between 100 nm and 200 nm, which was smaller than those produced by Kim and Batchelor.[43] The specific surface area was determined to be 20.1 m^2/g using N_2 BET at 77.4 K (Appendix A, Figure A.1). The d-spacings calculated from lattice fringes and electron diffraction (Figure 2.12) matched with the XRD pattern (Figure 2.13). The particles were further identified as pyrite based on the TEM/EDS spectra (Figure 2.11 (d)). There were several minor peaks identified in the XRD pattern (Figure 2.13) that were from marcasite and halite (NaCl). Halite was believed to be the residuals on the surface of pyrite after vacuum filtration.

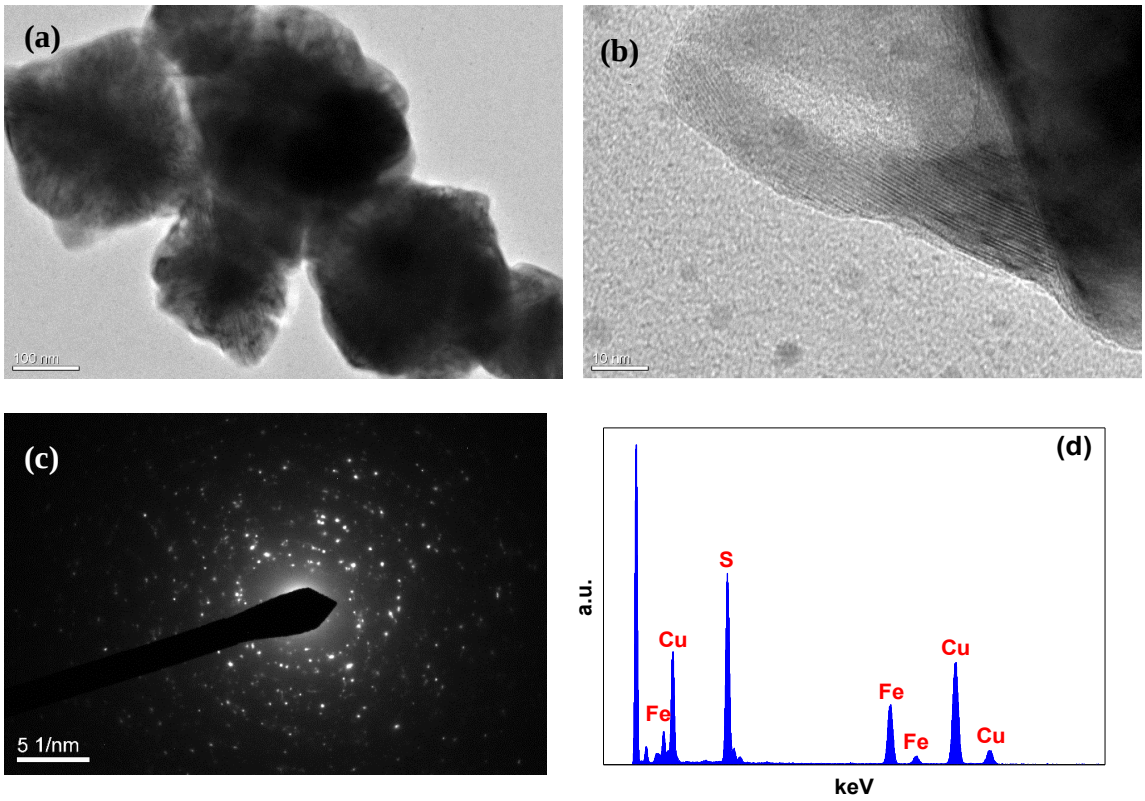

Figure 2.11 TEM images and EDS spectra of microwave-synthesized particles. (a) moiré patterns; (b) edge of the particle (lattice fringes); (c) electron diffraction; (d) EDS spectra.

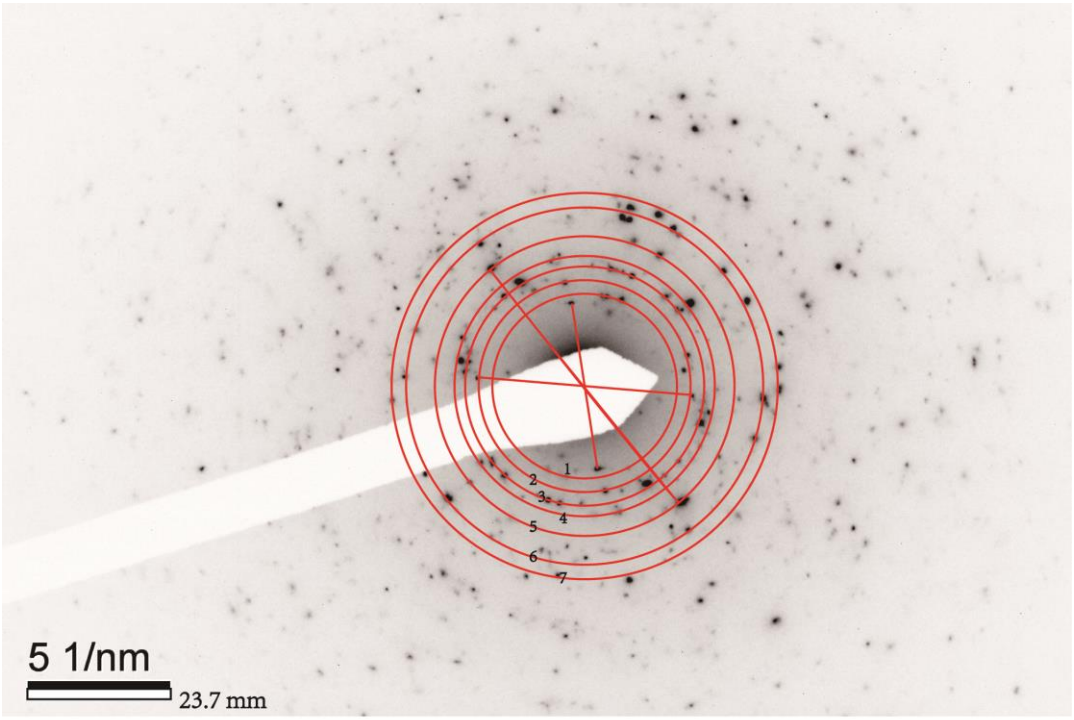

Circle	diameter (mm)	radius (mm)	d-spacing (nm)	Corresponding Mineral
1	30.5	15.25	0.311	Pyrite
2	35	17.5	0.271	Pyrite/Marcasite
3	39.5	19.75	0.240	Pyrite/Marcasite
4	43	21.5	0.220	Marcasite
5	49.5	24.75	0.192	Pyrite
6	59	29.5	0.161	Pyrite
7	63.8	31.9	0.149	Pyrite/Marcasite

Figure 2.12 Processed image with calculated d-spacings for Figure 2.11 (c) electron diffraction.

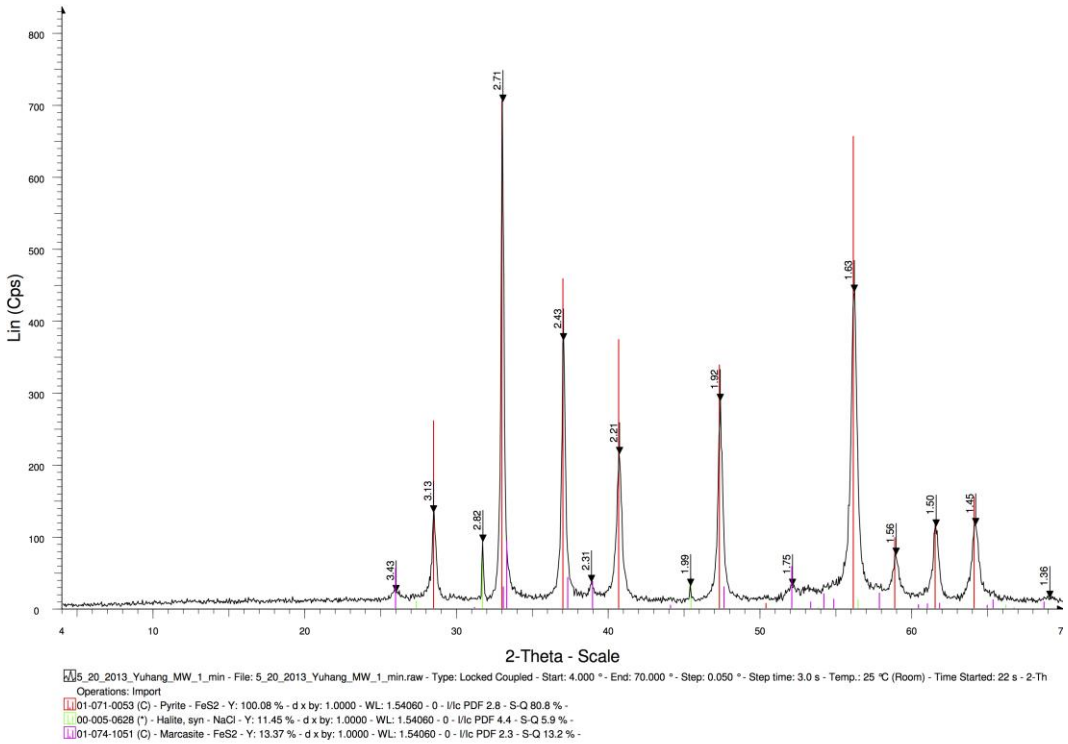

Figure 2.13 XRD patterns of microwave synthesized particles.

A broad scan of the surface of microwaved synthetic pyrite (Figure 2.14 (a)) indicated that the surface consisted of iron, oxygen, sulfur, and carbon. Carbon was mainly from the carbon tape, which was used to hold particles on the sample holder. Figure 2.14 (b) and (c) show the Fe 2p and S 2p spectra of pyrite and the parameters for the peaks are shown in Table 2.5. The two major peaks of the Fe $2p_{3/2}$ and S $2p_{3/2}$ spectra are located at binding energies of 707.46 eV and 162.6 eV and were identified to be the characteristic peaks of pyrite.[57, 71-73] The other two peaks in the Fe 2p spectra were found at 711.11 eV and 720.35 eV and they represent Fe(III)-O or Fe(II)-Cl and Fe,

respectively.[71, 74] The peak at 163.7 eV in the S 2p spectra indicates the presence of polysulfide or element sulfur.[57, 71, 73] The two narrow scan spectra indicate that the surface of pyrite might be slightly oxidized, but without the presence of highly oxidized sulfur.

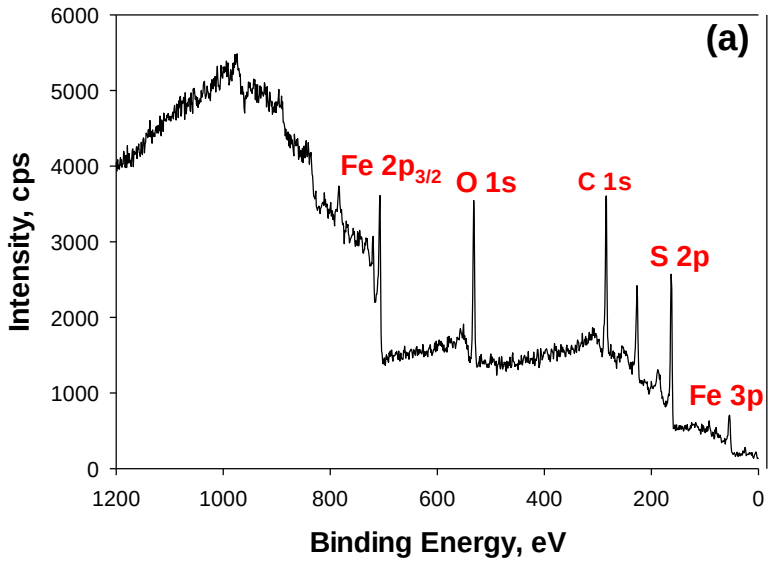

Figure 2.14 XPS spectra for microwave-synthesized particles and surface species analysis. (a) broad scan; (b) narrow scan of Fe 2p spectra; (c) narrow scan of S 2p spectra.

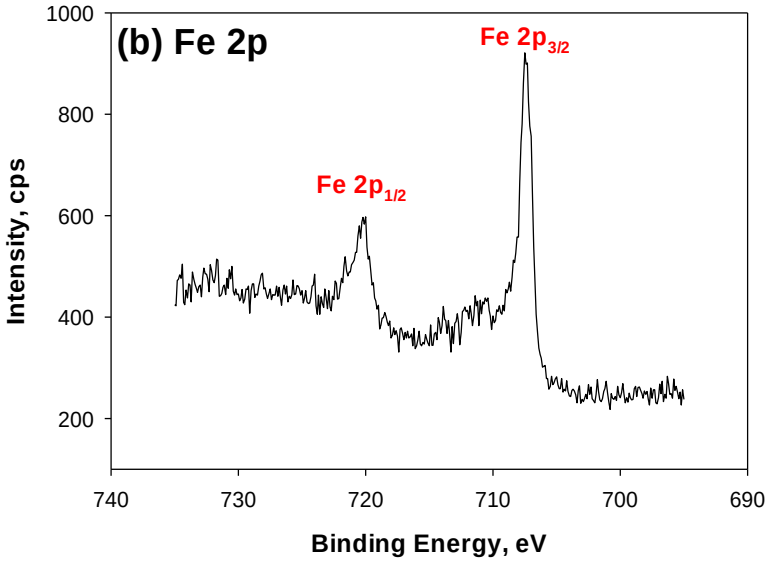

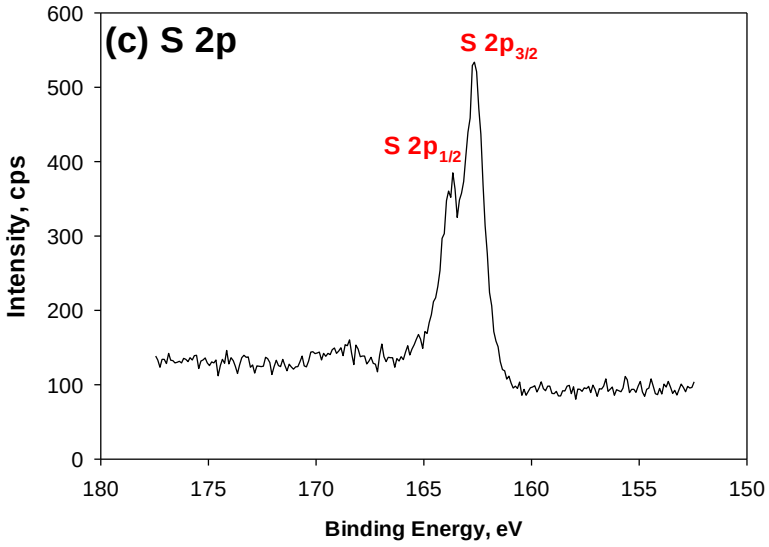

Figure 2.14 Continued.

Table 2.5 XPS peak parameters of particles produced by microwave irradiation.

Binding Energy (eV)		FWHM (eV)	Area %	Surface species
Fe 2p	707.46	1.24	50.2	FeS_2
	711.11	3.18	17.3	$Fe_2O_3/FeCl_2$
	720.35	2.20	32.4	--
S 2p	162.6	0.82	66.7	FeS_2
	163.7	0.82	33.3	Polysulfide/S

2.3.5 Mechanism

Results of SEM/EDS and XPS analyses indicated that polysulfides or elemental sulfur existed and that pyrite formed by the reaction between iron monosulfide and polysulfides. Reaction 2.9 described the initial redox reaction in the Fe^{3+}/HS^- solution.[55] Once $FeCl_3$ and NaSH solutions were mixed, amorphous black particles formed instantaneously. Those black particles dissolved in concentrated HCl, which indicated that they were FeS. The formation reaction for FeS is Reaction 2.10.[43, 55]

$$2Fe^{3+} + HS^- \rightarrow 2Fe^{2+} + S^0 + H^+ \quad (2.9)$$

$$Fe^{2+} + HS^- \rightarrow FeS + H^+ \quad (2.10)$$

Both iron monosulfide and elemental sulfur were formed, which were essential for pyrite formation. Polysulfide ions would be formed by reaction of sulfide with elemental sulfur, as shown in Reaction 2.5. Pyrite crystals were most likely formed via a FeS precursor due to the inability of pyrite to nucleate at low temperature.[64] Thus, pyrite would be formed via Reactions 2.4, 2.6, and 2.7.[43, 66, 68]

2.4 Conclusion

In this study, hydrothermal and a variety of ultrasonic and microwave aging methods were investigated to develop a fast and reliable method for synthesizing near nano-scale pyrite crystals. Pyrite was successfully synthesized within one day or even few minutes with these aging methods. Hydrothermal and ultrasonic methods generated more pyrite particles, but with longer aging times and larger particle sizes than microwave irradiation. Microwave irradiation successfully synthesized pyrite particles between 100-200 nm in only one minute with full irradiation power. The SEM/EDS and XPS analyses provide evidence of the presence of elemental sulfur even after washing with acetone and carbon disulfide, which reveals that polysulfides were possibly present. Pyrite formation is most likely via transformation of FeS precursors.

CHAPTER III

APPLICATION OF PYRITE FOR MERCURY(II) REMOVAL IN BATCH SYSTEM*

3.1 Introduction

Mercury has aroused great concerns because of the high risks it poses for both the environment and human health. Inorganic mercury could be transformed to methylmercury (MeHg) by microorganisms in aquatic ecosystems. Methylmercury is highly toxic and can be bioaccumulated in fish and wildlife via their food chains.[1, 9] Exposure to high levels of mercury will damage the cell and the central nervous system and will inhibit enzyme activities.[1, 10-12] The USEPA has classified that mercury chloride and methylmercury are possible human carcinogen.[14, 15]

In previous studies, the uptake of mercury(II) by activated carbon, oxides, and hydroxides have been widely investigated. A commercial granular activate carbon was found to have aqueous mercury(II) removal capacity as high as 61.7 μmol/g.[75] Mercury(II) uptake on fine-grained powders of goethite (α-FeOOH) was found to be 35-38 μmol/g over pH range of 4.3-7.4.[76] While γ-alumina (γ-Al_2O_3) and bayerite (β-$Al(OH)_3$) have mercury sorption capacities of 3.9-12.6 μmol/g at pH 5.2-7.8 and 3.5-4.0 μmol/g at pH 5.1-7.9, respectively.[76] However, their removal capabilities for mercury are much lower than iron sulfides. Watson et al. (1995) reported that a bacterially produced FeS has removal capacity of 665 μmol/g for Hg^{2+}.[77] Because mercuric ions are soft

*Part of this chapter is reprinted with permission from Synthesis, characterization, and application of pyrite for removal of mercury by Duan, Y.; Han, D.S.; Batchelor, B.; Abdel-Wahab, A., *Colloids and Surfaces A: Physicochemical and Engineering Aspects* **2016**, *490*, 326-335, Copyright [2016] by Elsevier B.V.

Lewis acids, they have strong affinity for soft Lewis bases, such as reduced-sulfur ligands.[23, 37, 40] Insoluble mercury sulfides and surface complexes of mercury on iron sulfides are expected to form and these solids could be removed by filtration. Sulfidation of FeS precursors would finally form more sulfur-rich phases: amorphous FeS ($Fe_{1.11}S$-$Fe_{1.09}S$), mackinawite ($FeS_{0.93}$-$FeS_{0.96}$), greigite (Fe_3S_4), and then pyrite (FeS_2).[59] Pyrite is the stable phase of iron sulfides and is also the most abundant metal sulfide on the surface of the earth. The adsorption of Hg(II) onto pyrite is largely affected by pH. The adsorption rate and capacity increase as pH increases.[37, 78] At acidic pH, the pyritic site (≡S-H) is the dominant function group on the surface of pyrite and reacts with mercury to form surface complexes, such as ≡S-Hg-Cl and ≡S-Hg-OH.[37, 40, 44] Several studies suggested that the Hg-Cl complex exists as an ordered monolayer on the surface of pyrite.[37, 78] Hyland et al. (1990) stated that both surface precipitation and adsorption of mercury occur on the surface of pyrite at low pH.[34] Formation of HgS by reaction of FeS_2 is shown in Reaction 3.1.[34] However, Behra et al. (2001) and Ehrhardt et al. (2000) pointed out that HgS does not form, based on the absence of S(II) in the S 2p spectra.[40, 44] At alkaline pH, the surface of pyrite is oxidized and covered by a layer of Fe (III) oxyhydroxide.[40, 44] The oxyhydroxide site (≡O-H) is the major functional group on the pyrite surface at basic pH and produces more complex aqueous chemistry.[37, 40, 44] At basic pH, mercury could go into the interface of pyrite-oxyhydroxide and form surface complexes between mercury and both pyritic and oxyhydroxide sites.[37, 44]

$$FeS_2 + HgCl_2(aq) \rightarrow HgS(s) + FeCl_2(aq) + S(0) \quad (3.1)$$

Although pyrite has been demonstrated to be an excellent absorbent in removing mercury from water while forming stable residuals, the pyrites used in those studies were all of macro-scale size or even larger.[34, 37, 39, 40, 44, 46, 48] In this research, we applied synthetic pyrite particles near the nano-scale in batch system to investigate the kinetics and capacities of removal of mercury(II) as affected by compounds (nitrate, sulfate, humic acids) that are major components found in wastewater. Surface reaction mechanisms were also discussed to provide better understanding of mercury(II) sorption on pyrite.

3.2 Materials and Methods

3.2.1 Anaerobic Condition

All experiments and related work were conducted in an anaerobic chamber (Coy Laboratory Products Inc.) that was filled with ultra-high purity (UHP) nitrogen. The anaerobic chamber was vacuumed and refilled with nitrogen gas once the door was opened in order to keep the anaerobic conditions inside the chamber. The deionized water (Milli-Q, Millipore) used in all experiment was deoxygenated by sparging with UHP nitrogen for 2 hours outside the chamber and then for 24 hours inside the chamber.

3.2.2 Hg(II) Removal Batch Tests

As described in Chapter II, pyrite particles were prepared by mixing 15 mL of 0.1 mol/L iron(III) chloride hexahydrate (97%, Sigma-Aldrich) and 15 mL of 0.2 mol/L sodium hydrosulfide hydrate (Sigma-Aldrich) and adding sufficient 1 mol/L NaOH to

achieve pH 4.5. The mixture was then irradiated by a commercial microwave (Emerson MW8779W, output 800 W, 2450 MHz) for 1 min at 100% power level in a microwave digestion bomb (45 mL, Parr Instrument Company). Excess FeS was removed by adding 10 mL concentrated HCl (J.T. Baker).[62] Then, the solid phase was collected by vacuum filtration with a 0.02-μm anodisc type 13 membrane filter (47 mm-diameter, Whatman) and washed several times with acetone and carbon disulfide to removal residual sulfur from the solid surface.[43] The synthesized solids were then dried inside the anaerobic chamber.

Batch experiments were conducted with synthesized pyrite in order to investigate effects of time and pyrite dose on mercury removal. In the kinetic tests, the effects of pyrite dose (0.1 g/L and 0.01 g/L) and background salts (0.01 mol/L $NaNO_3$ and Na_2SO_4) were evaluated. The mercury stock solution (1 mmol/L $HgCl_2$) and pyrite stock solution (0.2 g/L and 0.02 g/L) were separately adjusted to pH 8 by adding NaOH (0.1 mol/L) and HCl (0.1 mol/L). The DI water was adjusted to pH 8 and was used to dilute the stock solutions to desired concentrations. The Hg(II) concentrations were measured at 10 sampling times over 24 hours. In batch removal tests that evaluated the effects of mercury loading (Hg(II)/pyrite), 10 initial mercury concentrations ranging from 5 μmol/L to 500 μmol/L were used with 0.1 g/L pyrite and samples were taken at 1, 3, and 7 days. The effects of background salts (0.01 mol/L $NaNO_3$ and Na_2SO_4) and humic acids (5, 10, 20 mg/L) were evaluated as was done for kinetic tests. Values of pH were recorded at each sampling time.

3.2.3 Analytical Methods

Cold-vapor atomic absorption spectroscopy (CVAAS) was used to analyze mercury in this research and consisted of an atomic absorption spectrometer (AAS, Thermo Scientific, Solaar M6) equipped with a continuous flow vapor generation system (Thermo Scientific, VP 100). A solution of tin(II) chloride (98%, Sigma-Aldrich) in 10% HCl (J.T. Baker) was used to reduce Hg(II) to metallic mercury for analysis. The following parameters were used for the analysis: wavelength of 253.7 nm, band pass of 0.5 nm, lamp current of 75%, background correction of D2 quadline, measurement number of 3, measurement time of 4 s, measurement delay of 90 s, pump speed of 50 RPM (which provides a sample flow rate of 11.5 mL/min, a reductant flow rate of 2.4 mL/min, and an acid reagent flow rate of 1.3 mL/min), and carrier gas (Argon) flow of 100 mL/min. The average recovery (accuracy) was 99.71 % and the standard deviation (precision) was 0.18 μg/L. The average method detection limit (MDL) for mercury(II) was 0.58 μg/L. Before analysis, the samples were diluted with 10% HCl to achieve mercury concentrations in the range 0-100 μg/L. Samples taken from pyrite suspensions were passed through a 0.02-μm anodisc type 13 membrane filter (25 mm-diameter, Whatman). The filtrate was analyzed by CVAAS.

3.2.4 Microscopic and Spectroscopic Characterization

The surface of synthesized pyrite after contact with mercury was characterized by SEM/EDS and XPS. A scanning electron microscope (SEM) equipped with an energy dispersive x-ray spectroscopy (EDS) system (JSM-7500F, Tokyo, Japan) was utilized to

study the morphology and chemical composition of synthesized pyrite. The image was collected at a working distance of 15 mm or 8 mm under acceleration voltage range of 3 kV to 7 kV at a magnification of 10,000× or 20,000×.

An Omicron NanoTechnology XPS (Germany) with Mg-Kα source was used to analyze chemical composition on the surface of pyrite after it had reacted with mercury. The survey scans were recorded with pass energy of 100 eV and the narrow scans used lower pass energy (20 eV or 50 eV) for higher resolution. The spectra peak of C 1s with a binding energy of 284.5 ± 0.1 eV was used as a reference to correct expected charging effects. The narrow scan spectra of Fe 2p, S 2p, and O 1s were fitted with XPSPEAK41 fitting program with a Gaussian Lorentzian peak function through background-subtraction corrections using a Shirley-type optimization.

3.3. Results and Discussion

3.3.1 Removal Kinetics

The kinetics of Hg(II) removal with different doses of pyrite was investigated in a batch system without a buffer. Figure 3.1 (a) shows that a dose of 0.1 g/L pyrite was able to remove about 90% of the initial concentration of Hg(II) of 5 μmol /L in the first 5 minutes. After the rapid removal, the Hg concentration in solution began to increase, but eventually decreased to near zero after 12 hours. Similar behavior was observed with a lower dose of pyrite (0.01 g/L) as shown in Figure 3.2 (a) where a rapid decrease in Hg was followed by much slower decrease in concentration. However, at the lower dose, the

experiment did not continue for long enough for the concentration of Hg to approach zero.

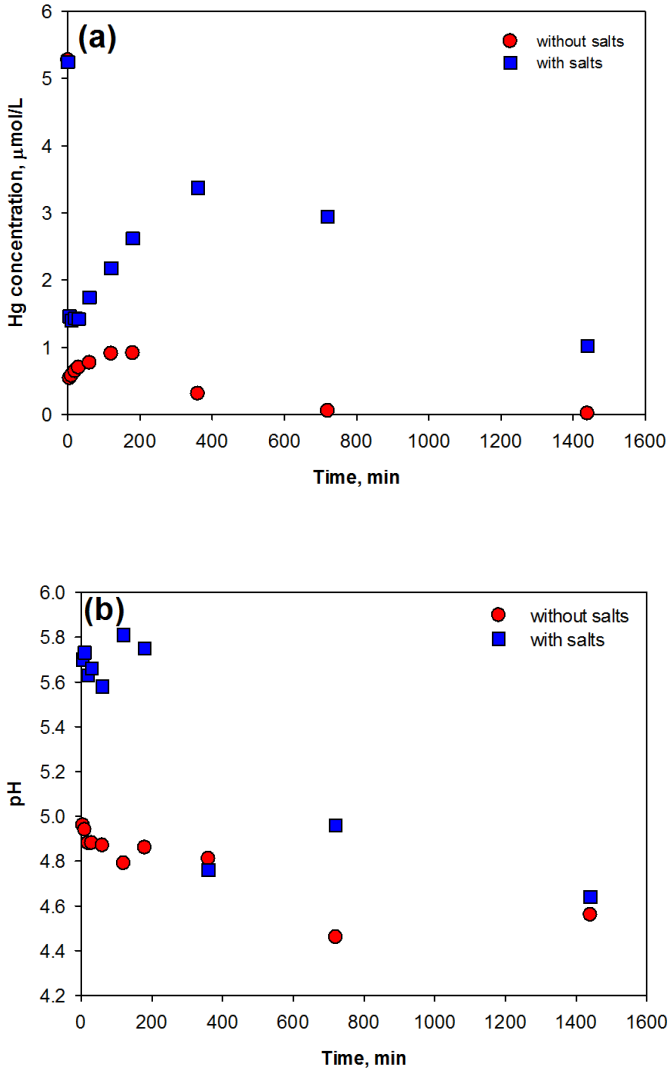

Figure 3.1 Kinetic removal test with FeS_2 dose = 0.1 g/L, initial concentration of Hg(II) = 5 µmol/L (a) concentration of mercury as a function of contact time; (b) pH as a function of contact time.

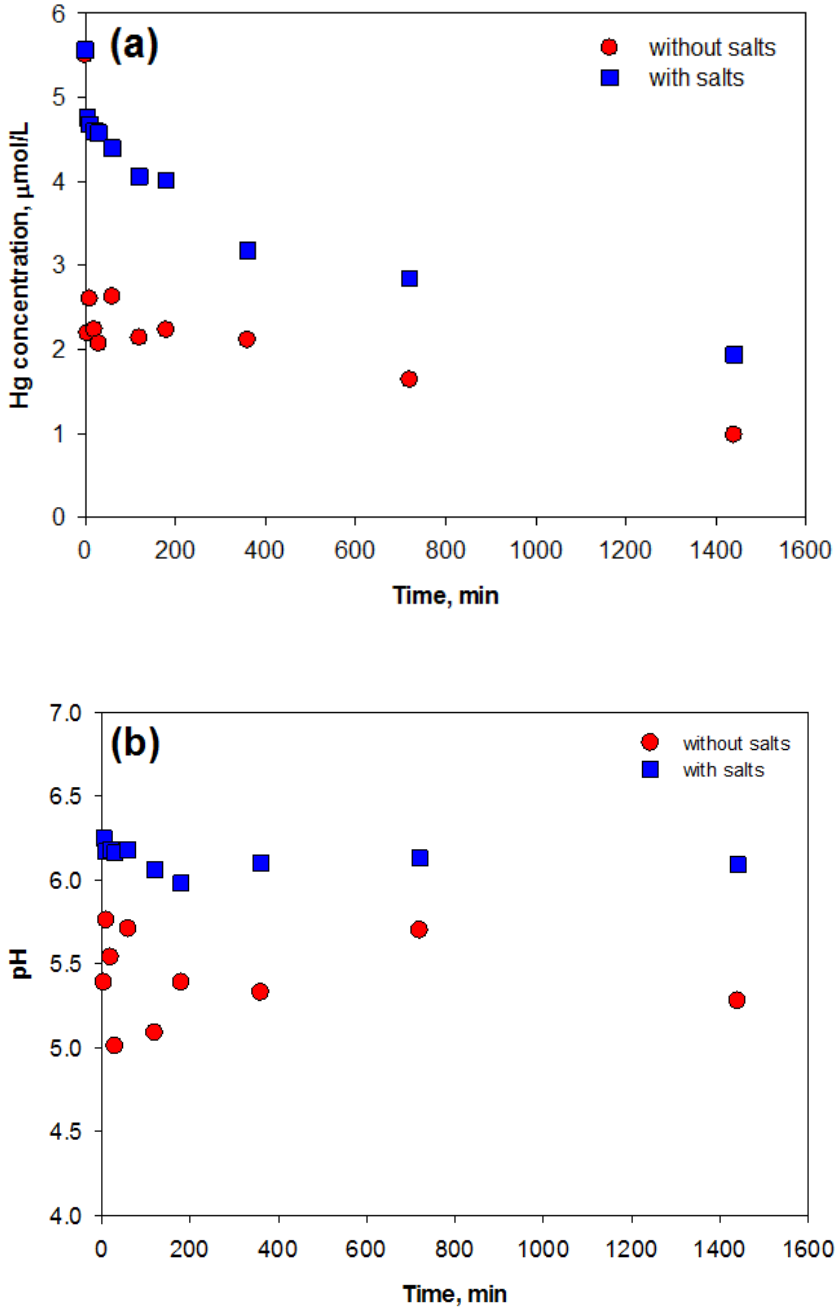

Figure 3.2 Kinetic removal test with FeS_2 dose = 0.01 g/L, initial concentration of Hg(II) = 5 µmol/L (a) concentration of mercury as a function of contact time; (b) pH as a function of contact time.

The removal/release pattern observed for Hg could be described by a two-step mechanism in which Hg(II) is removed by adsorption (Reaction. 3.2) followed by reaction with sulfides and elemental sulfur to form soluble Hg-polysulfide-sulfide complexes (Reaction 3.3), which would increase the concentration of total mercury in solution. Such complexes have been reported in the literature.[45-47] The presence of elemental sulfur on the surface, which is necessary to form polysulfides, was confirmed by SEM/EDS and XPS analyses. The resorption of Hg could be caused by changes in the surface sites that occur over time or changes in the types of complexes that result in forming complexes that are more likely to be adsorbed by pyrite.

$$FeS_{2(s)} + Hg(OH)_2 \rightarrow FeS_2\text{-}Hg(OH)_{2(adsorbed)} \quad (3.2)$$

$$FeS_2\text{-}Hg(OH)_{2(adsorbed)} + 2\ HS^- + (x-1)\ S(0) + H^+ \rightarrow Hg(S_x)(SH)^- + FeS_2(s) + H_2O \quad (3.3)$$

In all experiments, the pH was observed to be much lower than in the solution before addition of pyrite and that smaller changes in pH were observed when a lower dose of pyrite was used (Figure 3.2 (b) compared to Figure 3.1 (b)). Pyrite surface was protonated after washing with HCl, and release of hydrogen ions from the pyrite surface (Reactions 3.4 and 3.5) was gradual (Appendix A, Figure A.2). Therefore, even if the pyrite suspension were adjusted to pH 8 before mixing, the pH of the mixture would decrease over time due to the slow release of protons from the pyrite surface. Furthermore, the adsorption reaction between sulfidic pyrite surface sites and Hg(II) also contributed H^+ into the mixture. Before mixing and immediately after adding base, the pH of pyrite suspension was around 8 and both sulfidic ($\equiv$S-H and $\equiv S\text{-}H_2^+$) and iron

hydroxide (≡Fe-O-H and ≡Fe-O-H_2^+) groups exist[40] and tend to be more protonated. Adsorption of Hg(II) onto protonated sites would release H^+, as shown in Reactions 3.6 and 3.7. Therefore, deprotonation of pyrite surface and adsorption of Hg(II) would explain the initial drop in pH.

$$\equiv S\text{-}H_2^+ \rightarrow \equiv S\text{-}H + H^+ \quad (3.4)$$

$$\equiv Fe\text{-}OH_2^+ \rightarrow \equiv Fe\text{-}OH + H^+ \quad (3.5)$$

$$\equiv S\text{-}H_2^+ + Hg(OH)_2 \rightarrow \equiv S\text{-}HgOH + H_2O + H^+ \quad (3.6)$$

$$\equiv Fe\text{-}OH_2^+ + Hg(OH)_2 \rightarrow \equiv Fe\text{-}O\text{-}HgOH + H_2O + H^+ \quad (3.7)$$

Several possible mechanisms for the release of mercury were considered. Those discarded include the assumption that surface reactions of Hg(II) produced Hg(I), Hg(0) or other soluble Hg species that were released to the solution. This mechanism was discarded because analysis of samples by CVAAS in which Hg in the sample was not reduced to Hg(0) by tin chloride, and the analysis of samples by XPS spectra of Hg 4f, did not find any Hg(0) present in the solution or on the surface. The presence of Hg(0) was ruled out in agreement with previous results of sorption of Hg(II) onto pyrite.[40, 44] Another possibility is that the increase of Hg in solution is due to the desorption of Hg(II) caused by pH change. However, pH changes after the initial drop were small, so they would not likely be the cause of all of the Hg release. A third possible mechanism is the formation of soluble Hg-polysulfide-sulfide complexes, as shown in Reaction 3.3, and this mechanism is believed to be the one that is most likely to cause the release of mercury.

The impact of salts (0.01 mol/L sodium sulfate and sodium nitrate) on Hg(II) removal with pyrite was studied. The results shown in Figure 3.1 (a) indicate that less Hg(II) was removed in 0.01 mol/L salt solutions. For the test with a pyrite dose of 0.1 g/L (Figure 3.1 (a)), the mercury removal was always lower in the presence of salts and there was a greater decrease in removal between 3 and 12 hours in the presence of salts. For the test with a pyrite dose of 0.01 g/L (Figure 3.2 (a)), removal efficiency increased over time for experiments with and without salts. However, less mercury was removed in the presence of salts, particularly in the first 3 hours. The background salts may have affected the types of surface complexes formed by adsorption of Hg(II). The presence of salts also might cause some Hg to desorb that was sorbed onto hydroxide sites, since ≡O-H groups are not as strong as ≡S-H groups.[40]

3.3.2 Effect of Mercury Loading: Adsorption of Hg(II) without Salts

The effect of mercury loading (initial Hg(II)/pyrite) on removal of Hg(II) was studied in a series of batch tests without buffer. Initial mercury concentrations were 5, 10, 25, 50, 100, 200, 300, 400, 450, and 500 μmol/L, and the dose of pyrite was 0.1 g/L so the mercury loading ranged from 50 to 5,000 μmol/g. The results are shown in Figure 3.3. The data for the amount of mercury removed per mass of pyrite (q) and concentration in solution (c) at each contact time were fitted with two models: a saturation function relationship ($q=a\times b\times c/(1+b\times c)$) and a power law relationship ($q = a\times c^b$), where a and b are the model parameters and c is the mercury concentration. All model parameters were obtained by conducting nonlinear regressions using the

MATLAB nlinfit, which used a Levenberg-Marquardt algorithm to choose parameters that minimized the sum of squared residuals (SSR). And the fitness of model to data was characterized by a goodness of fit parameter (GFP) as shown in Equation 3.8.

$$GFP = \frac{\sqrt{SSR/(n-2)}}{\bar{q}} \tag{3.8}$$

where n is the number of data points and $\bar{q}$ is the average amount of Hg adsorbed per amount of pyrite. Figures 3.3 (a) and (b) show the fitted curves and the data and the model parameters are listed in Table 3.1. The power law relationship was better able to correlate the data without salts and higher loadings were observed at higher mercury loading and at longer contact times. Mercury removal did not reach equilibrium, as more mercury continued to be removed throughout the time period of the experiment. The values of pH were measured after contact times of 1, 3, and 7 days and they are shown in Figure 3.3 (c). The overall trends of pH at the three contact times were similar. A large decrease in pH was observed at low mercury loading, while small increases in pH were observed at higher mercury loading. The highest capacity of pyrite for Hg(II) was found to be around 900 μmol Hg/g FeS_2. This is much higher than that reported by Bower et al. (2008), who reported maximum sorption capacities of 6.1 μmol/g at pH 4.1, 9.9 μmol/g at pH 6.4, and 17.4 μmol/g at pH 10.4.[37] It is also higher than value of 10 μmol/g reported by Behra et al. (2001), at pH > 4.[40] However, it is important to note that both of these references used natural pyrite that had been ground to 40~80 μm. Such pyrite is much larger and would contain more impurities than the synthetic pyrite used in this research.[37, 40]

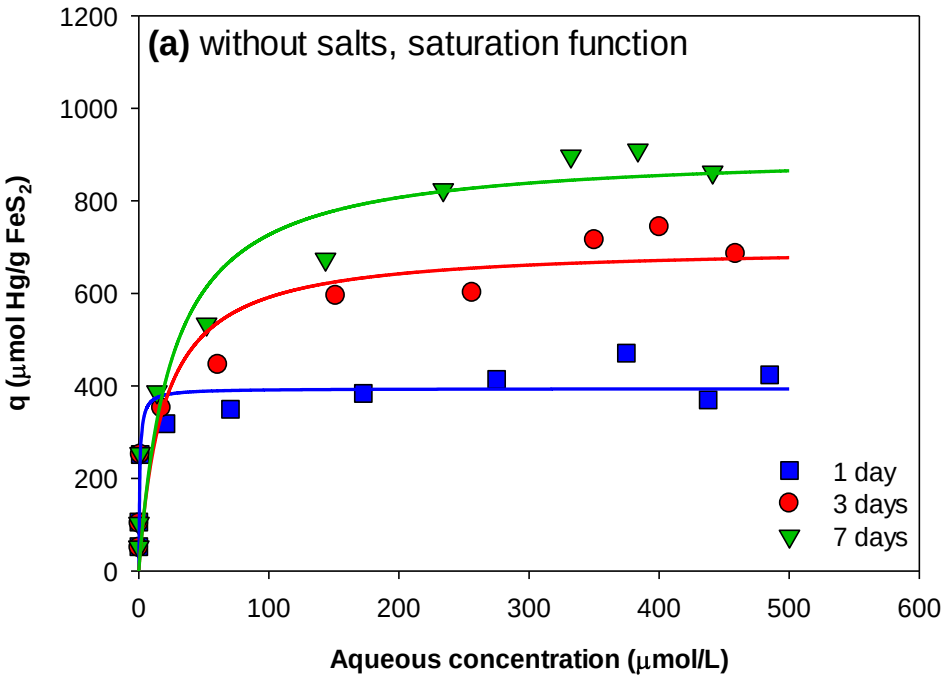

Figure 3.3 Removal of Hg(II) using synthesized FeS_2 as a function of initial Hg(II) concentration: (a) saturation function fit for uptake on pyrite; (b) power law fit for uptake on pyrite; and (c) pH at various initial Hg(II) concentrations. FeS_2 = 0.1 g/L, initial concentration of Hg(II) =5, 10, 25, 50, 100, 200, 300, 400, 450, and 500 μmol/L, initial pH = 8, contact time = 1, 3, and 7 days.

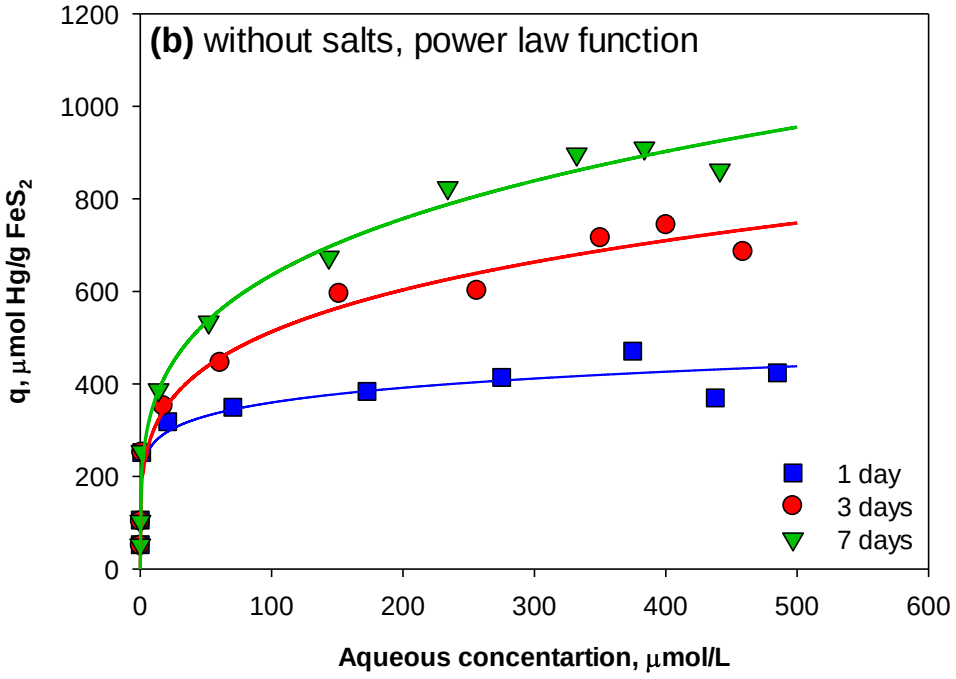

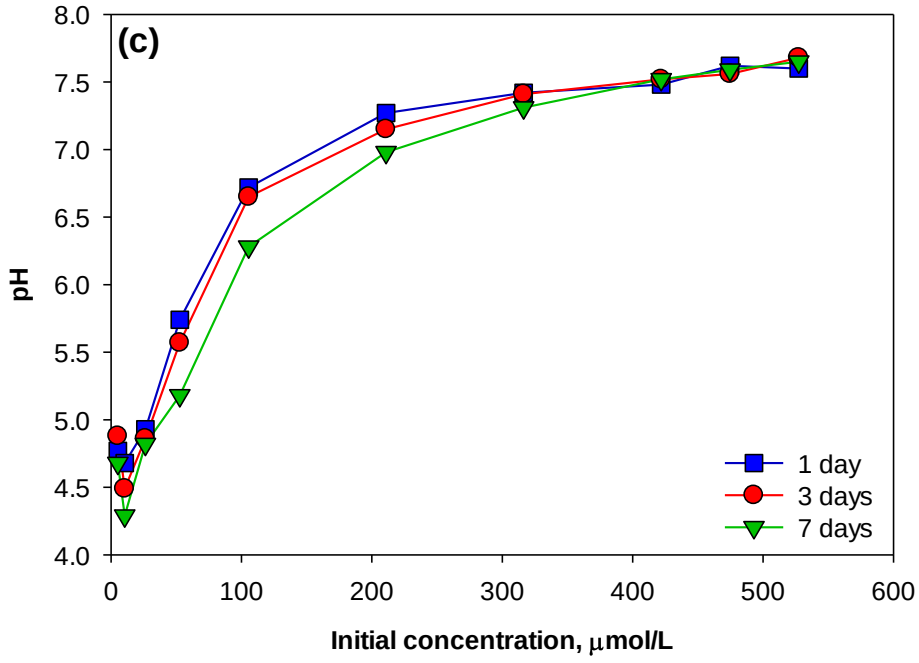

Figure 3.3 Continued.

Table 3.1 Model parameters for mercury-loading tests without salts.

Models	Contact time		
	1 day	3 days	7 days
Saturation function relationship			
b (L/μmol)	1.38 ± 0.90	0.053 ± 0.029	0.040 ± 0.018
a (μmol/g)	394± 23	703 ± 57	908 ± 69
R^2	0.82	0.86	0.90
Goodness of fit parameters	0.19	0.21	0.19
Power law relationship			
a ($\mu mol^{1-1/n}L^{1/n}/g$)	205 ± 26	174.10 ± 22.20	198 ± 20
b	0.12 ± 0.023	0.23 ± 0.023	0.25 ± 0.018
R^2	0.88	0.97	0.98
Goodness of fit parameters	0.13	0.10	0.077

The results in these experiments (Figure 3.3 (a)) after 1 day were similar to the results in the kinetic tests at 1 day, with both showing nearly 100% removal of 5 μmol/L mercury with a dose of 0.1 g/L pyrite. However, this loading was much smaller than the pyrite adsorption capacity, which means that the pyrite could remove more mercury.

In Figure 3.3 (c), larger decreases in pH were observed at lower mercury loadings. This behavior was likely due to a combination of two factors as discussed in Section 3.3.1. A drop in pH would be expected, even if no mercury were added, due to hydrogen ions released from the pyrite surface. Although base was added to the pyrite suspension to obtain pH 8, the release of protons was slow and continued after the pyrite suspension was mixed with the mercury stock solution. The other factor that affects pH changes would be the reaction of the pyrite surface with Hg(II) (Reactions 3.6 and 3.7).

However, those reactions would result in pH decreasing as more Hg(II) is removed. That is observed at low doses of Hg(II) (Figures 3.1(b), 3.2(b), 3.3(c)), but at higher doses of Hg(II), the effect was reversed and a smaller pH drop was observed. This might occur due to adsorption of Hg(II) on two different types of surface sites that have different affinities for Hg(II) and different effects on pH. Hg(II) would occupy the pyritic sites first because their affinity for Hg is stronger than that of hydroxyl groups.[40] After pyritic sites were fully occupied, Hg(II) would be sorbed by hydroxyl sites. If the acidity of pyritic sites is such that it releases protons as Hg(II) is sorbed (Reaction 3.6) and the acidity of hydroxide sites is such that protons are consumed as Hg(II) is sorbed (Reaction 3.9), then pH would be observed to initially drop and then rise as more Hg(II) is added and removed from solution. Furthermore, the protons that are released can be partially consumed by other reactions that Hg undergoes on the pyrite surface. One reaction could be formation of soluble Hg-sulfide complexes (Reaction 3.3) and another could be formation of mercury sulfide solid phases (Reaction 3.10). Therefore, as mercury loadings increase, more mercury would be adsorbed, resulting in increasing in pH.

$$\equiv Fe\text{-}O^- + H^+ + Hg(OH)_2 \rightarrow \equiv Fe\text{-}O\text{-}HgOH + H_2O \quad (3.9)$$

$$FeS_2\text{-}Hg(OH)_{2(adsorbed)} + 2H^+ \rightarrow HgS + S(0) + Fe^{2+} + 2H_2O \quad (3.10)$$

A sample from the mercury loading test with an initial Hg concentration of 500 μmol/L and contact time of 7 days was analyzed by XPS. A broad scan of the surface of the sample indicated that the surface consisted of iron, oxygen, sulfur, carbon, and mercury, as shown in Figure 3.4 (a). Carbon was from the carbon tape. The Fe 2p, S 2p,

and Hg 4f spectra of the sample are shown in Figures 3.4 (b)-(d), respectively, and the parameters for the peaks are shown in Table 3.2. The binding energy at 707.0 eV and 711.2 eV are two major peaks of Fe $2p_{3/2}$ spectra, and were identified to be the characteristic peaks of pyrite and Fe(III)-O, respectively.[71] The binding energy at 162.3 eV is the major peak of S $2p_{3/2}$ spectra, which indicates sulfides.[71] The narrow scan spectra for Hg 4f (Figure 3.4 (d)) showed nice Hg $4f_{5/2}$ and Hg $4f_{7/2}$ peaks. The Hg $4f_{7/2}$ peak with a binding energy of 100.9 eV indicates that HgS was on the surface.[34, 71] This supports the mechanism of HgS formation proposed to describe pH changes at different Hg loadings (Reaction 3.4).

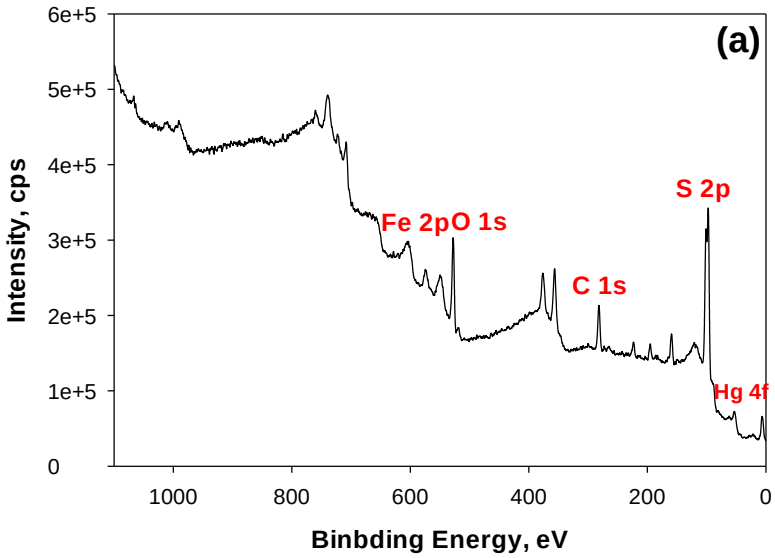

Figure 3.4 XPS spectra for sample from mercury loading test and surface species analysis (initial Hg concentration = 500 µmol/L, contact for 7 days). (a) Broad scan; (b) narrow scan of Fe 2p spectra; (c) narrow scan of S 2p spectra; (d) narrow scan of Hg 4f spectra.

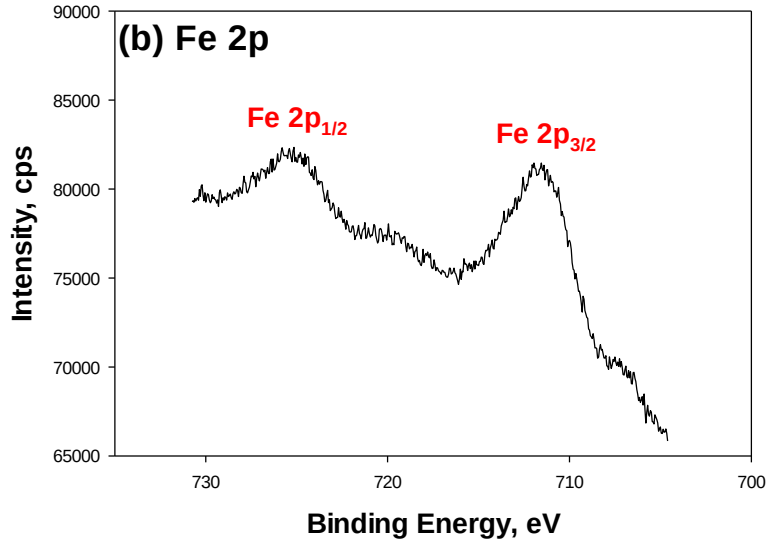

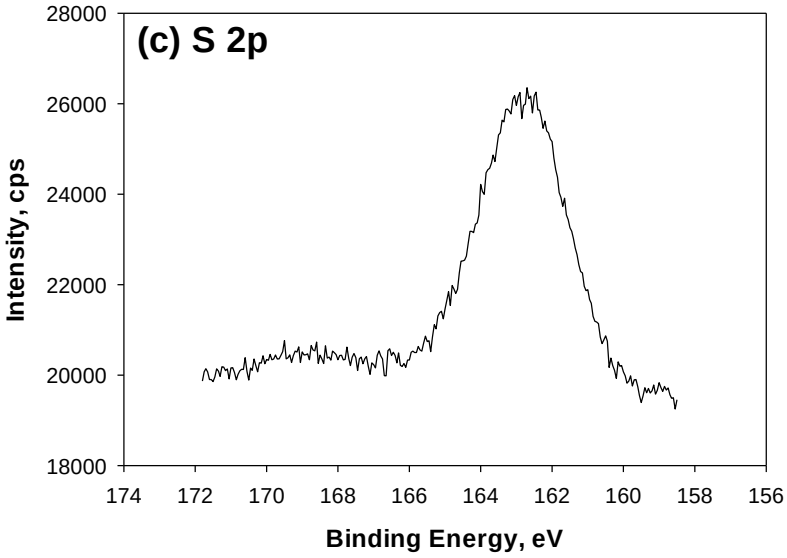

Figure 3.4 Continued.

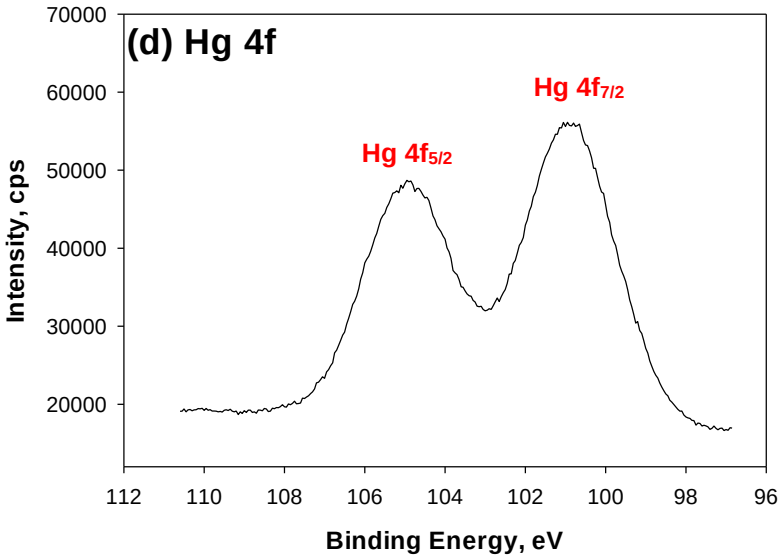

Figure 3.4 Continued.

Table 3.2 XPS peak parameters of sample from mercury loading test (initial Hg concentration = 500 μmol/L, contact for 7days).

Binding Energy (eV)		FWHM (eV)	Area (%)	Surface species
Fe $2p_{3/2}$	707.0	1.40	4.16	FeS_2
	711.2	3.68	65.00	Fe(III)
Fe $2p_{1/2}$	719.8	2.04	4.43	--
	724.8	3.64	26.42	--
S $2p_{3/2}$	162.3	1.94	55.40	Sulfide/FeS_2
S $2p_{1/2}$	163.5	1.94	44.60	--
Hg $4f_{7/2}$	100.9	2.23	58.78	HgS
Hg $4f_{7/2}$	104.9	2.09	41.22	--

3.3.3 Effect of Mercury Loading: Adsorption of Hg(II) with Salts

The effects of salts on removal of Hg(II) using pyrite (FeS_2) were studied as functions of mercury loading in a series of batch tests. Experimental conditions were the same as those described in section 3.3.2, except that Na_2SO_4 and $NaNO_3$ were added to the solution at concentrations of 0.01 mol/L. The results of these experiments are shown in Figure 3.5. The data at each contact time were fitted with the saturation function relationship and the power law relationship as shown by the lines in Figures 3.5 (a) and (b). The model parameters are listed in Table 3.3. In contrast to the result in the absence of salts, the saturation relationship was better able to correlate the data in the presence of salts. However, similar behavior was observed in that higher adsorption was observed at higher mercury loading and at longer contact times. But pyrite adsorption capacity of Hg(II) (400 μmol/g) was much lower than that in absence of salts (900 μmol/g). Similarly to the results presented in section 3.3.2, the lowest pH was found in the sample with an initial Hg(II) concentration of 10 μmol/L and the pH increased as the initial concentration increased (Figure 3.5 (c)).

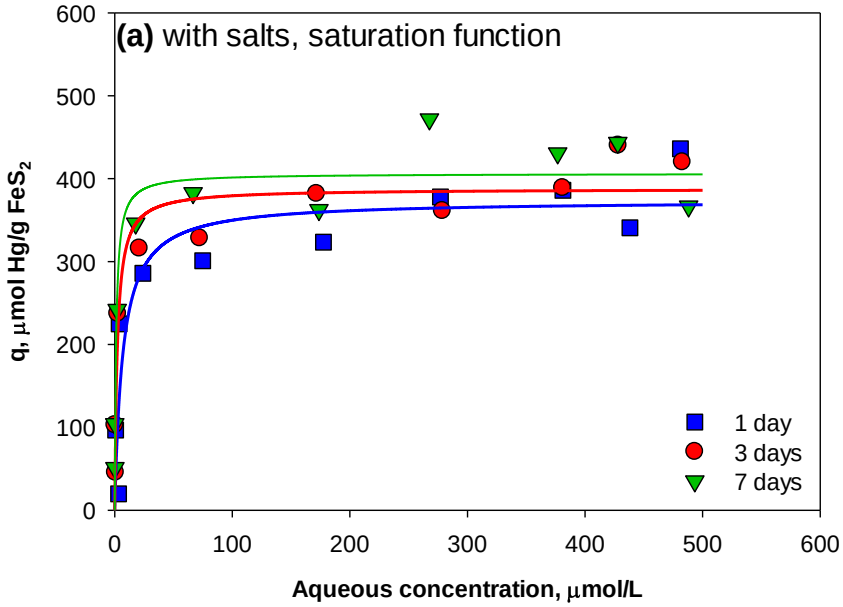

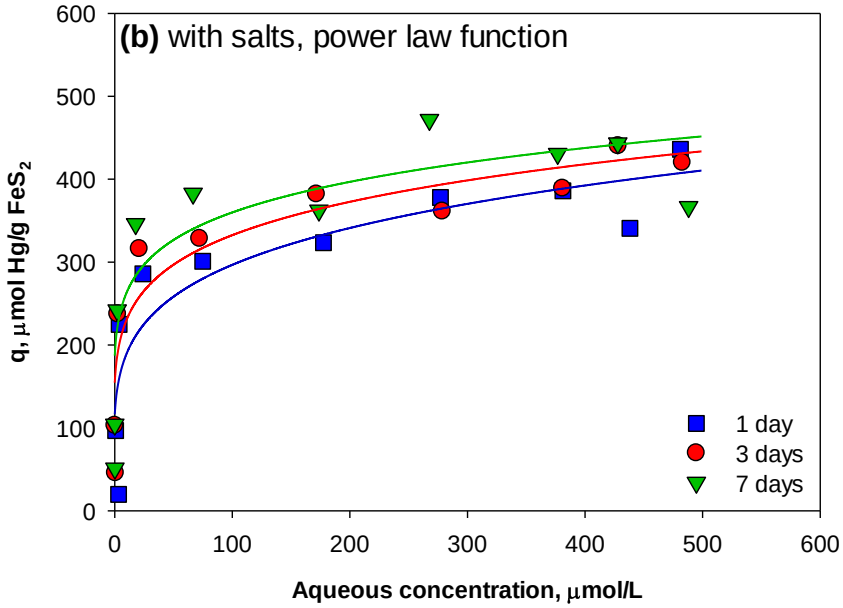

Figure 3.5 Effects of salts on removal of Hg(II) using synthesized FeS_2 as a function of initial Hg(II) concentration: (a) saturation function fit for uptake on pyrite; (b) power law fit for uptake on pyrite; and (c) pH at various initial Hg(II) concentrations. FeS_2 = 0.1 g/L, initial concentration of Hg(II) =5, 10, 25, 50, 100, 200, 300, 400, 450, and 500 μmol/L, initial concentrations of salts (Na_2SO_4, $NaNO_3$) = 0.01 mol/L, initial pH = 8, contact time = 1, 3, and 7 days.

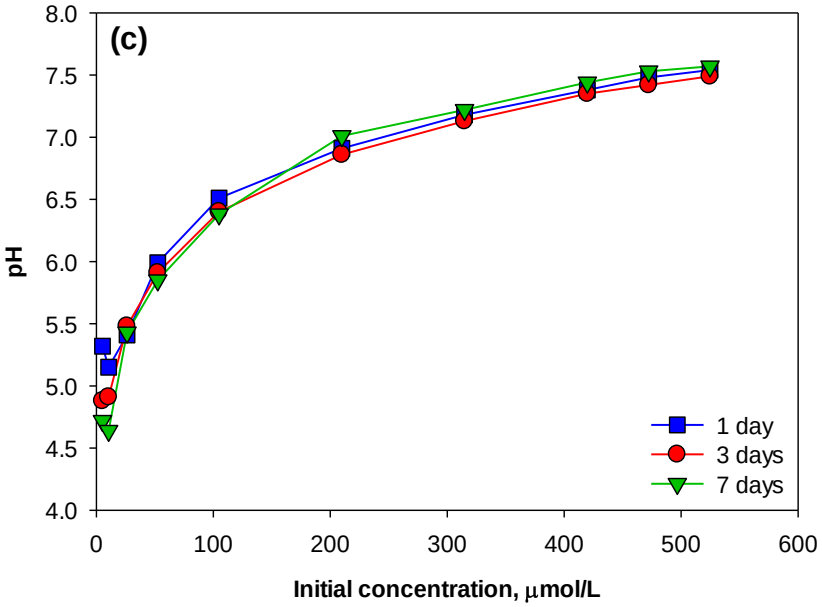

Figure 3.5 Continued.

Table 3.3 Model parameters for mercury-loading tests with salts.

Models	Contact time		
	1 day	3 days	7 days
Saturation function relationship			
b (L/μmol)	0.15 ± 0.073	0.46 ± 0.17	0.84 ± 0.40
a (μmol/g)	374 ± 28	388 ± 18	406 ± 19
R^2	0.78	0.89	0.89
Goodness of fit parameters	0.22	0.15	0.15
Power law relationship			
a ($\mu mol^{1-1/n}L^{1/n}/g$)	116 ± 30	155 ± 25	187 ± 29
b	0.20 ± 0.048	0.17 ± 0.030	0.14 ± 0.029
R^2	0.77	0.86	0.84
Goodness of fit parameters	0.22	0.16	0.18

3.3.4 Effect of Mercury Loading: Adsorption of Hg(II) with Humic Acids

3.3.4.1 5 mg/L Humic Acids

Effects of humic acids on removal of Hg(II) using pyrite (FeS_2) were studied as a function of initial Hg(II) concentration at pH 8 in a series of batch tests where no buffer was applied. Initial mercury concentrations of 5, 10, 25, 50, 100, 200, 300, 400, and 450 μmol/L and the 0.1 g/L of pyrite were applied. Humic acids were added at a concentration of 5 mg/L to the solid suspension as described above. As shown in Figure 3.6, higher pyrite uptake (q) observed at higher initial Hg(II) concentration and at longer contact times. The data for each contact time were fitted with a saturation function relationship and a power law relationship, as shown in Figure 3.6 (a) and (b) and the model parameters are listed in Table 3.4. Similar to the result in the absence of salts, the power law relationship was better able to correlate the data in the presence of 5 mg/L HAs. Maximum pyrite uptake of Hg(II) (450 μmol/g) in the presence of 5 mg/L HAs was much lower than that observed in absence of salts (900 μmol/g), but a little higher than that in the presence of salts (400 μmol/g). An earlier study of mercury sorption on Fe and Mn hydroxides shows a similar effect in that addition of HAs inhibited Hg^{2+} adsorption.[79] This phenomena could be due to the competition between Hg^{2+} and HAs for binding sites on the pyrite surface or due to the formation of soluble Hg-HAs complexes that are less able to be adsorbed by pyrite. Furthermore, HAs may also tend to complex with HgS that is formed in the system and result in less removal of mercury from solution.[80, 81] The pH increased as the initial concentration of Hg(II) increased (Figure 3.6 (c)).

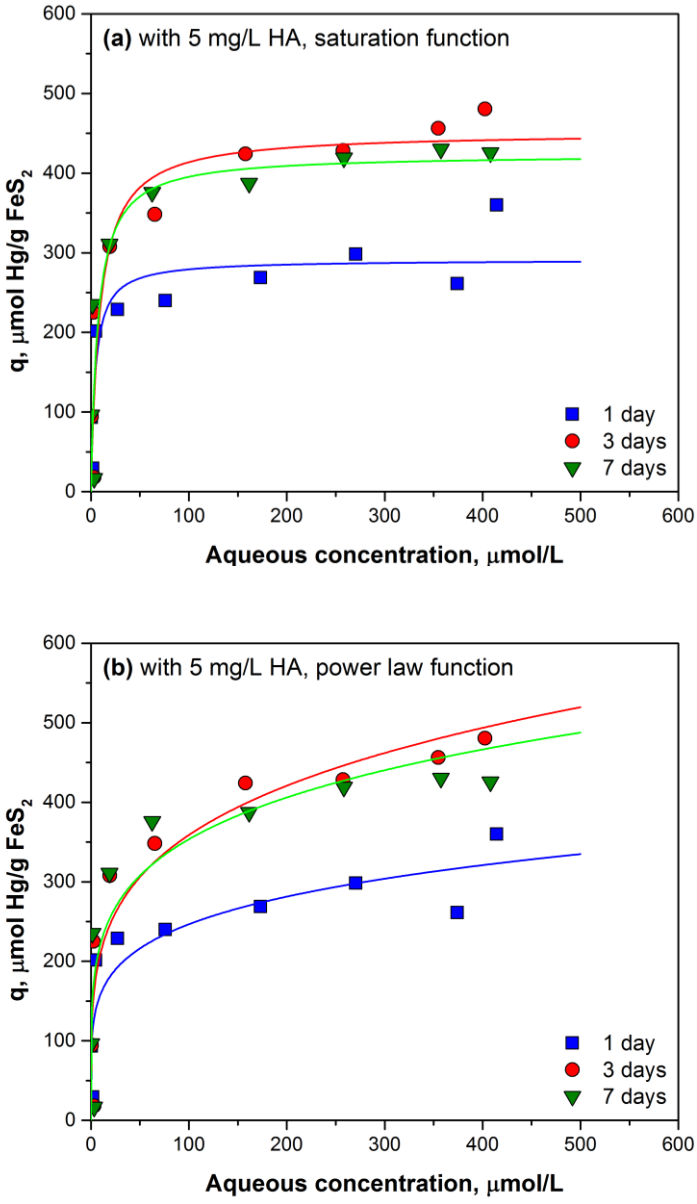

Figure 3.6 Effects of humic acids on removal of Hg(II) using synthesized FeS_2 as a function of initial Hg(II) concentration: (a) saturation function fit for uptake on pyrite; (b) power law fit for uptake on pyrite; and (c) pH at various initial Hg(II) concentrations. FeS_2 = 0.1 g/L, initial concentration of Hg(II) =5, 10, 25, 50, 100, 200, 300, 400, and 450 μmol/L, initial concentration of HAs = 5 mg/L, initial pH = 8, contact time = 1, 3, and 7 days.

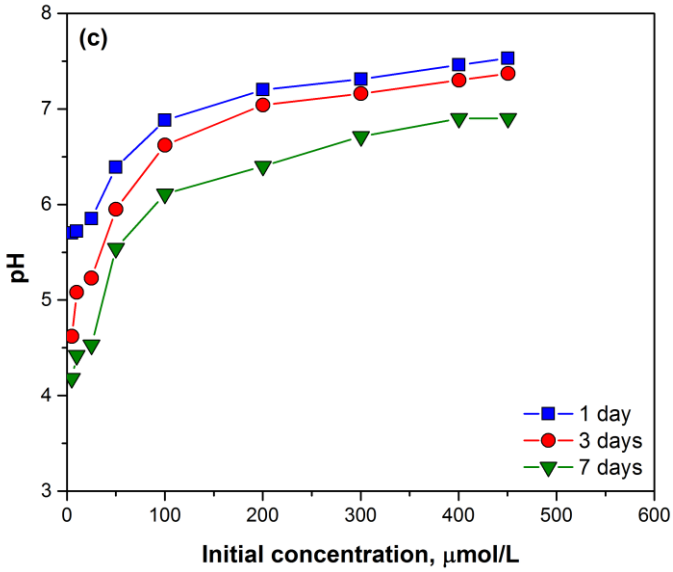

Figure 3.6 Continued.

Table 3.4 Model parameters for mercury-loading tests in the presence of 5 mg/L humic acids.

Models	Contact time		
	1 day	3 days	7 days
Saturation function relationship			
b (L/μmol)	0.23 ± 0.12	0.11 ± 0.059	0.14 ± 0.093
a (μmol/g)	291.3 ± 23.1	451.3 ± 37.3	423.6 ± 41.4
R^2	0.76	0.82	0.72
Goodness of fit parameters	0.23	0.23	0.27
Power law relationship			
a ($\mu mol^{1-1/n}L^{1/n}/g$)	102.8 ± 25.5	124.4 ± 31.9	140.7 ± 38.1
b	0.19 ± 0.048	0.23 ± 0.049	0.20 ± 0.052
R^2	0.76	0.83	0.74
Goodness of fit parameters	0.25	0.22	0.26

3.3.4.2 10 mg/L Humic Acids

All experimental conditions in this section were the same as described in section 3.3.4.1 except that 10 mg/L HAs was added into the solution. The results are shown in Figure 3.7. As seen previously, higher uptake (q) was observed at higher Hg(II) doses and at longer contact time, but the maximum uptake of pyrite for Hg(II) (525 μmol/g) was slightly higher than experimental results obtained at 5 mg/L HAs (450 μmol/g). Removal data were fitted with a saturation function and a power law relationship (Figure 3.7 (a) and (b)), and all model parameters are listed in Table 3.5. It was found that the saturation function relationship is better to predict the experimental data. In addition, Figure 3.7 (c) shows that the patterns of variation of pH in the experiment with 10 mg/L HAs were similar to those for the experiment with 5 mg/L HAs.

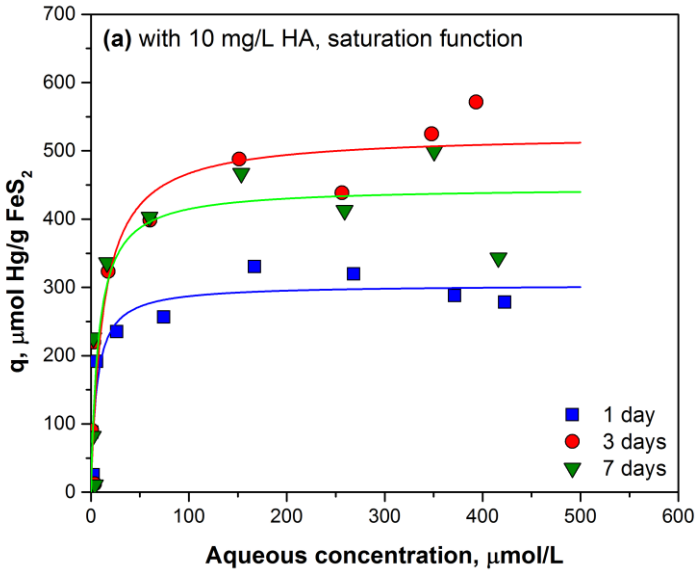

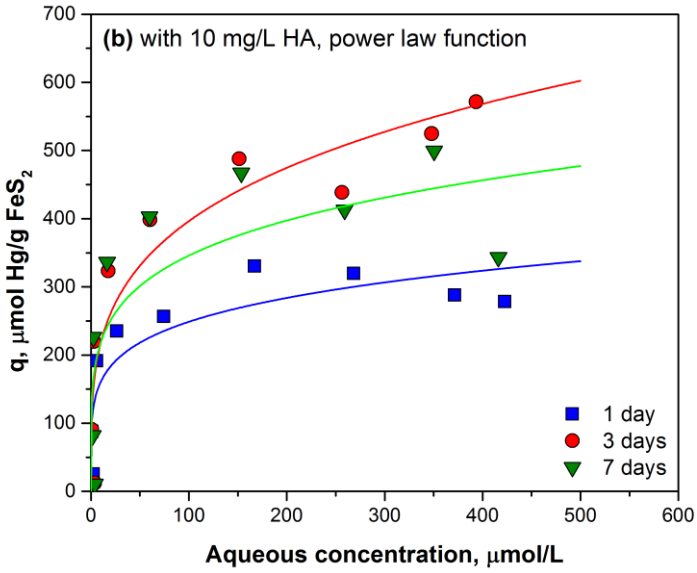

Figure 3.7 Effects of humic acids on removal of Hg(II) using synthesized FeS_2 as a function of initial Hg(II) concentration: (a) saturation function fit for uptake on pyrite; (b) power law fit for uptake on pyrite; and (c) pH at various initial Hg(II) concentrations. FeS_2 = 0.1 g/L, initial concentration of Hg(II) =5, 10, 25, 50, 100, 200, 300, 400, and 450 μmol/L, initial concentration of HAs = 10 mg/L, initial pH = 8, contact time = 1, 3, and 7 days.

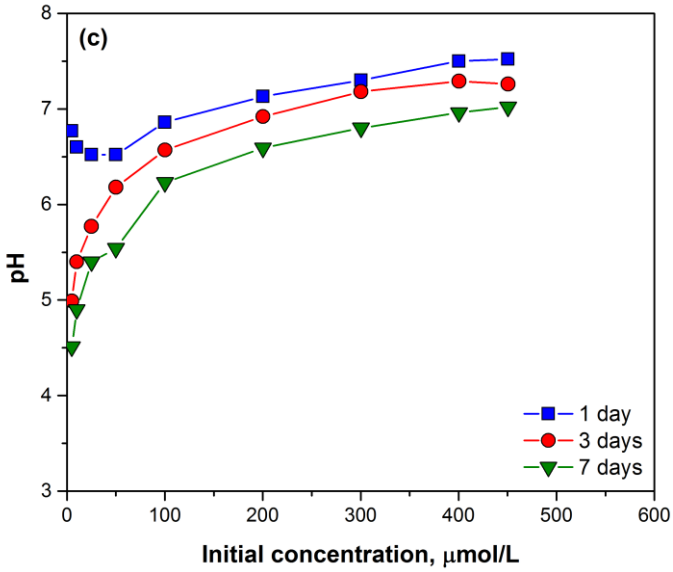

Figure 3.7 Continued.

Table 3.5 Model parameters for mercury-loading tests in the presence of 10 mg/L humic acids.

Models	Contact time		
	1 day	3 days	7 days
Saturation function relationship			
b (L/μmol)	0.17 ± 0.061	0.081 ± 0.037	0.13 ± 0.069
a (μmol/g)	303.9 ± 18.5	524.5 ± 42.4	446.6 ± 43.7
R^2	0.87	0.86	0.75
Goodness of fit parameters	0.17	0.22	0.27
Power law relationship			
a ($\mu mol^{1-1/n}L^{1/n}/g$)	103.7 ± 28.0	119.7 ± 34.9	137.7 ± 51.4
b	0.19 ± 0.052	0.26 ± 0.055	0.20 ± 0.072
R^2	0.72	0.84	0.60
Goodness of fit parameters	0.25	0.23	0.35

3.3.4.3 20 mg/L Humic Acids

A concentration-dependent removal test for Hg(II) was also conducted in the presence of 20-mg/L HAs and the results are shown in Figure 3.8. Similarly as in the other experiments, higher initial Hg(II) concentrations and longer contact times resulted in more Hg(II) removal. However, the uptake on pyrite (q) for 3-day contact were much lower than for the test with lower HAs concentrations for the same contact time. This removal behavior is expected and could possibly be due to involvement of a complexation reaction between Hg(II) and HAs. The increase in HAs concentration from 10 to 20 mg/L did not significantly change the adsorption. The maximum uptake of Hg(II) on pyrite was 545 μmol/g. Similar to the case with 10 mg/L HAs, the saturation function relationship is better able to predict the data than the power law equation (Figure 3.8 (a) and (b)). All model parameters are listed in Table 3.6. In addition, the pattern of variation of pH in the experiment with 20 mg/L HAs was similar to those of the other experiments.

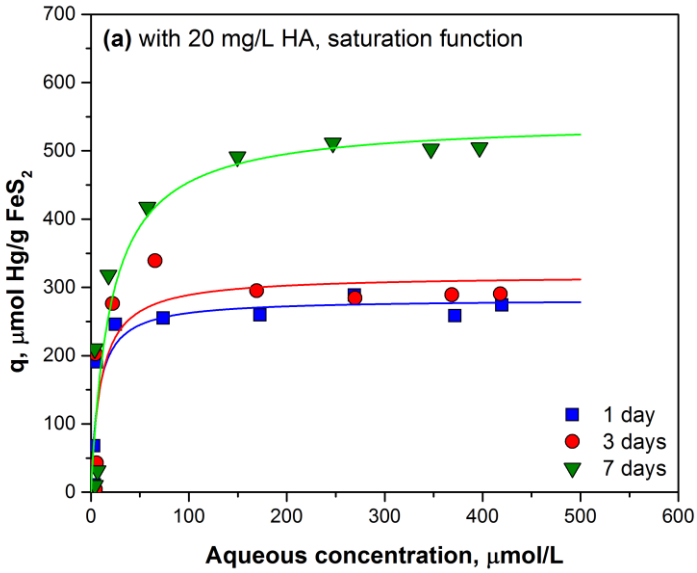

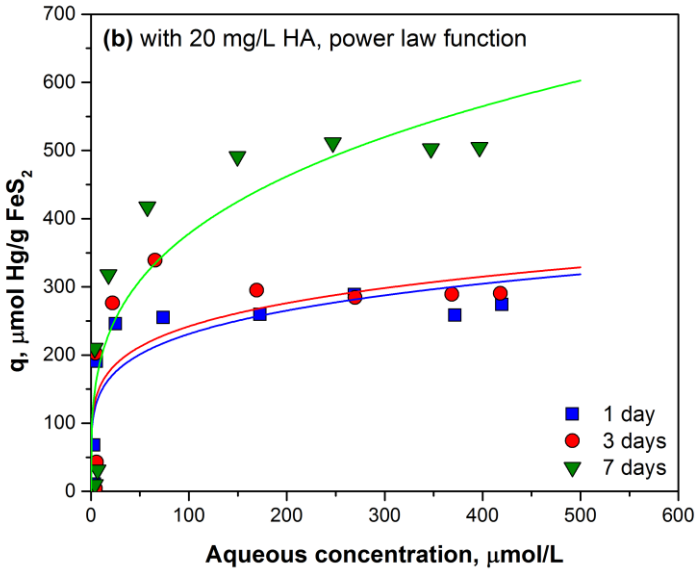

Figure 3.8 Effects of humic acids on removal of Hg(II) using synthesized FeS_2 as a function of initial Hg(II) concentration: (a) saturation function fit for uptake on pyrite; (b) power law fit for uptake on pyrite; and (c) pH at various initial Hg(II) concentrations. FeS_2 = 0.1 g/L, initial concentration of Hg(II) =5, 10, 25, 50, 100, 200, 300, 400, and 450 μmol/L, initial concentration of HAs = 20 mg/L, initial pH = 8, contact time = 1, 3, and 7 days.

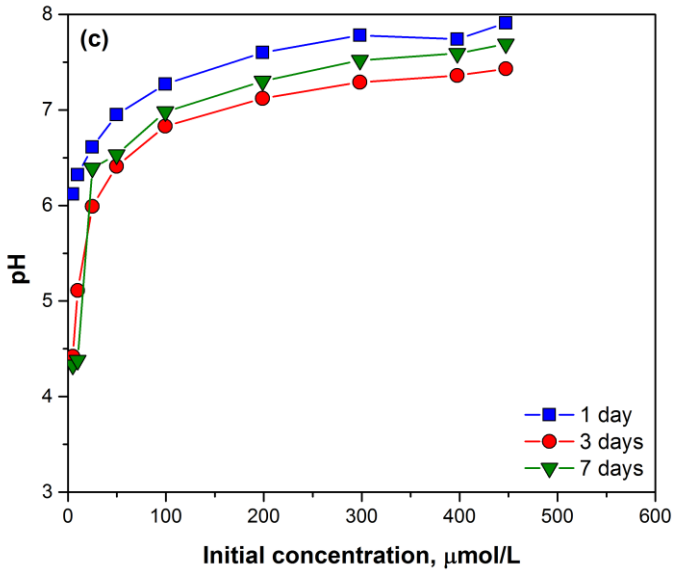

Figure 3.8 Continued.

Table 3.6 Model parameters for mercury-loading tests in the presence of 20 mg/L humic acids.

Models	Contact time		
	1 day	3 days	7 days
Saturation function relationship			
b (L/µmol)	0.13 ± 0.055	0.10 ± 0.059	0.05 ± 0.021
a (µmol/g)	282.7 ± 22.2	317.7 ± 36.2	544.9 ± 46.2
R^2	0.80	0.67	0.87
Goodness of fit parameters	0.22	0.31	0.22
Power law relationship			
a ($\mu mol^{1-1/n}L^{1/n}/g$)	91.9 ± 31.6	100.9 ± 45.0	99.4 ± 40.2
b	0.20 ± 0.067	0.19 ± 0.087	0.29 ± 0.076
R^2	0.60	0.45	0.76
Goodness of fit parameters	0.30	0.39	0.30

The effect of HAs concentration on the maximum uptake of Hg(II) on pyrite is shown in Figure 3.9. The presence of HAs generally inhibited the adsorption of Hg(II), which is in agreement with previous studies of adsorption of Hg onto Fe and Mn hydroxides.[79] The reduced sulfur groups of HAs may form Hg-HAs complexes, which might have less affinity for pyrite than Hg(II) that is uncomplexed or complexed with other ligands. Previous studies show that humic substances, particularly humic acids, would decrease the growth rate of HgS,[82, 83] which is the final stable phase for Hg(II) in contact with pyrite. Furthermore, formation of Hg-HAs complexes would increase the solubility of HgS.[80, 81] However, the effect of increasing the concentration of HAs above 5 mg/L was much less than the effect of increasing it from 0 to 5 mg/L. Addition of high concentrations of HAs could result in formation of higher concentrations of Hg-HAs complexes that could aggregate to sizes large enough to be removed by the 0.02-μm membrane filter, which would appear to increase dissolved Hg(II) removal.

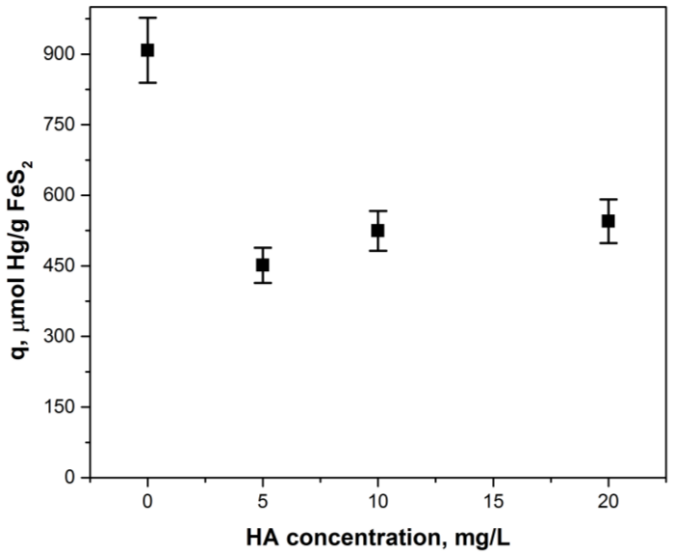

Figure 3.9 Plot of maximum pyrite uptake of Hg(II) vs concentration of humic acids.

3.3.4.4 SEM/EDS Analysis

The solid samples obtained from the experiment with initial mercury concentration of 450 μmol/L and at day-7 contact time in the presence of HAs were analyzed by SEM/EDS. The results are shown in Figure 3.10. The morphology of solid phases did not change much after contact with mercury. EDS results (Figure 3.11) indicate that the S/Fe ratio for each sample was around 2, which confirms that the particles are mainly pyrite. Mercury peaks were not detected for these samples because of relatively high detection limit of the EDS for identification of elements.

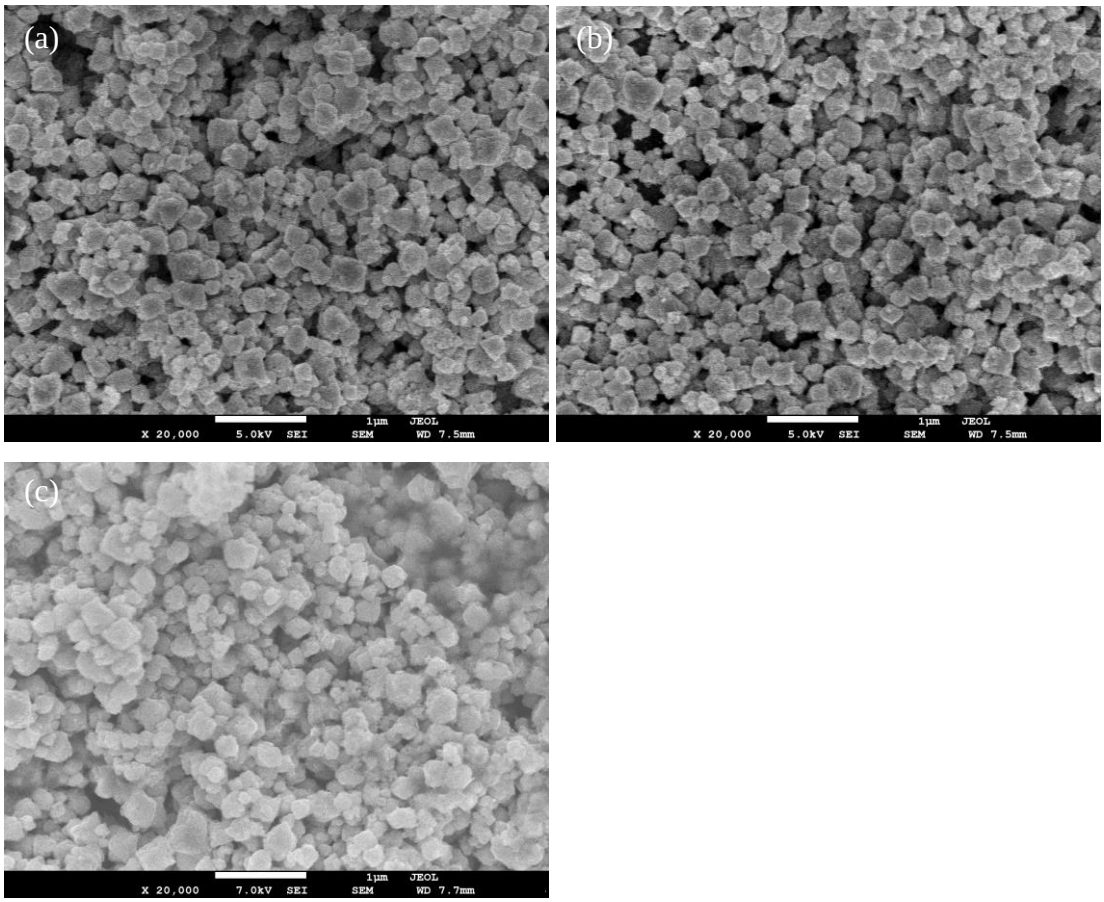

Figure 3.10 SEM micrographs of selected samples with humic acids, with initial Hg(II) concentration of 450 μmol/L: (a) 5 mg/L HAs, (b) 10 mg/L HAs, (c) 20 mg/L HAs.

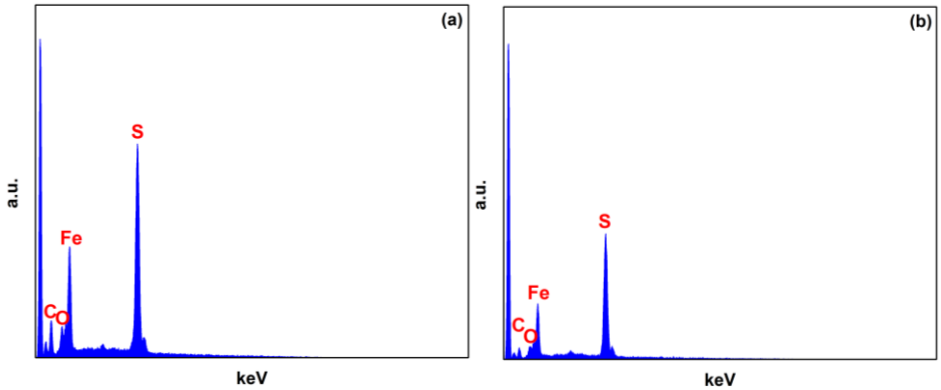

Figure 3.11 EDS analysis of selected samples obtained at 450 μmol/L of initial Hg(II) concentration in the presence of HAs: (a) 10-mg/L HAs, (b) 20-mg/L HAs.

3.3.4.5 XPS Analysis

The surface of solid samples obtained from the Hg(II) removal test in the presence of 5 mg/L and 20 mg/L HAs at day-7 contact time were characterized by XPS analysis. Figures 3.12 and 3.13 show the XPS spectra collected from broad scans with a range of binding energy from 0 eV to 1200 eV and they indicate that the solid surface consisted of iron, oxygen, sulfur, carbon, and mercury. Carbon was mainly from the carbon tape, which was used to hold particles on the sample holder. Compared with pure FeS_2 (Figure 2.14), the intensity of Fe 2p peak in broad scan was greatly reduced, but a higher intensity of the Hg 4f peak was observed. This is expected because solid mercury species were formed on the surface of pyrite. The atomic concentrations for these elements are listed in Tables 3.7 and 3.8. The ratio of S was higher than that of Hg and much higher than that of Fe, indicating that S was found in the forms of both mercury sulfide and iron sulfide. To confirm the surface species, high resolution XPS spectra for Fe 2p, S 2p, and Hg 4f were also collected with low pass energy (20 eV).

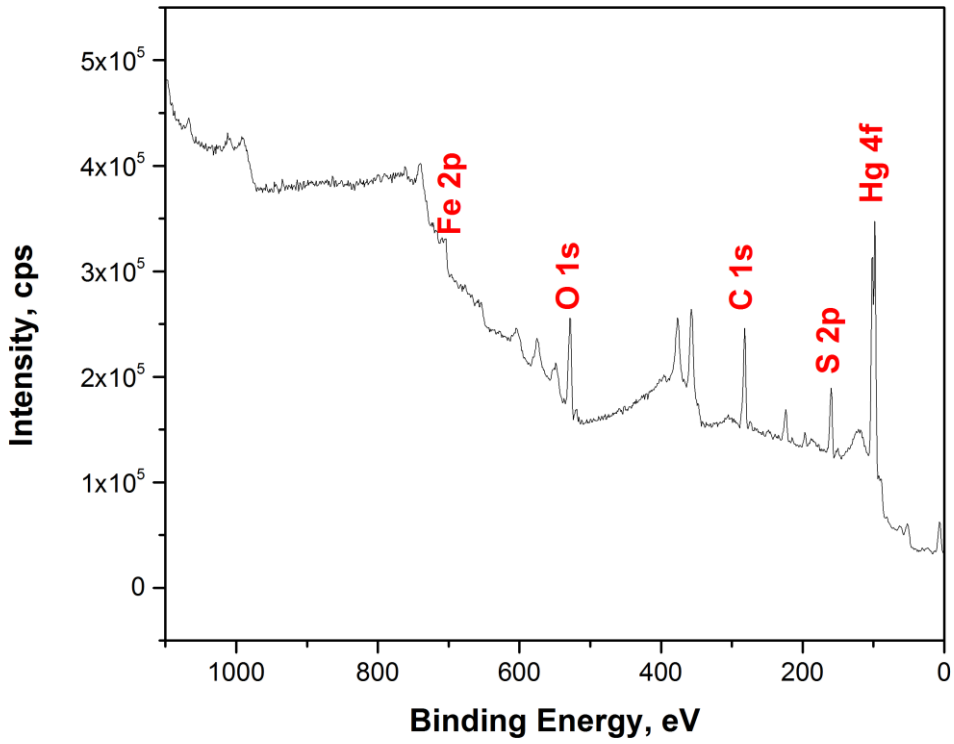

Figure 3.12 Broad scan XPS spectrum for sample with 5 mg/L HAs, initial Hg concentration of 450 μmol/L and contact for 7 days.

Table 3.7 XPS analysis for the sample with 5 mg/L HAs, initial Hg concentration of 450 μmol/L and contact for 7 days.

Atomic Concentration (%)				
O 1s	C 1s	Hg 4f	S 2p	Fe 2p
18.2	50.5	13.2	17.1	1.0

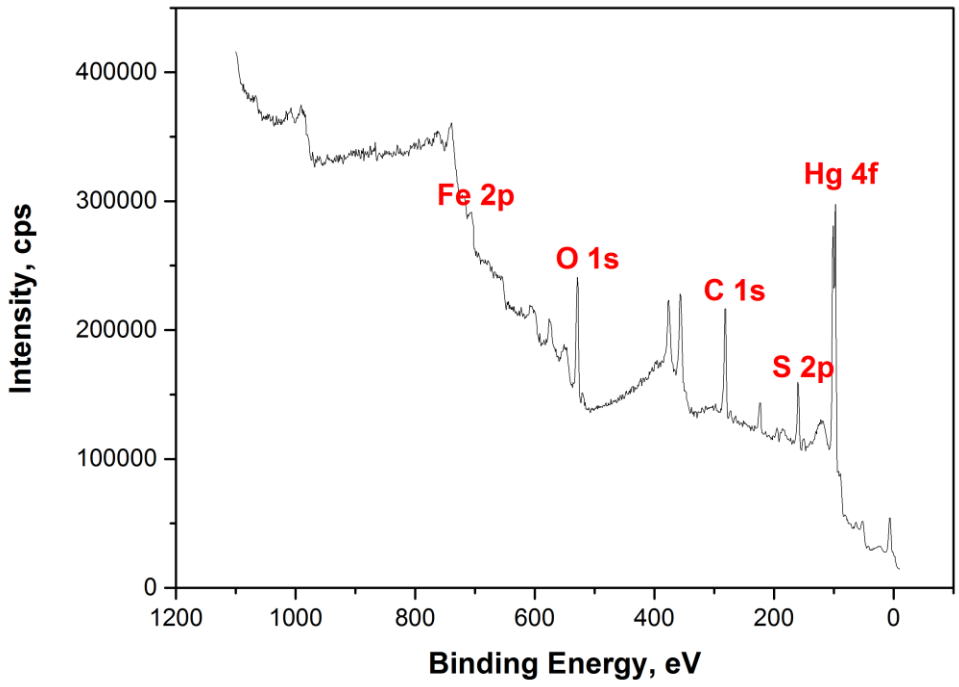

Figure 3.13 Broad scan XPS spectrum for sample with 20 mg/L HAs, initial Hg concentration of 450 μM and contact for 7 days.

Table 3.8 XPS analysis for the sample with 20 mg/L HAs, initial Hg concentration of 450 μmol/L and contact for 7 days.

Atomic Concentration (%)				
O 1s	C 1s	Hg 4f	S 2p	Fe 2p
22.8	48.8	10.4	15.7	2.3

Fe 2p, S 2p, and Hg 4f spectra of solid samples obtained from mercury loading test with initial Hg concentration of 450 μmol/L and contact time of 7 days in the

presence of 5 mg/L HAs are shown in Figure 3.14, and the parameters are listed in table 3.9, respectively. The binding energy at 707.5 eV and 711.4 eV are two peaks of Fe 2p3/2 and they were identified to be the characteristic peaks of pyrite and Fe(III), respectively.[71] The major peak of S 2p3/2 was found at binding energy of 162.7 eV which indicated that sulfide on the surface.[71] The peak at 101.09 eV in Hg 4f spectra indicates HgS was formed.[34, 71]

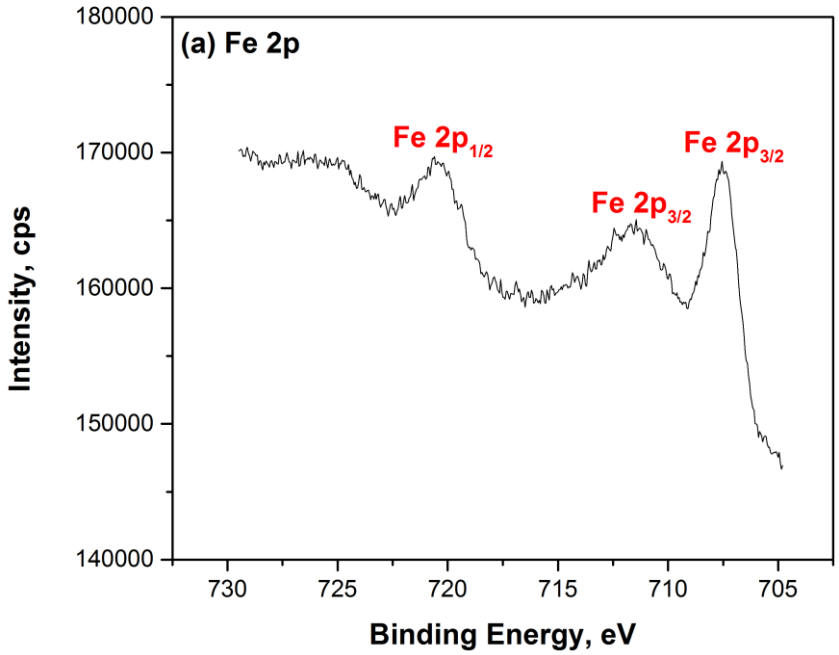

Figure 3.14 High resolution XPS spectra for sample from mercury loading test in the presence of 5 mg/L HAs and surface species analysis (initial Hg concentration = 450 μmol/L, contact for 7 days). (a) narrow scan of Fe 2p spectra; (b) narrow scan of S 2p spectra; (c) narrow scan of Hg 4f spectra.

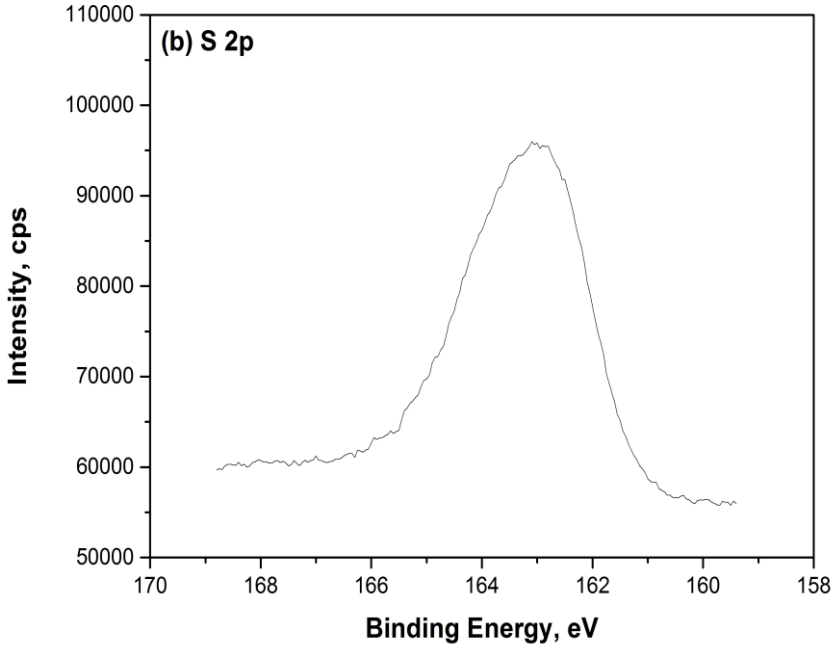

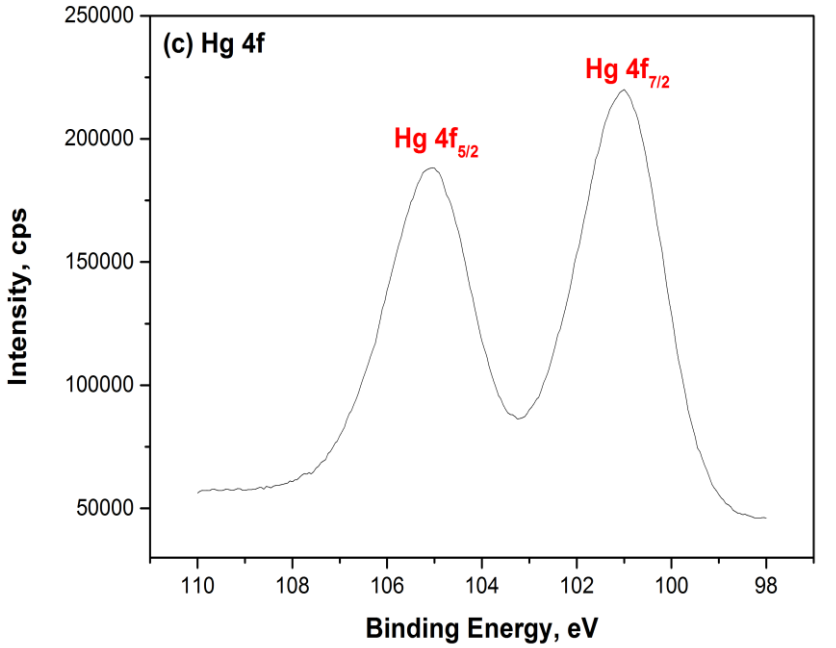

Figure 3.14 Continued.

Table 3.9 XPS peak parameters of sample from mercury loading test with 5 mg/L HAs (initial Hg concentration = 450 μmol/L, contact for 7days).

Binding Energy (eV)		FWHM (eV)	Area (%)	Surface species
Fe $2p_{3/2}$	707.5	1.47	27.45	Fe(II)-S
	711.4	4.28	47.97	Fe (III)
Fe $2p_{1/2}$	720.4	2.01	15.13	--
	725.0	3.19	9.45	--
S $2p_{3/2}$	162.7	1.47	60.24	Sulfide/S_2^{2-}
S $2p_{1/2}$	163.9	1.47	39.76	--
Hg $4f_{7/2}$	101.09	1.69	55.37	HgS
Hg $4f_{5/2}$	105.1	1.79	44.63	--

Fe 2p, S 2p, and Hg 4f spectra of solid samples obtained from mercury loading test with initial Hg concentration of 450 μmol/L and contact time of 7 days in the presence of 20 mg/L HAs are shown in Figure 3.15, and the parameters are summarized in Table 3.10. Similarly as found in the presence of 5 mg/L HAs, the Fe $2p_{3/2}$ peaks were found at binding energy of 707.4 eV and 711.4 eV and they were identified to be the characteristic peaks of pyrite and Fe(III).[71] The major peak of S $2p_{3/2}$ was observed at 162.7 eV, representative of sulfide.[71] The binding energy at 101.03 eV in Hg 4f spectra indicates divalent Hg specie, possibly leading to formation of HgS when we consider ratio of Hg to S together with the presence of sulfide.[34, 71]

Both results indicated the presence of HgS in the sample, which was in agreement with the conclusion in Section 3.3.2. Formation of HgS on the surface suggested that mercury removal by pyrite was not only adsorption, but also surface precipitation.

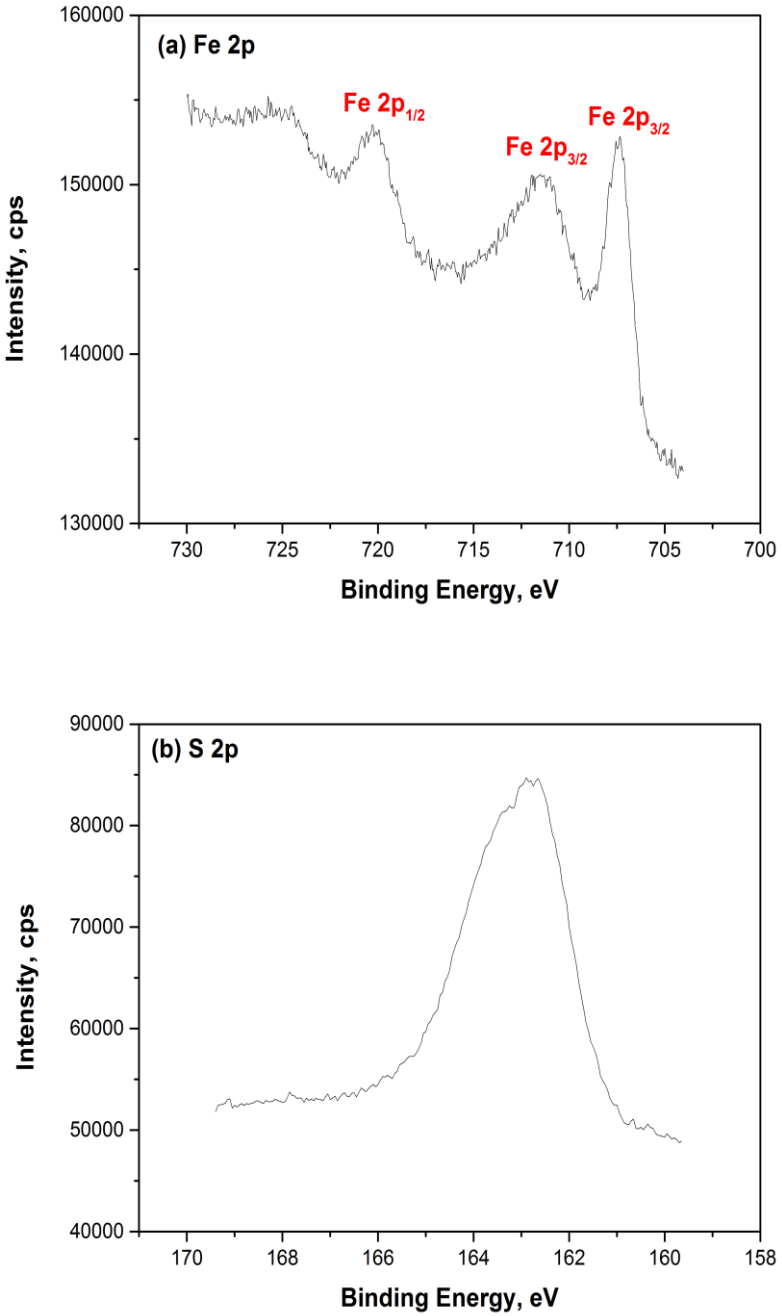

Figure 3.15 High resolution XPS spectra for sample from mercury loading test in the presence of 20 mg/L HAs and surface species analysis (initial Hg concentration = 450 μmol/L, contact for 7 days). (a) narrow scan of Fe 2p spectra; (b) narrow scan of S 2p spectra; (c) narrow scan of Hg 4f spectra.

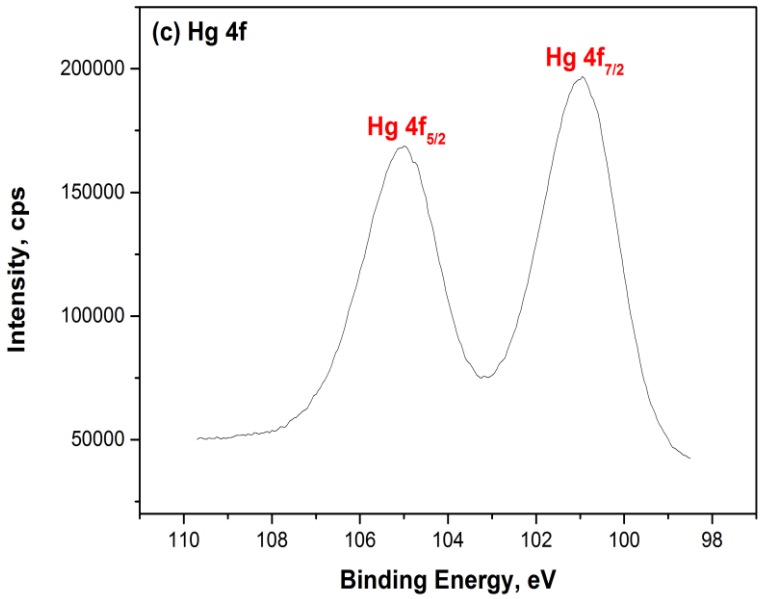

Figure 3.15 Continued.

Table 3.10 XPS peak parameters of sample from mercury loading test with 20 mg/L HAs (initial Hg concentration = 450 μmol/L, contact for 7days).

Binding Energy (eV)		FWHM (eV)	Area (%)	Surface species
Fe $2p_{3/2}$	707.4	1.25	23.35	Fe(II)-S
	711.4	3.99	51.75	Fe (III)
Fe $2p_{1/2}$	720.2	1.93	13.64	--
	724.8	2.9	11.25	--
S $2p_{3/2}$	162.7	1.47	62.08	Sulfide/S_2^{2-}
S $2p_{1/2}$	163.85	1.47	37.92	--
Hg $4f_{7/2}$	101.03	1.65	55.25	HgS
Hg $4f_{5/2}$	105.08	1.74	44.74	--

3.4 Conclusion

Mercury removal by pyrite was observed with initially fast kinetics. It was found that 0.1 g/L pyrite was able to remove about 90% of 5 μmol /L Hg(II) in 5 minutes or less. However, mercury was then released, before being readsorbed to give substantially complete mercury removal after 12 hours. Release of mercury could be caused by formation of soluble Hg-polysulfide-sulfide complexes. Resorption of Hg could be caused by changes in the surface due to surface reactions or by changes in the soluble complexes that result in complexes that are more likely to be adsorbed by pyrite. The pH in all kinetic experiments was observed to be much lower than in the solution before addition of pyrite. Two factors could lead to pH drop: one is the hydrogen ions released from the pyrite surface and the other one is the reaction of the pyrite surface with Hg(II). The presence of two salts at concentrations of 0.01 mol/L decreased mercury removal by about 20%. The maximum sorption capacity of pyrite was found to be 900 μmol Hg/g FeS_2 in the absence of salts and humic acids. Large pH drop was observed at low doses of Hg(II) and was due to the two factors discussed above. While, the rise in pH as more Hg(II) was added and removed could be due to the existence of two different surface sorption sites that have different affinities for Hg(II) and different effects on pH. One site might adsorb Hg(II) more strongly and release protons. This would result in reductions in pH. Another site might sorb Hg(II) less strongly and consume protons. Both salts and humic acids inhibit removal of Hg(II) by pyrite. However, this inhibition was observed at the lowest concentration of humic acids and was not observed to increase at higher concentrations. The effect of humic acids could be due to it competing

with Hg(II) for the binding sites on pyrite, or by forming soluble Hg-HAs complexes. The analyses of samples by XPS found Hg 4f spectra that indicated the presence of HgS on the surface, which suggests that mercury removal by pyrite was not only an adsorption process, but also a surface precipitation process.

CHAPTER IV

APPLICATION OF A REACTIVE ADSORBENT-COATED SUPPORT SYSTEM FOR REMOVAL OF MERCURY(II)

4.1 Introduction

Previous studies demonstrated that pyrite and other iron sulfides species, such as mackinawite (FeS), are excellent absorbents for removing mercury from water and that they can form stable residuals.[37-42] Furthermore, the results from experiments in batch reactors described in Chapter III also showed evidence that pyrite has strong removal capability for Hg(II) by forming HgS solids. However, a key problem in applying near nano-scale particles of pyrite is that they cannot be allowed to leave with the treated water as they contain the adsorbed mercury. Attaching the pyrite particles to larger particles, such as sand, could be a solution to keep them within the treatment system. Three methods of attaching pyrite particles to sand were studied in this research. One method is to attach particles to the surface of a support media through electrostatic forces, where pH is a critical factor for optimal coating. The pH is important because it determines surface charges that define electrostatic forces between the sand and pyrite particles. An important characteristic of particles is their point of zero charge (PZC), which is the pH at which the surface charge is zero. Studies of coating goethite or FeS on sand found that the maximum coating occurred around the PZC of the particles.[49, 50] Aging time and influent concentration could also affect coating efficiency, but they are

not as important as pH.[50, 51] In this research, we evaluated two parameters that affect the coating efficiency, including pH and the pyrite to sand ratio (P/S).

Another approach to attach pyrite on the sand is to directly form pyrite on the sand surface. Results shown in Chapter II showed that FeS was first formed after mixing $FeCl_3$ with NaSH. Since FeS could be successfully coated on both untreated sand and chemically-treated sand at pH 5.5,[50] we coated FeS onto sand first and then applied microwave irradiation as a method to covert FeS-coated sand to pyrite-coated sand.

The third method for attaching near nano-scale pyrite particles to sand particles uses a polymer-based coating and leads to formation of polyelectrolyte multilayer films (PMF) to incorporate nanoparticles. In the presence of oppositely charged substrate, the polyelectrolytes could form a layer-by-layer uniform film of polymer, which could immobilize the nanoparticles on the surface of the sand.[52-54]

In order to provide good contact with the water being treated, pyrite-coated sands were placed in a column. Water to be treated would pass through the column and the near nanoparticles would be retained in the column on the support material. Effects of pH, hydraulic retention time (HRT), salts (nitrate and sulfate), and humic acids on mercury removal by pyrite-coated sands were studied. The system developed was called reactive adsorbent-coated support (RACS) system that aims to produce high quality water from mercury-contaminated wastewater and to produce stable final residuals that can be safely disposed to landfill.

4.2 Materials and Method

Chemicals applied in this research were analytical grade or higher. The deionized (DI) water (Milli-Q, Millipore) used in all experiment was deoxygenated by sparging with ultra-high purity (UHP) nitrogen for 2 hours outside the chamber and then for 24 hours inside an anaerobic chamber (Coy Laboratory Products Inc.), which was filled with UHP nitrogen.

4.2.1 Pyrite Synthesis and Sand Preparation

Pyrite synthesis was conducted in the anaerobic chamber following the procedures developed in Chapter II. Pyrite particles were prepared by mixing 15 mL of 0.1 mol/L iron(III) chloride hexahydrate (97%, Sigma-Aldrich) and 15 mL of 0.2 mol/L sodium hydrosulfide hydrate (Sigma-Aldrich). The pH was adjusted to 4.5 by addition of 1 mol/L NaOH.[55, 56] The mixture was then irradiated by a commercial microwave (Emerson MW8779W, output 800 W, 2450 MHz) for 1 min at 100% power level. A microwave digestion bomb (45 mL, Parr Instrument Company) was used as the container to avoid possible explosion due to the high pressure and temperature. A 10-mL volume of concentrated HCl (J.T. Baker) was added into the mixture to dissolve excess FeS without destroying crystalline pyrite.[62] Then, the solid phase was collected by vacuum filtration with a 0.02-μm anodisc type 13 membrane filter (47 mm-diameter, Whatman) and washed several times with acetone and carbon disulfide to removal residual sulfur from the solid surface.[43] The synthesized solids were then dried inside the anaerobic chamber. The particle sizes ranged from 100 nm to 200 nm (Figure 2.9 (f)).

Sand (50-70 mesh) purchased from Sigma-Aldrich was used in this research. Chemical treatment procedures for the sand followed methods developed by Han et al.[50] The raw sand was washed several times with DI water until the rinse water was clear and then rinsed with DI water for 24 hours. In order to remove any natural minerals and impurities that remain on the sand surface, the DI washed sand was then rinsed with solutions of 1 mol/L sodium dithionite, 12 mol/L hydrochloric acid, and 15% hydrogen peroxide each for 24 hours. Between each rinse, the sand was washed with DI water 20-30 times to remove excess chemicals. The sand was then dried for future use.

4.2.2 Coating of Sand with Pyrite

4.2.2.1 Fe Content on Sand

The Fe contents of raw sand and treated sand were studied. Concentrated nitric acid was used as the extraction acid and the sand was soaked in concentrated HNO_3 for 24 hours. The extraction solution was then diluted to determine the Fe concentration by Ferrozine method (Appendix C), which used a UV-Visible spectrophotometer (Heλios, Thermo Spectronic) to measure the absorbance of the solution at 562 nm. The results are listed in Table 4.1. The raw sand contained 0.14 milligram natural Fe per gram sand. Washing and rinsing with DI water did not remove any natural Fe-containing compounds from the sand surface. But after washing with chemicals, the natural Fe was largely removed (about 57%). The amount of Fe on chemically-treated sand was only 0.06 mg/g. Therefore, the chemically-treated sand was chosen for further study.

Table 4.1 Fe content on different sands.

Sand treatment	Amount of Fe on sand (mg/g)
Raw sand	0.14
DI washed sand	0.14
Chemically-treated sand	0.06

4.2.2.2 Electrostatic Attraction Coating

To coat the sand with pyrite, 20 g of chemically-treated sand was combined with 20 mL of 1 g/L FeS_2 in a 40-mL glass vial and continuously mixed by an end-over-end rotator in the anaerobic chamber for several days until the supernatant was clear. Then the pH of the mixture was measured and the supernatant was discarded. In order to examine the effect of rinsing, a portion of the pyrite-coated sands was rinsed for 24 hours (six consecutive DI water rinses within 1 hour and then additional one day contact with DI water) and a portion was not rinsed. Both portions of coated sand were dried inside the anaerobic chamber.

Two coating pH values (4 and 7) were studied and the desired pH of the solution was adjusted with dilute NaOH or HCl. The effect of pyrite to sand (P/S) ratio (2 mg/g, 1 mg/g, and 0.5 mg/g) on coating efficiency was also considered in experiments conducted by adding different volumes of a 1-g/L pyrite suspension. The amount of Fe on coated sand was determined by extracting Fe with concentrated HNO_3 for 24 hours and measuring the concentration of Fe by the Ferrozine method (Appendix C).

4.2.2.3 Pyrite Synthesis on Sand Surface

Another approach to attach pyrite on the sand is to directly form pyrite on sand surface. The procedure was similar with pyrite synthesis using microwave irradiation in Chapter II. But after mixing 15 mL 0.1 mol/L Fe(III) and 15 mL 0.2 mol/L NaHS in glass vials, the pH was adjusted to 5. And then 10 g of chemically-treated sand was added into the mixture and mixing by an end-to-end rotator for 1 day to coat FeS on sand. After 1 day, the suspension was aging with microwave (100% power level) for 1 minute. The sand was then washed with acetone and carbon disulfide and dried inside the anaerobic chamber. The amount of Fe on coated sand was extracted by concentrated HNO_3 for 24 hours and the concentration was determined by Ferrozine method (Appendix C).

4.2.2.4 Polymer-Based Coating

The third method to attach the pyrite particles to the sand surface uses polymers. Polyallylamine hydrochloride (PAH, MW=120,000-200,000), which is positively charged, was used for the first layer and polyacrylic acid (PAA, MW=5000) was used for the second layer. 50 g chemically-washed sand was added into 100 mL of 0.4 mmol/L PAH at pH 4 and stirred for 20 min and then the sand was washed 4 times with DI water. After discarding the supernatant, 100 mL 0.4 mmol/L PAA at pH 4 was added and stirred for another 20 min. Then the sand was washed 4 times with DI water to remove excess polymers. After the sand was dried, a volume of 1-g/L FeS_2 suspension at pH 4 was mixed with the sand and the mixture was rotated for 3 days by an end-to-end

rotator. The supernatant was then discarded and the coated sand was dried inside the anaerobic chamber. The amount of Fe on coated sand was determined by extracting Fe with concentrated HNO_3 for 24 hours and measuring the concentration of Fe by the Ferrozine method (Appendix C).

4.2.3 Reactive Adsorbent-Coated Support System

A chromaflex column (74 mL volume, 15 cm length, 2.5 cm internal diameter; Kimble & Chase) equipped with a flow adapter (0.3175 cm-outside diameter tubing, Kimble & Chase) and a Masterflex L/S PTFE-Tubing pump system (3-300 rpm, 90-260 VAC, Cole-Parmer) was used in the column experiments in an up-flow mode. An autosampler (Pharmacia LKB Frac 100 Fraction Collector) was used to collect samples from the effluent.

The solubility of pyrite attached to the sand was evaluated by measuring the concentration of Fe in solution after contact with deoxygenated DI water adjusted to pH 5, 7, and 9. pH values higher than 9 or lower than 5 were avoided, due to the possible oxidative dissolution of pyrite at extreme pH. The Fe concentration was determined by the Ferrozine method (Appendix C), which used a UV-Visible spectrophotometer (Heλios, Thermo Spectronic) to measure the absorbance of the solution at 562 nm.

A tracer test was conducted with a non-reactive salt (KBr) to verify the uniformity of columns packed with both chemically-treated sand (without pyrite) and pyrite-coated sand. A 15-mL volume of 1-mg/L bromide solution was added to the column at the start of the test followed by DI water. Samples were collected over a time

interval of 3 min, so the bromide concentration in each sample is a 3-minute average. Furthermore, a blank test was also conducted with 15 mL of a solution containing 1 mg/L Hg(II) and chemically-treated sand (without pyrite) to verify that chemically-treated sand would not remove any Hg(II) by itself.

The material packed into the column consisted of 30 g dry, pyrite-coated, chemically-treated sand. The final column length was 3.5 cm and the porosity for all column experiments was around 0.44-0.45. Before use, the column with packed sand was purged with carbon dioxide for 15 min. A 3-L volume of a solution containing 1 mg/L Hg(II) was prepared with deoxygenated DI water and adjusted to the desired pH (5, 7, 9) with dilute NaOH or HCl. The effect of salts was examined in experiments where 0.01 mol/L sodium nitrate and 0.01 mol/L sodium sulfate were added to the feed solution. Humic acids at concentrations of 10 mg/L or 20 mg/L were added to evaluate its effect on mercury removal. The column was operated in an up-flow mode with flow rate controlled for most experiments around 1-1.08 mL/min, which is equivalent to a pore water velocity of 0.45-0.50 cm/min. However, the flow rate was 2.14 mL/min for the low hydraulic retention time (HRT) test. The effluent samples were collected over a time interval of 10 min (6 min for low HRT test) by the fraction collector. Selected samples were measured for mercury content and pH. The Cold-Vapor Atomic Absorption Spectrophotometry (CVAAS) system consisted of an atomic absorption spectrometer (AAS, Thermo Scientific, Solaar M6) equipped with a continuous flow vapor generation system (Thermo Scientific, VP 100) and was used to analyze Hg (II) in this research. A solution of tin(II) chloride dissolved in 6 mol/L HCl was used to reduce

divalent mercury to metallic mercury for analysis. For comparison purposes, selected samples were passed through a 0.02-μm anodisc type 13 membrane filter (25 mm-diameter, Whatman) prior to analysis.

4.2.4 Microscopic and Spectroscopic Characterization of Pyrite-Coated Sand

After the column test, the coated sand was dried inside the anaerobic chamber and collected for SEM/EDS and XPS analysis. An Omicron NanoTechnology X-ray Photoelectron Spectrometer (XPS) (Germany) with Mg-Kα source was used to obtain the oxidation status of Fe, S, Hg, and C, and chemical composition on the surface of coated sand. The survey scans were recorded with pass energy of 100 eV and the narrow scans used lower pass energy (20 eV or 50 eV) for higher resolution. The spectra peak of C 1s with a binding energy of 284.8 eV was used as a reference to correct expected charging effects. The narrow scan spectra of Fe 2p, S 2p, and Hg 4d were fitted with XPSPEAK41 fitting program with a Gaussian Lorentzian peak function through background-subtraction corrections using a Shirley-type optimization.

A scanning electron microscope (SEM) equipped with an energy dispersive x-ray spectroscope (EDS) (JSM-7500F, Tokyo, Japan) was utilized to study the morphology and chemical composition of pyrite-coated sand. The image was collected at a working distance of 8 mm under an acceleration voltage range of 3 kV to 7 kV at a magnification of 10,000×.

4.3 Results and Discussion

4.3.1 Effect of pH on Electrostatic Attraction Coating

pH is an important factor in attaching pyrite to sand by electrostatic forces. Preliminary work indicated the PZC of pyrite is around 7.7, as shown in Figure 4.1.[84] The extent of attachment was measured at two pH values (4 and 7) and the results are listed in Table 4.2. The concentration of pyrite on the sand was calculated by measuring the total Fe concentration and subtracting the concentration of the natural Fe impurities on chemically-treated sand. A little more pyrite (3.5%-10%) was attached to chemically-treated sand at pH 7, which is close to pH_{pzc} of pyrite, than that at pH 4. This is in agreement with previous study on FeS and the optimal coating pH was expected to be near pH_{pzc} of the surface to be coated.[50] The results also demonstrated that rinsing does not have a substantial effect on the amount of coating.

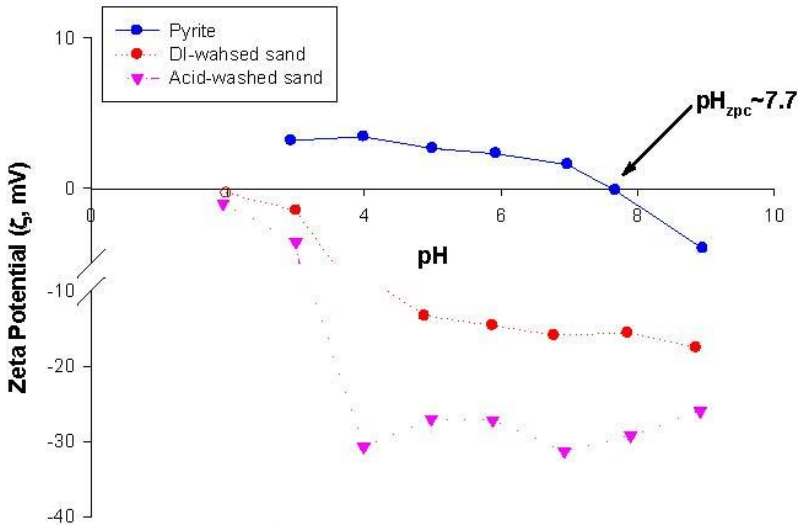

Figure 4.1 Zeta potentials of distilled water (DI)-washed sand, acid (6N-acid)washed sand and pyrite.[84]

Table 4.2 Amount of pyrite coated on sands at different pH.

pH	Description	Pyrite concentration on sand (mg/g)	pH after coating
pH 4.13	No rinsing	0.80	4.56
	24-hour rinsing	0.85	4.55
pH 7.26	No rinsing	0.88	5.28
	24-hour rinsing	0.88	5.32

The coated sands were also analyzed with SEM/EDS and the results are shown in Figure 4.2. The surfaces of coated sand from different coating conditions were very similar. A patchwise surface coating was observed from Figure 4.2, where pyrite particles aggregated at indentations on the surface rather than on smooth surfaces.

Similar observations were found with FeS-coated sand and iron-oxide coatings on silica.[50, 51]

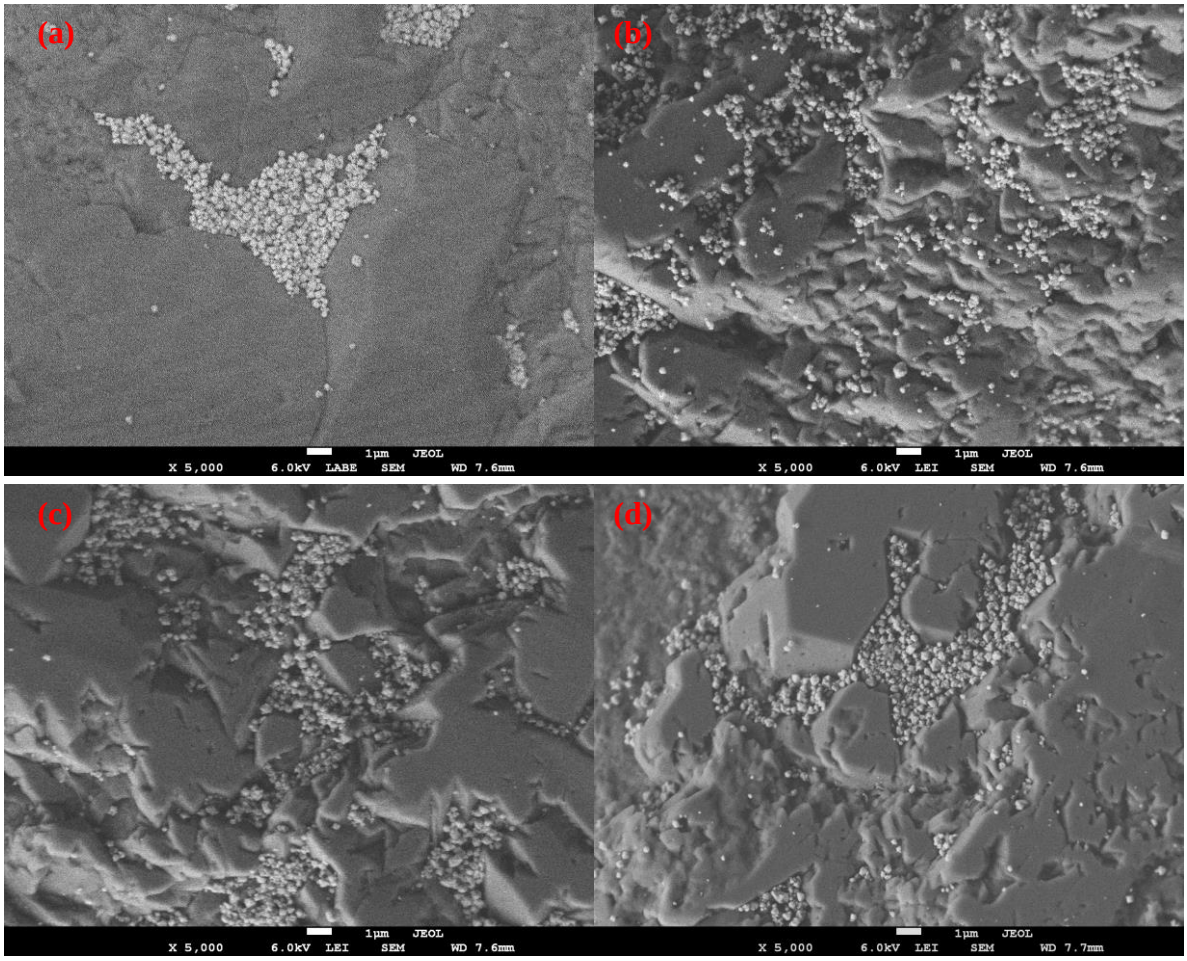

Figure 4.2 SEM/EDS micrographs of pyrite coated chemically-treated sand at different pH values. (a): pH 4, no rinsing; (b): pH 4, 24-hour rinsing; (c): pH 7, no rinsing; (d): pH 7, 24-hour rinsing.

4.3.2 Effect of Pyrite to Sand (P/S) Ratio on Electrostatic Attraction Coating

Different ratios of pyrite to sand (2 mg/g, 1 mg/g, and 0.5 mg/g) were also considered to investigate the coating efficiency. The coating and extraction procedures were similar to those described in Section 4.2.2.1 and 4.2.2.2. However, they differ in that before coating, the pH was adjusted to 7, and the coated sands were not rinsed with DI water after coating. The results are shown in Table 4.3. The amount of pyrite coated on sand was found to increase when greater masses of pyrite were added.

Table 4.3 Amount of pyrite coated on sands with different P/S ratio.

P/S Ratio (mg/g)	Pyrite concentration on sand (mg/g)	pH after coating
2	1.74	5.26
1	0.78	4.81
0.5	0.29	4.41

Therefore, the procedure chose was to use chemically-treated sand, adjusted to pH 7 with a P/S ratio of 1 mg/g, and no rinsing. The average amount of pyrite on attached to sand using this procedure was found to be 0.82 mg FeS_2/g sand.

4.3.3 Comparison of Three Coating Methods

Pyrite synthesis on the sand surface yielded a coating of 1.37 mg FeS_2/g sand, which was higher than that with the electrostatic attraction coating method (0.82 mg/g).

However, the initial P/S ratio for this method was much higher than that for electrostatic attraction coating. P/S ratio was estimated to be 8 mg/g, since 15 mL 0.1 mol/L $FeCl_3$ and 15 mL 0.2 mol/L NaSH mixture would generate about 0.08 g pyrite and 10 g sand was added into the mixture for microwave irradiation. Therefore, the efficiency of "pyrite formed on sand" method was much lower than the electrostatic attraction coating and any further development of this method was abandoned.

Polymer-based coating generated a coating amount of 0.36 mg FeS_2/g sand when the initial P/S ratio was 1 mg/g. The concentration was less than half of the pyrite concentration on sand achieved by the electrostatic attraction method (0.82 mg/g). But the polymer may have an effect on removal of Hg(II), so polymer/pyrite-coated sand was also used in column tests, as discussed in Section 4.3.8 and 4.3.9.

4.3.4 Stability Test with Pyrite-Coated Sand

Stability of pyrite attached to sand was evaluated in column experiments by measuring the concentration of Fe in the effluent using a feed solution of deoxygenated DI water at three influent pH values (5, 7, and 9). The effluent Fe concentrations measured over a period of 3 hours are shown in Figure 4.3. Each sample was collected for a time interval of 10 minutes; therefore, the concentrations presented are 10-minute averages. As shown in Figure 4.3, pyrite was partially dissolved from the sand surface at all tested influent pH and times. The lowest amount of pyrite was dissolved when the feed flow was adjusted to pH 7, while feed at pH 5 released the greatest amount of pyrite. However, the loss of Fe to the solution decreased at pH 5 and pH 9 as time

increased. At neutral pH, the loss of Fe from the sand surface was nearly constant around 1.45-1.68 mg/L over the sampling time. Although some pyrite dissolved at all pH, the amount of pyrite lost is relatively small compared to the total amount of pyrite attached to the sand. The iron released during the entire experiment represents 3.2%, 2.4%, and 3.1% of the pyrite present in tests at influent pH 5, 7, and 9, respectively. If the pyrite loss rate remains constant, it would take more than 4 days to consume all of the pyrite on sand surface. However, the loss of pyrite decreases with time at pH 5 and 9, so a longer time would be required to consume all of the pyrite.

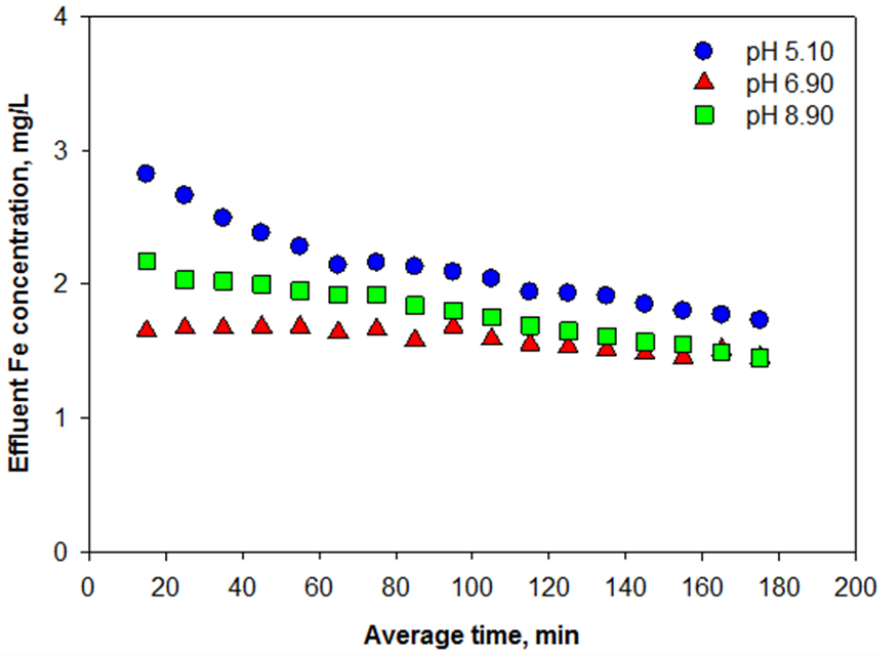

Figure 4.3 Column test of solubility of pyrite-coated sand at pH 5.10, 6.98, and 8.90. The flow rate was 1.03 mL/min.

4.3.5 Tracer Test

Tracer tests with chemically-treated sand, with and without pyrite were conducted to characterize the RACS media. Non-reactive KBr was selected as the tracer. The parameters for tracer tests are listed in Table 4.4. After packing the sand into the column, the column was purged with carbon dioxide for 15 min and then saturated with DI water.

Table 4.4 Parameters for tracer test.

Media	Porosity	Flow rate (mL/min)	HRT (= V_{H2O} / Q) (min)
Chemically-treated sand	0.44	1.08	14.8
Pyrite coated chemically-treated sand	0.46	1.02	15.1

Figures 4.4 and 4.5 show the 3-minute averaged, effluent bromide concentrations over the time. The shapes for both cases were similar and none of them represent an ideal plug flow. The mean residence times calculated from experiment data with Equation 4.1 were 17.0 min and 15.6 min for tests with and without pyrite, respectively. For both cases, the hydraulic retention time (HRT) and the mean residence time are very close. The hydraulic retention times for both cases are a little smaller than the mean residence times. It could be the errors from the measurement of total volume, weight of water in pores, and flow rate.

$$\bar{t} = \frac{\sum t_i c_i \Delta t}{\sum c_i \, \Delta t} \tag{4.1}$$

where t_i is the sampling time (min); c_i is the effluent concentration at time t_i (mg/L); and Δt is the time interval (min).

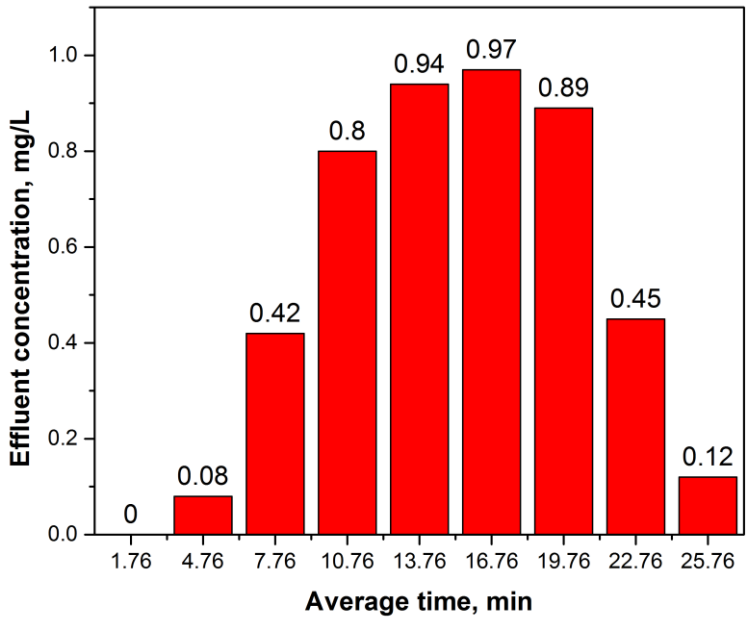

Figure 4.4 Tracer test with chemically-treated sand.

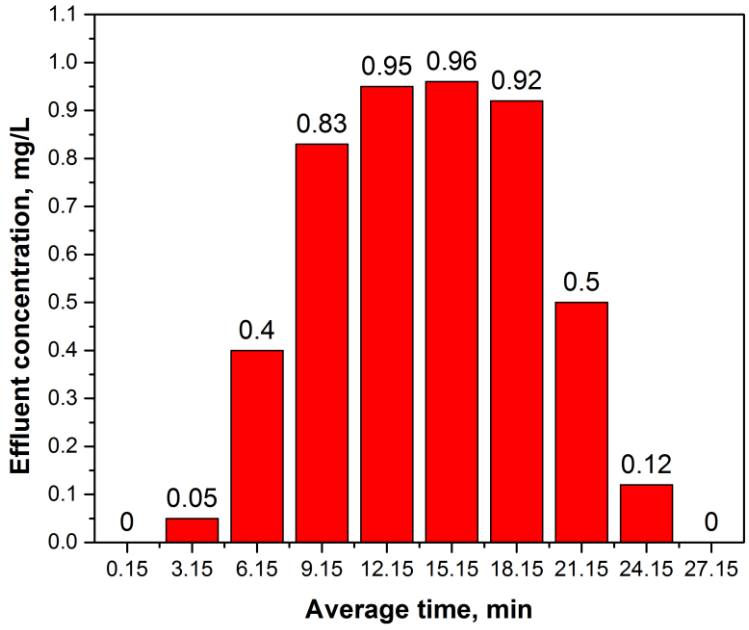

Figure 4.5 Tracer test with pyrite-coated chemically-treated sand.

4.3.6 Column-Based Hg(II) Removal by Electrostatic Attraction/Pyrite-Coated Sand

4.3.6.1 Effect of Influent pH

Mercury sorption column experiments at different influent pH values were conducted to study the capability of RACS system to removal mercury from water. Effluent samples were again collected for a time interval of 10 min. The column experiment at influent pH of 5.03 with a flow rate of 1.06 mL/min is named "Test A", the experiment at influent pH of 6.93 with a flow rate of 1.08 mL/min is named "Test B", and experiment at influent pH of 8.94 with a flow rate of 1.08 mL/min is named "Test C". The breakthrough curves for Hg(II) from the columns with pyrite-coated sand

(P/S ratio 0.82 mg/g) are shown in Figure 4.6 (a). The breakthrough for Tests A and B began between 745 min and 795 min, while the breakthrough for Test C started around 996 min. Both Tests A and B showed nearly complete breakthrough during the sampling period. However, Test C did not fully breakthrough, which means that it did not reach its maximum removal capacity. As the influent pH decreased (C>B>A), the breakthrough curves were shifted to the left, indicating lower capacity for mercury removal. Also, the steepness of the breakthrough curves increases as influent pH decreases, which indicates faster removal kinetics. The total amounts of mercury that were removed were calculated by numerically integrating the mass flow of contaminant removed ($Q*(C_0-C)$) over the operating time of the column. The amounts removed for Tests A, B, and C were 0.071, 0.082, and 0.11 mg/mL based on the total volume of the system, respectively. These were equivalent to pyrite loadings of 0.050, 0.057, and 0.075 g Hg/g FeS_2, respectively, which were much lower than the maximum Hg uptake on pyrite (0.18 g Hg/g FeS_2) observed in batch system in Chapter III. But they are consistent with results reported by Bower et al.[37], who concluded that the adsorption rate and removal capacity of mercury increased as pH increased. At acidic pH, the pyritic site (≡S-H) is the dominant functional group on the surface of pyrite. In the presence of mercury, it forms surface complexes, such as ≡S-Hg-Cl and ≡S-Hg-OH.[37, 40] However, the oxyhydroxide site (≡O-H) is the major functional group on the pyrite surface at basic pH and produces more complex aqueous chemistry.[37, 40, 44] The surface of pyrite is oxidized and covered by a layer of Fe (III) oxyhydroxide that may present more adsorption sites for mercury.[44] Selected samples were passed through a 0.02-μm filter before measuring the Hg

concentration. The concentrations of the filtered samples were slightly lower than the concentrations of the unfiltered samples for experiments at influent pH 5 and 9. However, the differences between unfiltered and filtered samples for Test B were much larger than the other two tests. The differences between measurements in filtered and unfiltered samples are likely due to two possibilities. One is that substantial amounts of Hg in the effluent can exist in solid phases that are removed by filtration. The other possibility is that filter itself adsorbs soluble Hg species such as Hg-sulfide or Hg-polysulfide complexes.

The pH of each selected samples was recorded and shown in Figure 4.6 (b). The effluent pH for Test A increased slowly over time and retained a value near that of the influent (pH 5.03). However, the effluent pH for Test B and C increased when breakthrough started. Previous research (Chapter III) on synthesized pyrite and Hg(II) showed that the release of protons from the pyrite surface without contact with mercury would continue for about 50 min (Figure A.2). The first sample in column test was taken after operation for 80-90 min (Figure 4.6 (a)), so most of the protons released from pyrite surface by reactions that do not involve mercury would be flushed out from the column before the first sample was taken. Therefore, the effect on effluent pH from pyrite itself should occur early in the column test but before first sample. However, adsorption of Hg(II) occurred at all times before complete breakthrough and could affect the pH. If the column were an ideal plug flow system and if Hg adsorption were very rapid, pyrite would be in equilibrium with influent Hg in the zone nearest the bottom of the column. If there were multiple sites on the pyrite that could adsorb mercury, they all

could equilibrate. Therefore, the effluent pH is likely due to the combined effects of reactions at sites that both strongly and weakly adsorb mercury. In an equilibrium column, the breakthrough of mercury would be sharp, so the change in effluent pH would also be sharp. However, the real column is not an ideal plug flow and is not at equilibrium, so the pH changes would be more gradual. Therefore, the pH behavior in Test B and C could be due to a net effect of both pyritic and hydroxide sites reacting with Hg at same time. The effluent pH in Test A did not rise as much because it was not much below the influent pH (5.03).

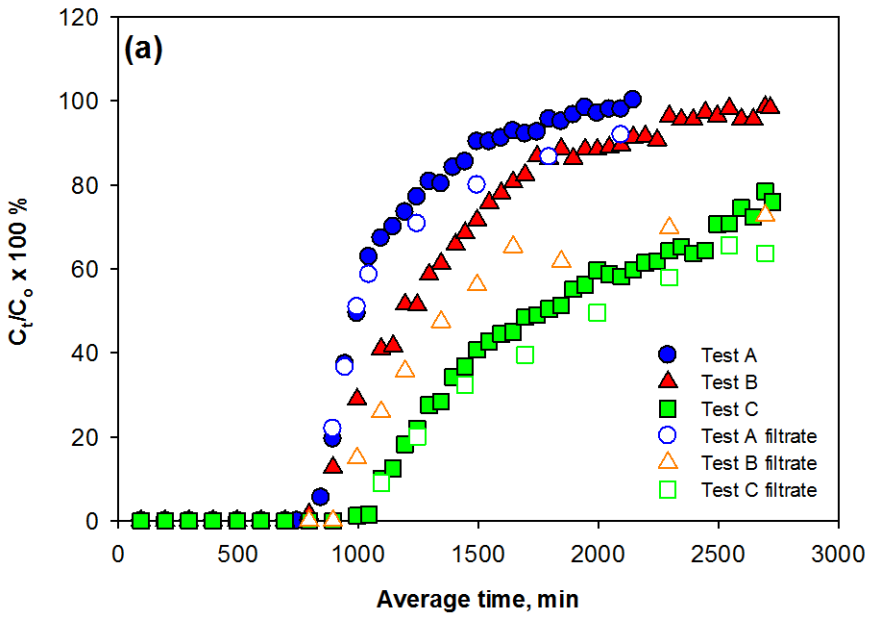

Figure 4.6 Effluent Hg(II) concentration through columns with pyrite-coated sand at different influent pH values. Test A: influent pH = 5.03, flow rate Q = 1.06 mL/min; Test B: influent pH = 6.93, flow rate Q = 1.08 mL/min; Test C: influent pH = 8.94, flow rate Q = 1.08 mL/min. (a) Concentration vs time; (b) pH vs time.

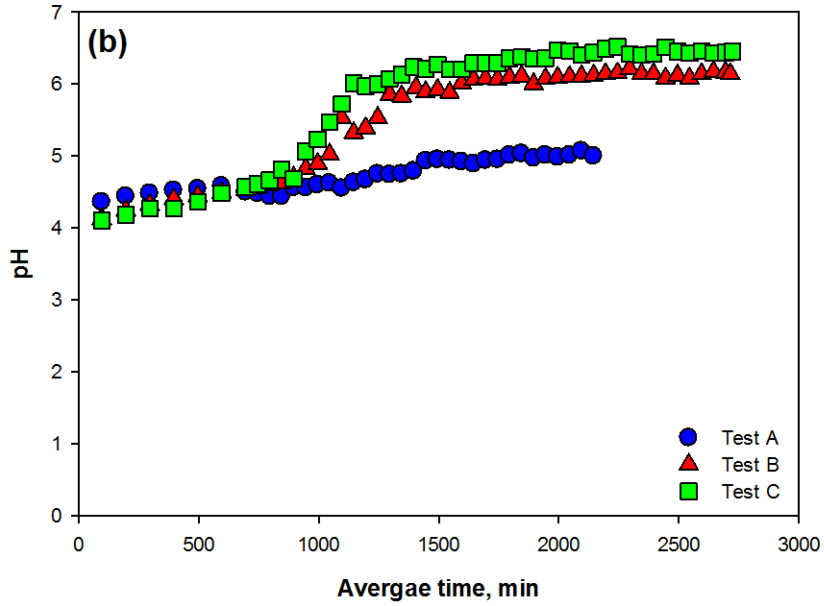

Figure 4.6 Continued.

4.3.6.2 Effect of Hydraulic Retention Time

A column test at influent pH 7 (Test D) was conducted with lower HRT by applying a flow rate of 2.14 mL/min, which was almost twice the value used in the other column tests. Samples were collected over a time interval of 6 min and the results are shown in Figure 4.7 (a). The breakthrough curve was shifted to the left when the HRT was reduced, as was expected for a column. If an adsorption column operates at equilibrium with a favorable isotherm, the time to breakthrough is proportional to the HRT.[85] If the column is not at equilibrium, the relationship is typically linear, so nearly proportional behavior that would be observed in the intercept is small. The observed breakthrough time for test D was 357 min, which is approximately half of that for Test B

(695 min). However, the steeper shape of the breakthrough curve at the lower HRT indicates faster kinetics. This behavior is consistent with external film transfer limiting removal kinetics, which would be faster at higher fluid velocities. There were 0.075 mg/mL of mercury removed at the lower HRT (test D), which is a little less than that observed (0.082 mg/mL) in the higher HRT system (test B). Hg in effluent was mostly present in solution, because the concentrations before and after filtration were close. The pH of the effluent increased as the breakthrough started at both HRT, as shown in Figure 4.7 (b).

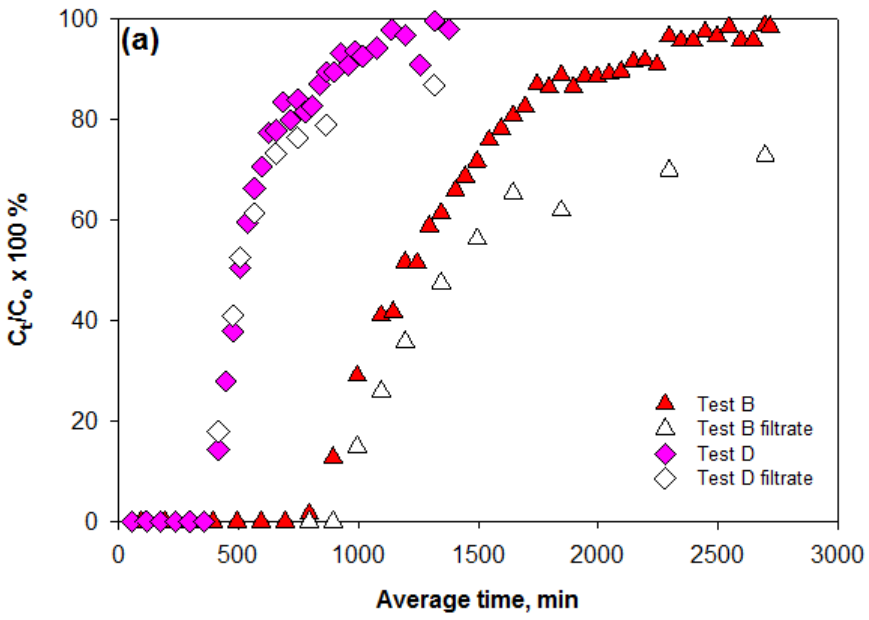

Figure 4.7 Effluent Hg(II) concentration through columns with pyrite-coated sand with low HRT. Test B: influent pH = 6.93, flow rate Q = 1.08 mL/min; Test D: influent pH = 7.01, flow rate Q = 2.14 mL/min. (a) Concentration vs time; (b) pH vs time.

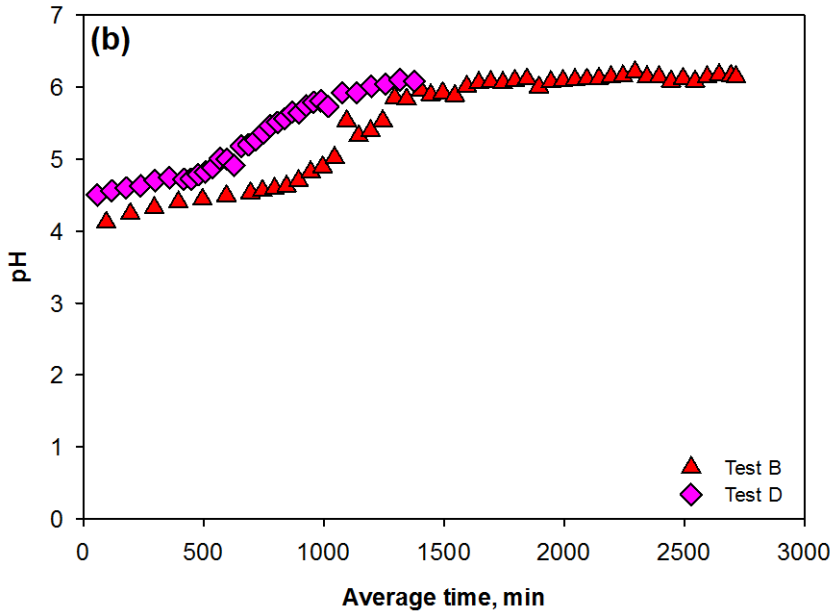

Figure 4.7 Continued.

4.3.6.3 Effect of Salts

The effect of salts (Test E) on mercury removal was investigated by adding 0.01 M sodium sulfate and 0.01 mol/L sodium nitrate to the influent. Samples were collected for a time interval of 10 min and the results are shown in Figure 4.8. Breakthrough in experiments with salts started about 100 min later than without salts, but the midpoint of the breakthrough curve was nearly the same for both experiments and both systems ultimately achieved the same removals (98%-102%). The breakthrough curve for the experiment with salts was narrower, indicating that the presence of salts increased the rate of mercury removal. The total amount of mercury removed was around 0.073

mg/mL for Test E (high salt) compared to 0.082 mg/mL for Test B (low salt). The background salts may have affected the types of surface complexes formed by adsorption of Hg(II). The presence of salts may also desorb some Hg that was sorbed onto hydroxide sites since ≡O-H groups may not adsorb as strongly as ≡S-H groups.[40]

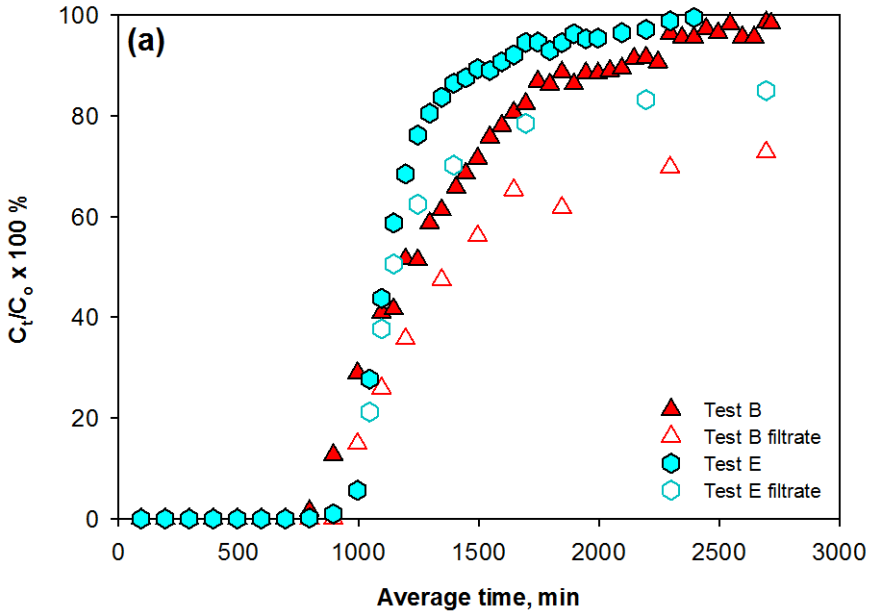

Figure 4.8 Effluent Hg(II) concentration through columns with pyrite-coated sand with and without salts. Test B: influent pH = 6.93, flow rate Q = 1.08 mL/min; Test E: influent pH = 6.99, flow rate Q = 1.03 mL/min, influent concentration of $NaNO_3$ and Na_2SO_4 = 0.01 mol/L. (a) Concentration vs time; (b) pH vs time.

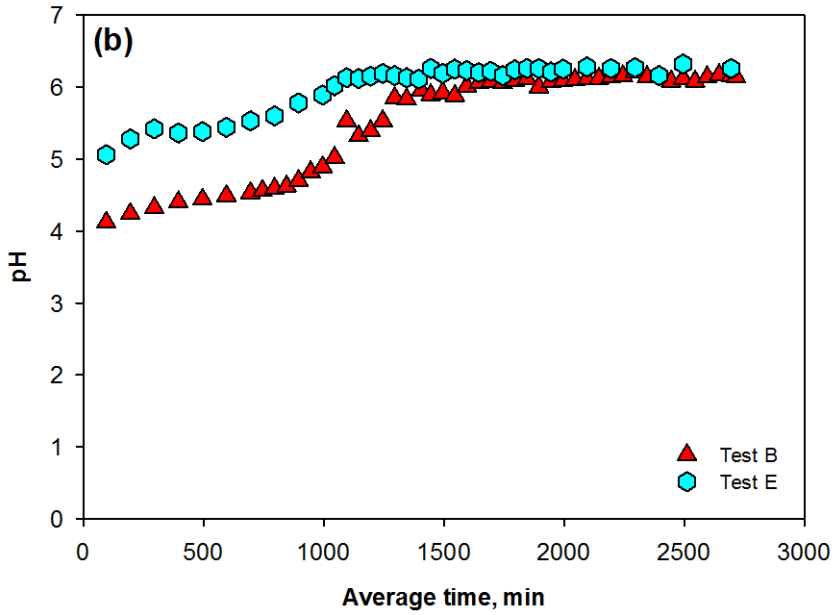

Figure 4.8 Continued.

4.3.6.4 Effect of Humic Acids

The effect of humic acids (HAs) on mercury removal at pH 5 was studied by adding 10 mg/L (Test F) and 20 mg/L HAs (Test G) into the feed solution. Samples were collected for a time interval of 10 min and the results are shown in Figure 4.9 (a). The tests with HAs started to breakthrough at the very beginning and none of them reached full breakthrough during the sampling period. The maximum observed C/C_0 was around 87% for 10 mg/L HAs test, and 68%-70% for 20 mg/L HAs test. The flatter breakthrough curves for experiments with HAs indicate that it slowed removal of Hg(II). Despite the slower removal kinetics, columns with HAs showed higher capacities for

Hg(II) removal. There was 0.081 mg/mL of mercury removed in Test F (10 mg/L HAs) and 0.093 mg/mL in Test G (20 mg/L HAs) compared to 0.070 mg/mL in tests without HAs at the same influent pH (Test A). Organic matter like HAs may contain reduced sulfur groups that could complex with HAs by forming Hg-HAs complexes. Xia et al.[86] pointed out that Hg(II) binding to soil humic acids was dominated by complexation with reduced sulfur functional groups (thiol (R-SH) and disulfide (R-SS-R)/disulfane (R-SSH)). Other functional groups, such as H-bonded O-H groups and C=O groups, also showed capability for forming complexes with Hg(II),[87] but Hg(II) prefers reduced sulfur groups over other functional groups in humic acids.[86] However, HAs can bind Hg(II) at more than one site. The preference of Hg for sulfur means that it is likely to bond first with those groups. However, the limited density of reduced sulfur ligands in HAs means that Hg is likely to also bond with a nearby oxygen group.[86] The mercury concentration in filtered samples was much lower than in samples without filtration, especially for the experiment with 20 mg/L HAs (Test G). This indicates that mercury in the effluent could be in a suspended solid phase or it could be soluble, but adsorbed by the filter. As the HAs concentration increased, less mercury was found in the filtrate of the effluent. This may due to the reaction between Hg(II) and soluble HAs, which may produce mercury containing solid phases or large complexes that can be screened by the 0.02-μm filter. On the other hand, Hg-HAs complexes might be more likely to be absorbed by the filter and removed from solution in that way. The pH (Figure 4.9 (b)) for each test followed a similar trend, which was nearly constant over the sampling period.

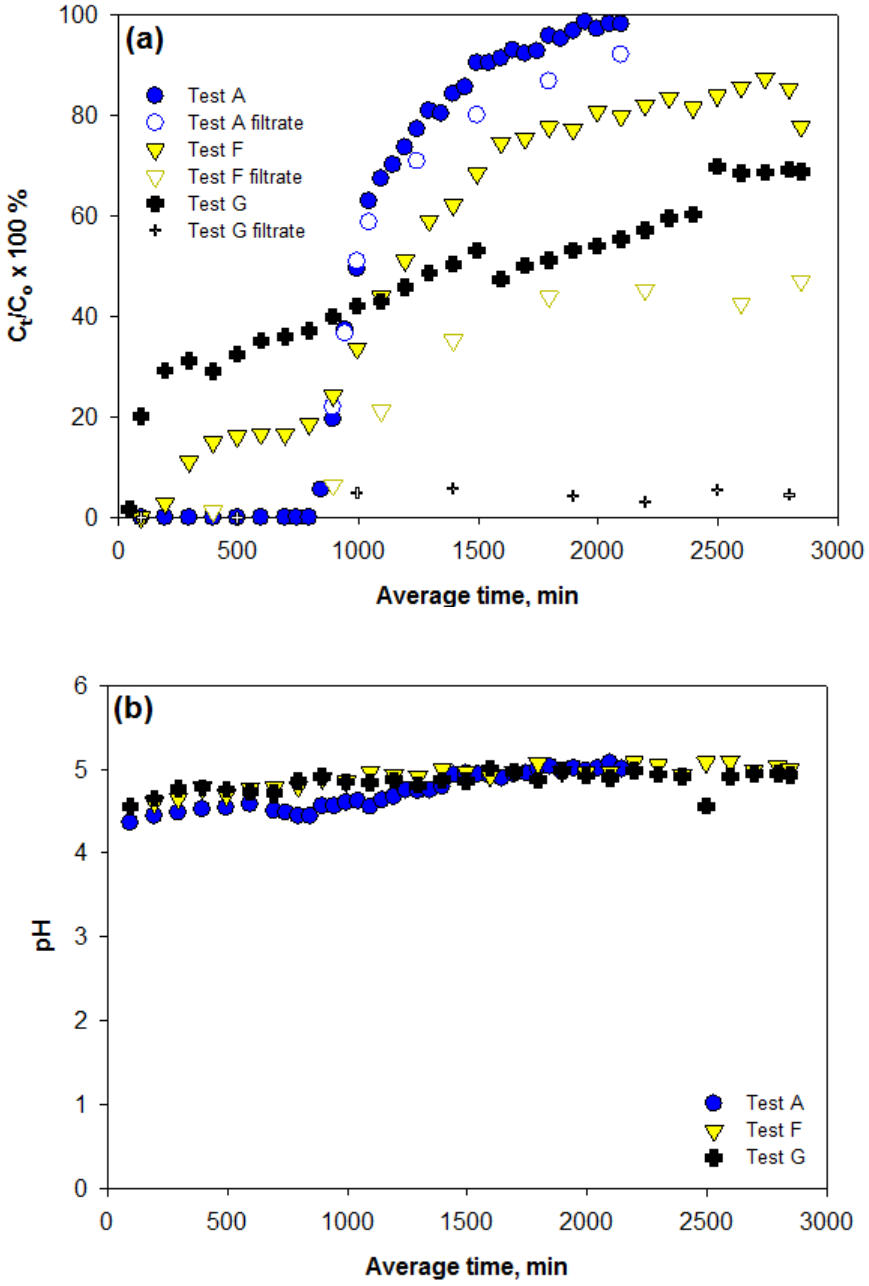

Figure 4.9 Effluent Hg(II) concentration through columns with pyrite-coated sand with 10 and 20 mg/L HAs. Test A: influent pH = 5.03, flow rate Q = 1.06 mL/min; Test F: influent pH = 5.05, flow rate Q = 1.00 mL/min, influent concentration of HAs = 10 mg/L; Test G: influent pH = 5.01, flow rate Q = 1.01 mL/min, influent concentration of HAs = 20 mg/L. (a) Concentration vs time; (b) pH vs time.

4.3.7 Microscopic and Spectroscopic Characterization of Electrostatic Attraction/Pyrite-Coated Sand

After the column tests, the pyrite-coated sand was dried inside the chamber prior to SEM/EDS and XPS analysis. The SEM/EDS results are shown in Figure 4.10. The morphology of the surface was similar to the sand before it contacted mercury in the columns. There were some powder-like materials found on the surface, but they have not been identified. One possibility is that they are HgS precipitates that formed on the surface. EDS spectra shows strong silica and oxygen peaks and minor iron and sulfur peaks, due to the low concentration ratio of pyrite to sand. Mercury peaks were not detected for any samples, because the concentration of mercury was too low compared to the other elements.

Figure 4.11 show the results for broad XPS scans and they indicate that the surface consisted of iron, oxygen, sulfur, carbon, silica, and mercury. None of the samples showed Hg 4f peaks, because Hg 4f7/2 peaks (99 eV – 102 eV) were so close to the Si 2p peaks (98 eV – 104 eV) and the Si 2p peak is so strong that it overlaps the Hg 4f peaks. Since there was much more sand present than other compounds, the Fe, S, and Hg peaks were very weak and some of them were so weak that they could not be observed in the narrow scans.

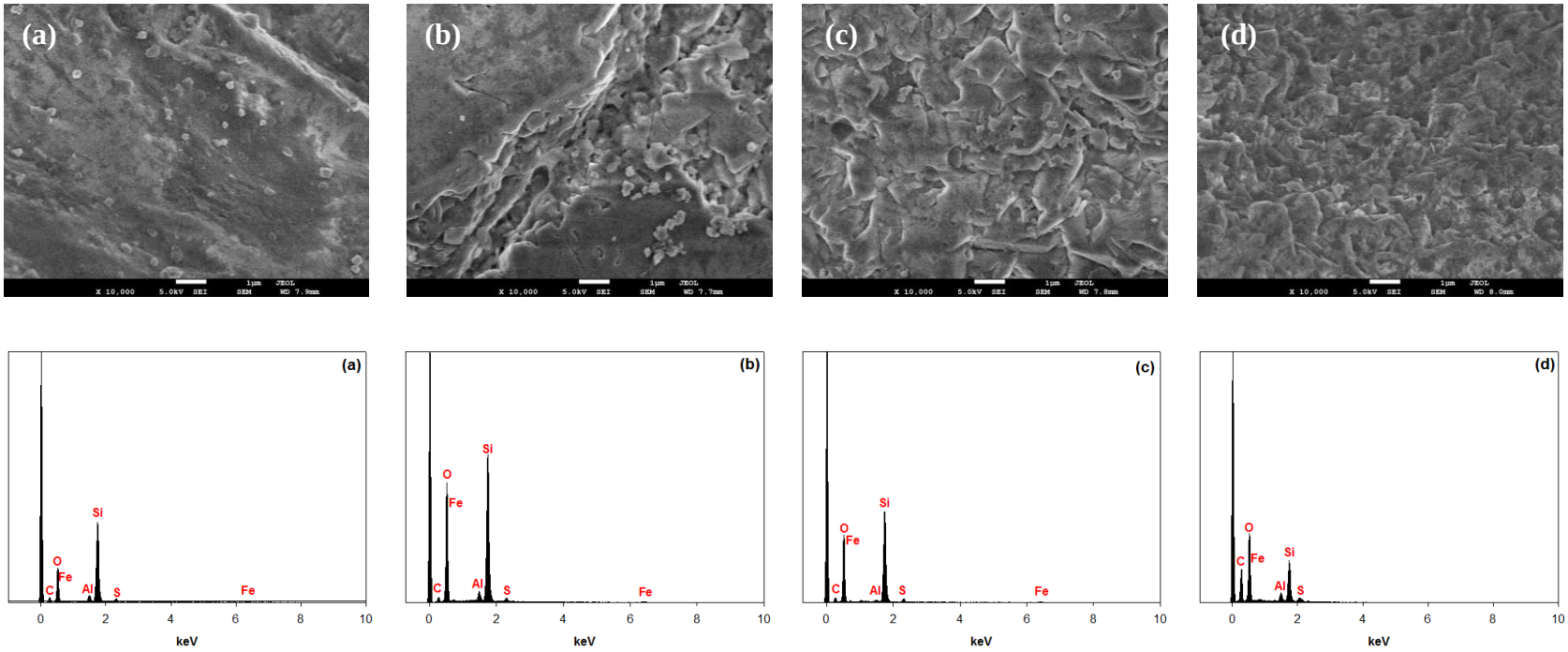

Figure 4.10 SEM images and EDS results of pyrite-coated sand after flow with 1 mg/L Hg(II) (a) at influent pH 5 (Test A); (b) with low HRT at influent pH 7 (Test D); (c) with 0.01 M salts at influent pH 7 (Test E); (d) with 10 mg/L HAs at influent pH 5 (Test F).

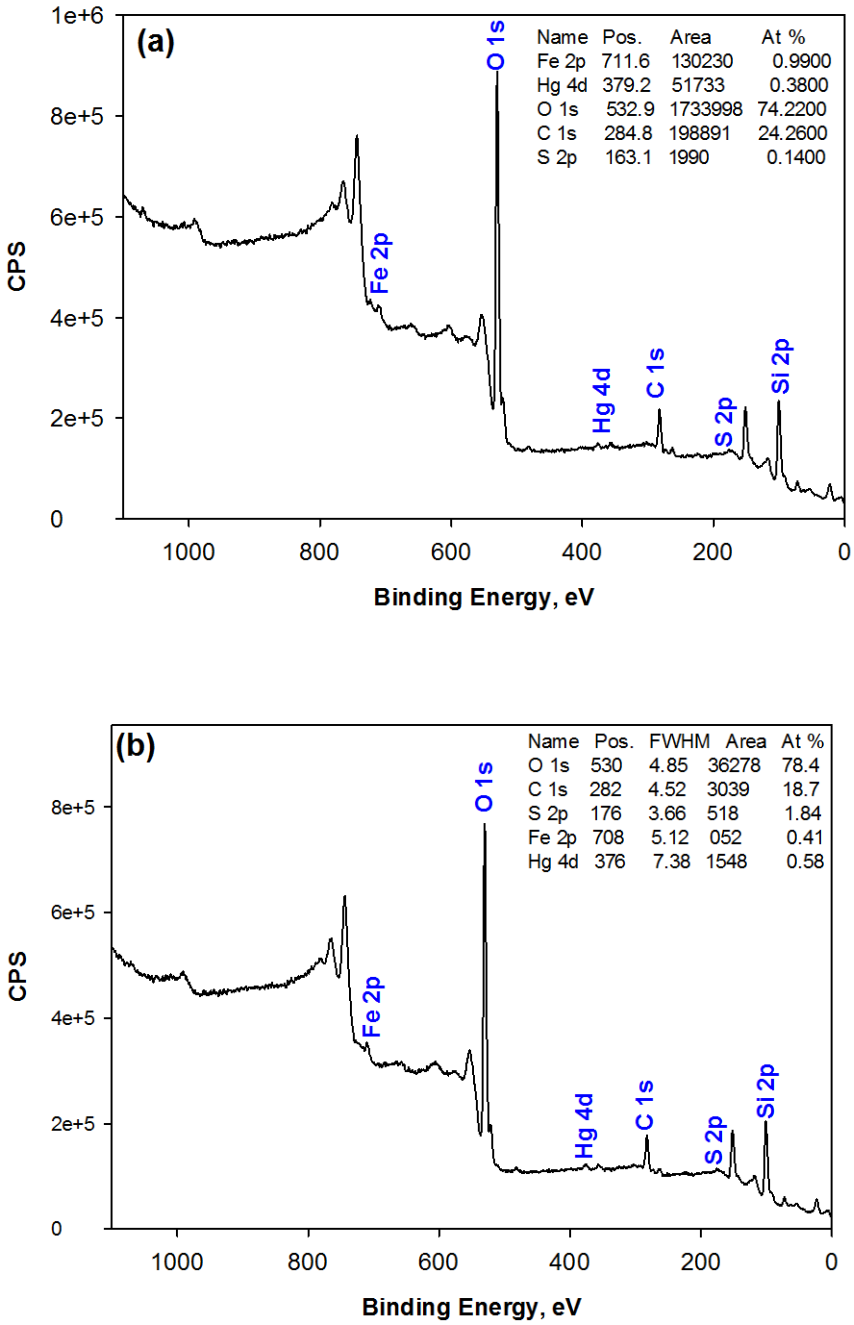

Figure 4.11 Broad scan for pyrite-coated sand after flow with 1 mg/L Hg (a) at influent pH 5 (Test A); (b) with 0.01 M salts at influent pH 7 (Test E).

To confirm the surface species, some narrow scans of Fe 2p, S 2p, and Hg 4d spectra were also analyzed and the results are shown in Figures 4.12 and 4.13. The binding energy around 711.9 eV is the peak of Fe 2p3/2 which indicates the characteristic peaks of Fe(III) or FeS. The peak of S 2p3/2 was too weak to analyze in both samples, but it was located near 163eV, which indicates that the species was sulfide. Hg 4d peaks were identified for the samples; however, the information for Hg 4d peaks is limited and the species cannot be specified. Based on previous analyses of pyrite contacted with Hg(II) in batch tests in Chapter III, these peaks should be associated with HgS.

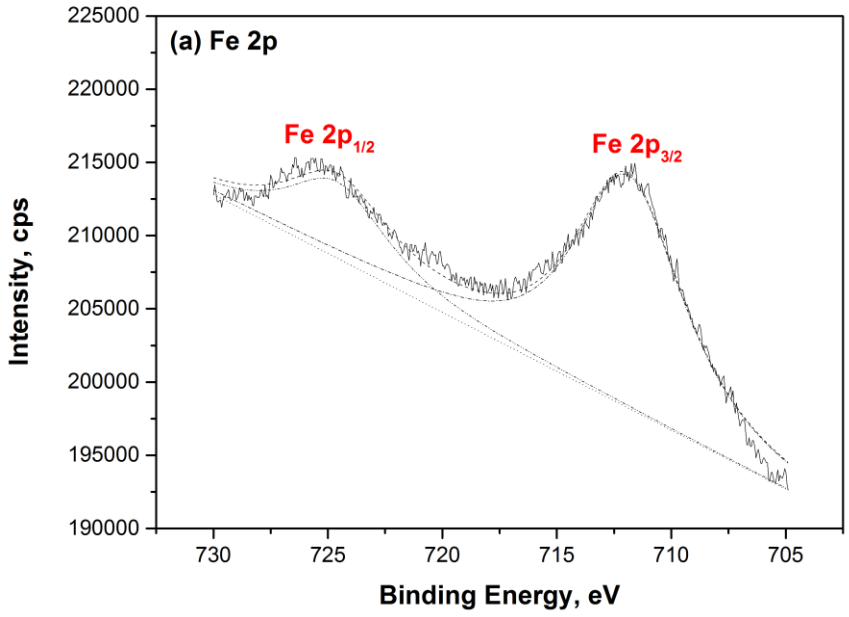

Figure 4.12 Narrow scans for pyrite-coated sand after flow with 1 mg/L Hg at influent pH 5 (Test A). (a) Fe 2p spectra; (b) S 2p spectra; (c) Hg 4d spectra.

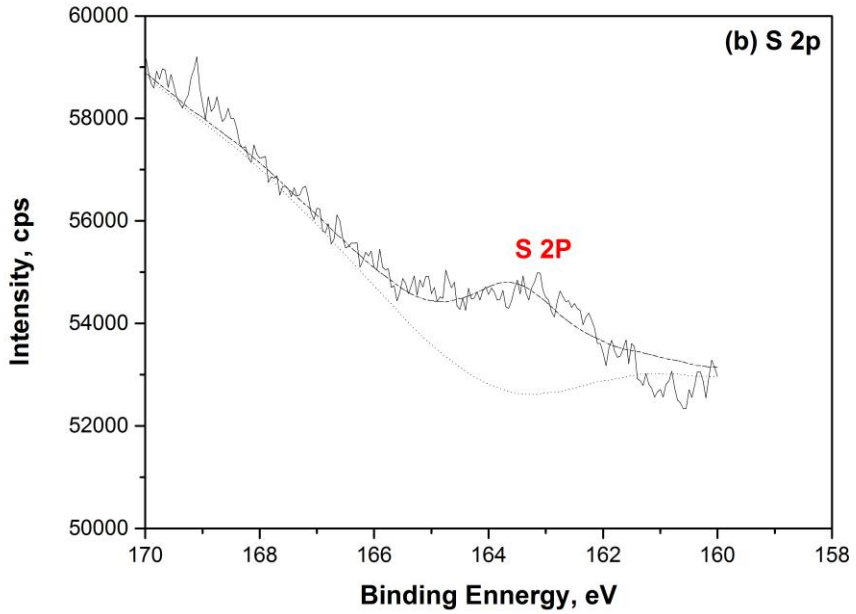

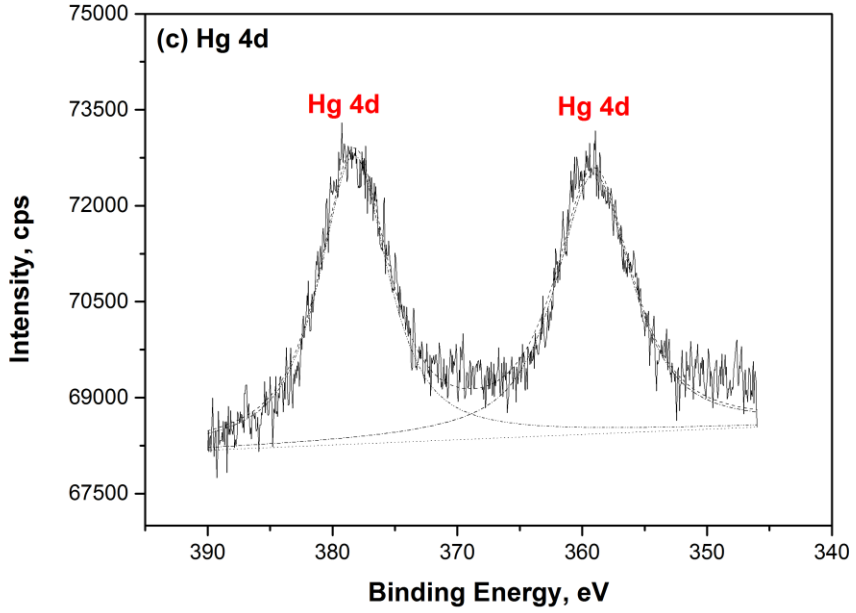

Figure 4.12 Continued.

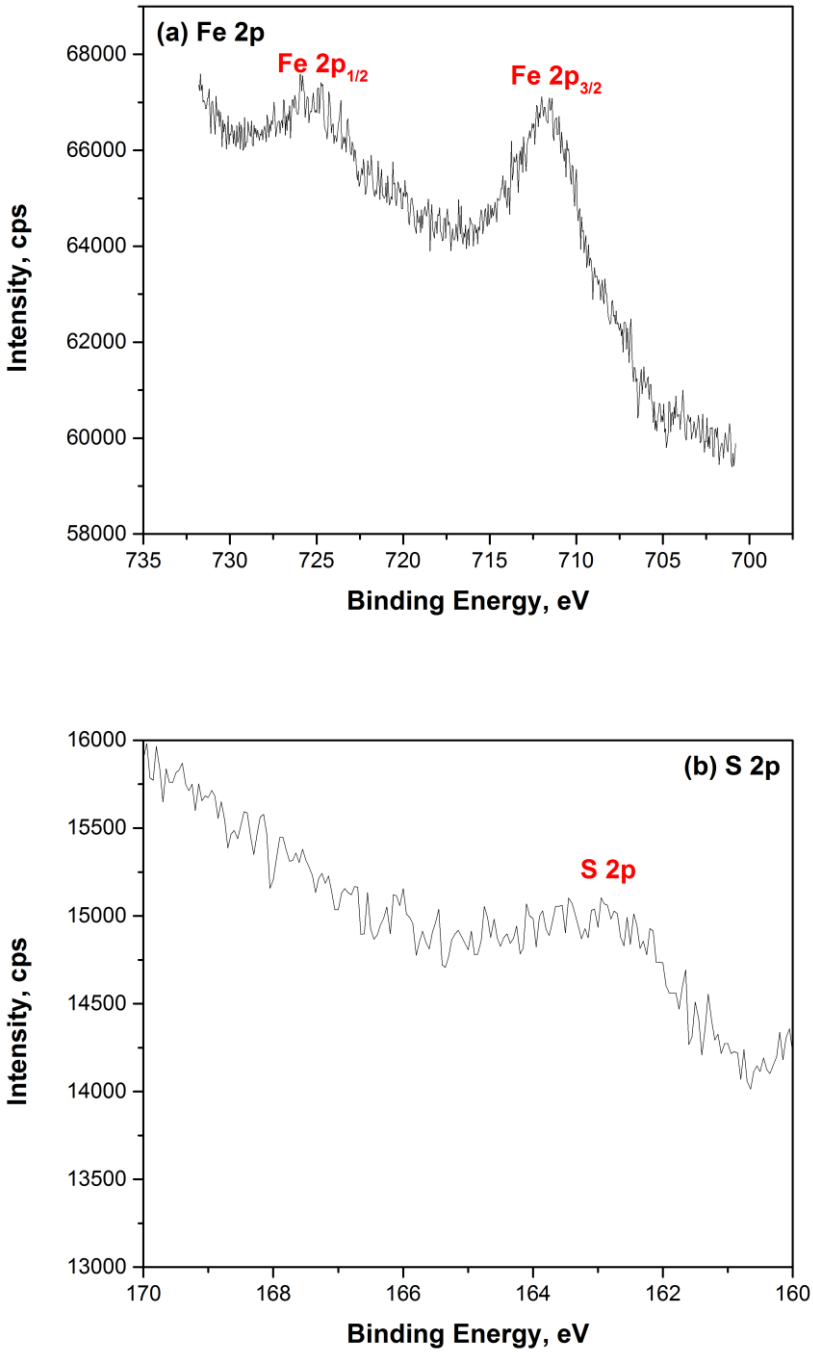

Figure 4.13 Narrow scans for pyrite-coated sand after flow with 1 mg/L Hg with 0.01 M salts at influent pH 7 (Test E). (a) Fe 2p spectra; (b) S 2p spectra; (c) Hg 4d spectra.

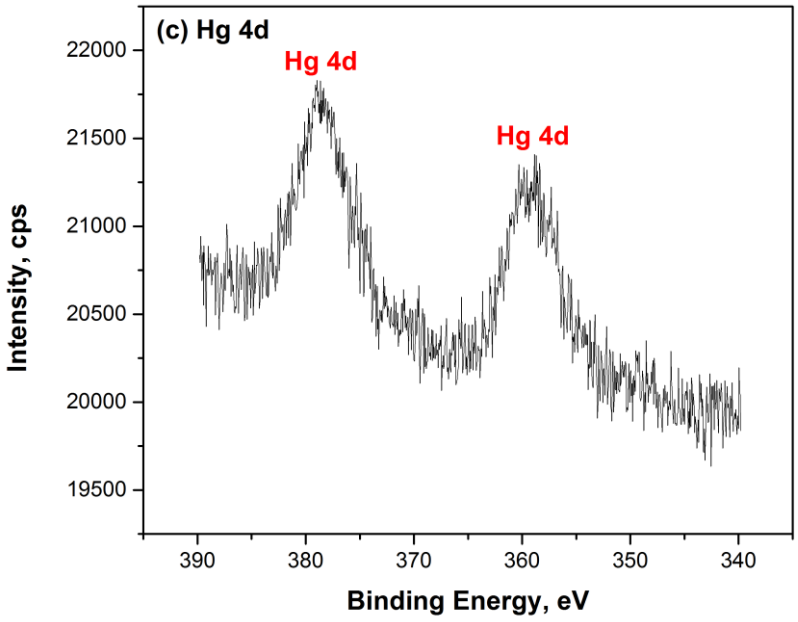

Figure 4.13 Continued.

4.3.8 Column-Based Hg(II) Removal by Polymer/Pyrite-Coated Sand

Mercury sorption column experiments at pH 7 were conducted to study the capability of polymer/pyrite-coated sand to removal mercury from water. Similarly, the sample was collected for a time interval of 10 min. The flow rates were around 1.00-1.07 mL/min and the porosities were 0.43-0.46 for the tests. The column experiment at influent pH of 6.97 with a flow rate of 1.07 mL/min is named "Test H", the experiment with 0.01 mol/L salts at influent pH of 6.93 with a flow rate of 1.00 mL/min is named "Test I", and experiment with 10 mg/L HAs at influent pH of 7.03 with a flow rate of 1.01 mL/min is named "Test J". The breakthrough curves for Hg(II) from the columns

with polymer/pyrite-coated sand (P/S ratio 0.36 mg/g) are shown in Figure 4.14. The breakthrough for Tests H and I started at 1495 min, which was much longer than just pyrite-coated sand. Neither system achieved complete breakthrough during the sampling period, which means that they did not reach their maximum removal capacity. The maximum observed C/C_0 was around 85% for tests with and without salts. There were 0.14 mg/mL and 0.13 mg/mL of mercury removed in the absence and presence of salts, respectively, compared to 0.082 mg/mL and 0.073 mg/mL in tests with electrostatic attraction/pyrite-coated sand at the same influent pH (Test B and E). One possibility to explain the higher removal is that the polymers also could remove mercury, so that the breakthrough started later. Polymers, such as PAA and polyethylenimine, have been demonstrated to be able to complex with metal ions by forming macromolecular complex.[88-91] PAA is rich in carboxylic functional groups, which are effective binding sites for Hg(II).[91] The breakthrough curve for the experiment with salts (Test I) was steeper than without salts (Test H) at the beginning, which indicates the presence of salts increased the rate of mercury removal. The concentrations of the filtered samples were very close to the concentrations of the unfiltered samples for experiments without salts, which indicates that most Hg in the effluent was in soluble phases or less likely to be adsorbed by the filter. While in the presence of salts, the differences between the unfiltered samples and filtered samples were larger than without salts. This indicated that the presence of salts promoted formation of Hg-containing solids or increased the Hg affinity to the filter.

The effect of humic acids (HAs) on mercury removal at pH 7 was studied by adding 10 mg/L HAs into the feed solution. Samples were collected for a time interval of 10 min and the results are shown in Figure 4.14 in green. The tests with HAs started to breakthrough at the very beginning and did not reach full breakthrough during the sampling period. The maximum observed C/C_0 was around 72%. The total amount of mercury removed was around 0.087 mg/mL for Test J compared to 0.14 mg/mL in Test H. The mercury concentration in filtered samples was much lower than in samples without filtration. This indicates that most mercury in the effluent was in a solid phase or was adsorbed by the filter. The reason for this could be the complexation of Hg(II) with soluble HAs, which may produce mercury containing solid phases, large Hg-HAs complexes, or more adsorbable complexes.

The pH of each selected samples was recorded and shown in Figure 4.14. The effluent pH for each test slowly increased with time but was still lower than the influent pH. Hg(II) removal process was not only an adsorption process but also involved chemical reactions and those reactions could produce or consume H^+. Therefore, the effluent pH is probably results of both sites reacting with Hg at same time.

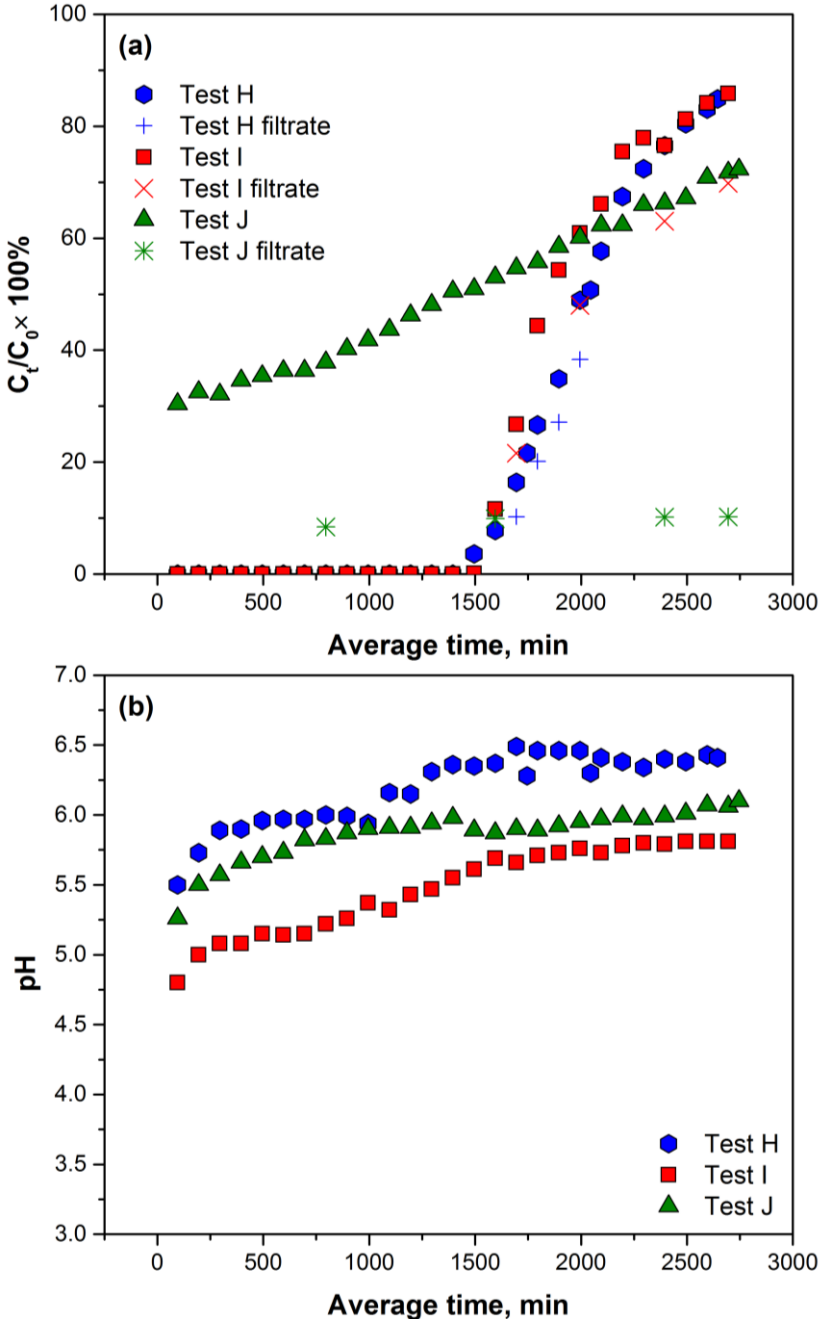

Figure 4.14 Effluent Hg(II) concentration through columns with polymer/pyrite-coated sand with and without sand and HAs at pH 7. Test H: influent pH = 6.91, flow rate Q = 1.07 mL/min; Test I: influent pH = 6.93, flow rate Q = 1.00 mL/min, influent concentration of $NaNO_3$ and Na_2SO_4 = 0.01 mol/L; Test J: influent pH = 7.03, flow rate Q = 1.01 mL/min, influent concentration of HAs = 10 mg/L. (a) Concentration vs average time; (b) pH vs average time.

4.3.9 Microscopic and Spectroscopic Characterization of Polymer/Pyrite-Coated Sand

The SEM figures are shown in Figures 4.15-4.17. The morphology of the surface was similar to the sand before it contacted mercury in the columns. But compared to sand prepared with electrostatic attraction coating, pyrite was more spread about the surface of the sand, rather than being clustered in depressed areas. There were some powder-like materials found on the surface, but they have not been identified. One possibility is that they are HgS precipitates or macromolecular polymer-Hg complexes that formed on the surface.

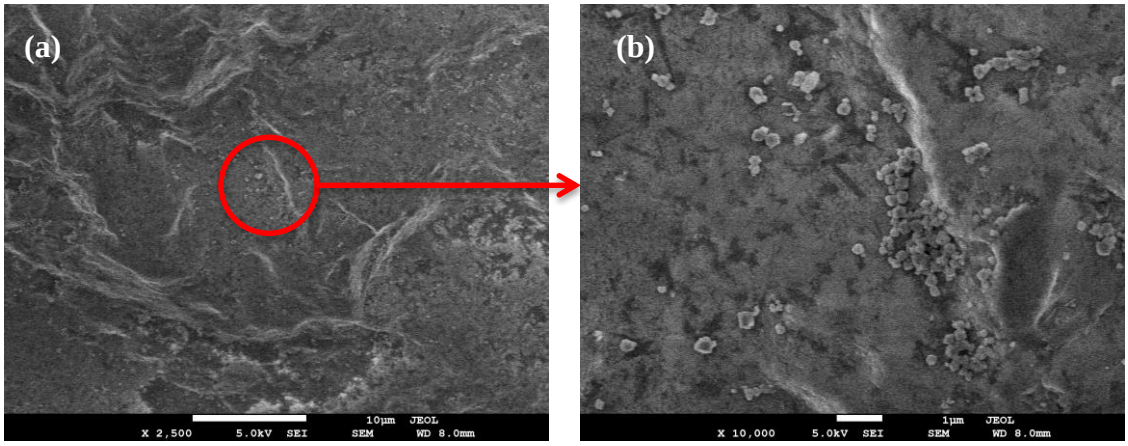

Figure 4.15 SEM micrographs of polymer/pyrite-coated sand after flow with 1 mg/L Hg(II) at pH 7. (a) SEM image at 2,500×; (b) SEM image at 10,000×.

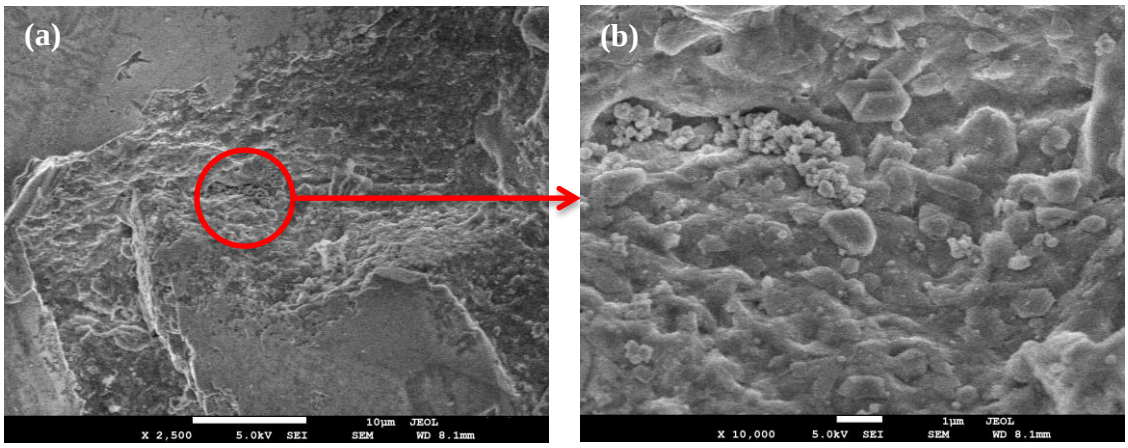

Figure 4.16 SEM micrographs of polymer/pyrite-coated sand after flow with 1 mg/L Hg(II) with 0.01 M salts at pH 7. (a) SEM image at 2,500×; (b) SEM image at 10,000×.

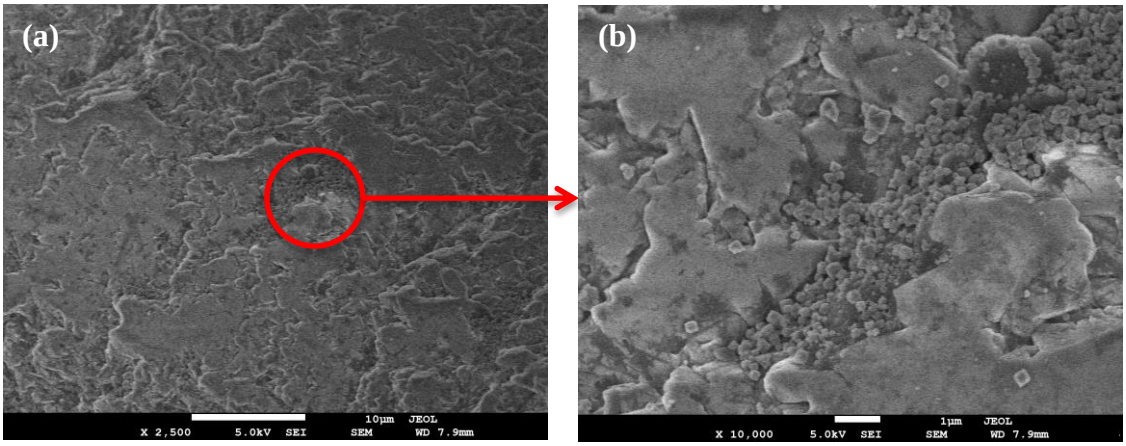

Figure 4.17 SEM micrographs of polymer/pyrite-coated sand after flow with 1 mg/L Hg(II) with 10 mg/L HAs at pH 7. (a) SEM image at 2,500×; (b) SEM image at 10,000×.

Figures 4.18 and 4.19 show the results for broad XPS scans and they indicate that the surface consisted of iron, oxygen, sulfur, carbon, calcium, silica, and mercury. Carbon was from the carbon tape, while the calcium was most likely from the polymer

because calcium peaks were not identified with pyrite-coated sand without polymers. Hg 4f7/2 peaks (99 eV – 102 eV) were very close to the Si 2p peaks (98 eV – 104 eV) so that they cannot be separated from each other. The silica peaks were weak compare to electrostatic attraction coating. This may be due to the polymers that covered the surface of the sand and the intensities of the peaks depend on the depth of the elements with respect to the surface.

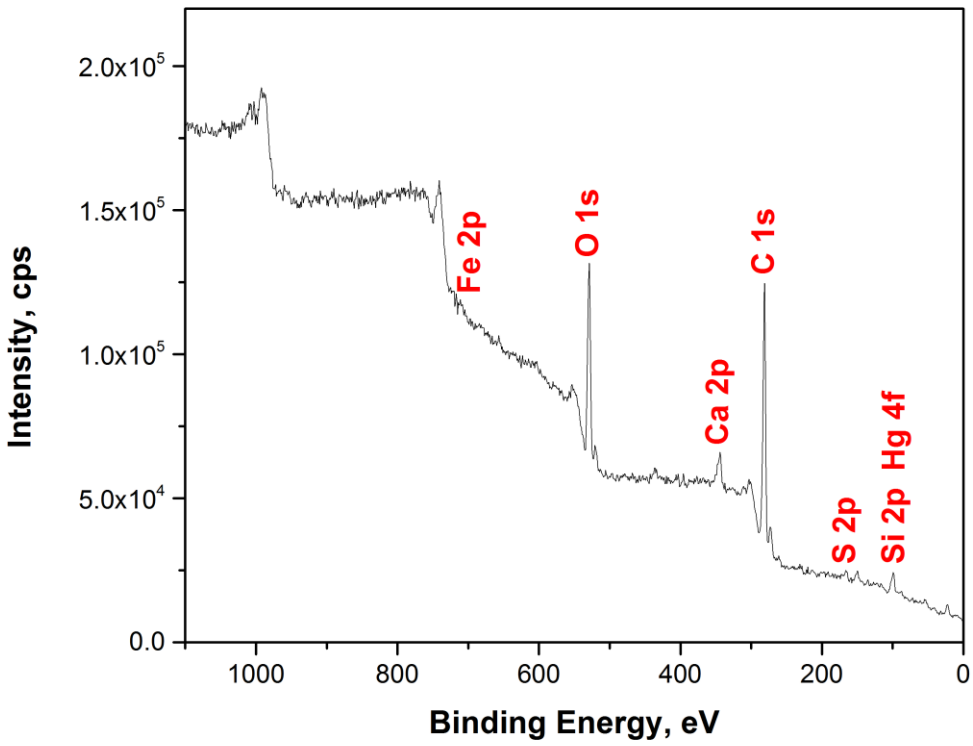

Figure 4.18 Broad scan for polymer/pyrite-coated sand after flow with 1 mg/L Hg at pH 7.

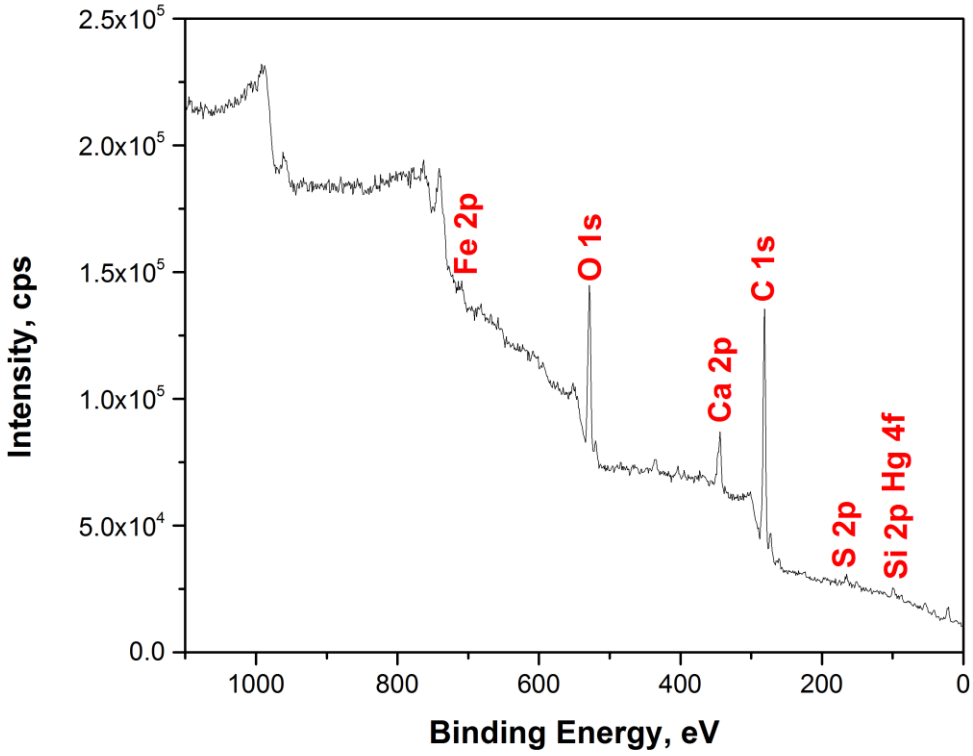

Figure 4.19 Broad scan for polymer/pyrite-coated sand after flow with 1 mg/L Hg with 10 mg/L HAs at pH 7.

To confirm the surface species, narrow scans of Fe 2p and S 2p spectra were also analyzed and the results are shown in Figures 4.20 and 4.21. The binding energy around 712 eV was the peak of Fe $2p_{3/2}$ which indicates the characteristic peaks of Fe(III) or FeS or $FeSO_4$. The peaks of S $2p_{3/2}$ were located near 170 eV, which indicates that the species was sulfate.

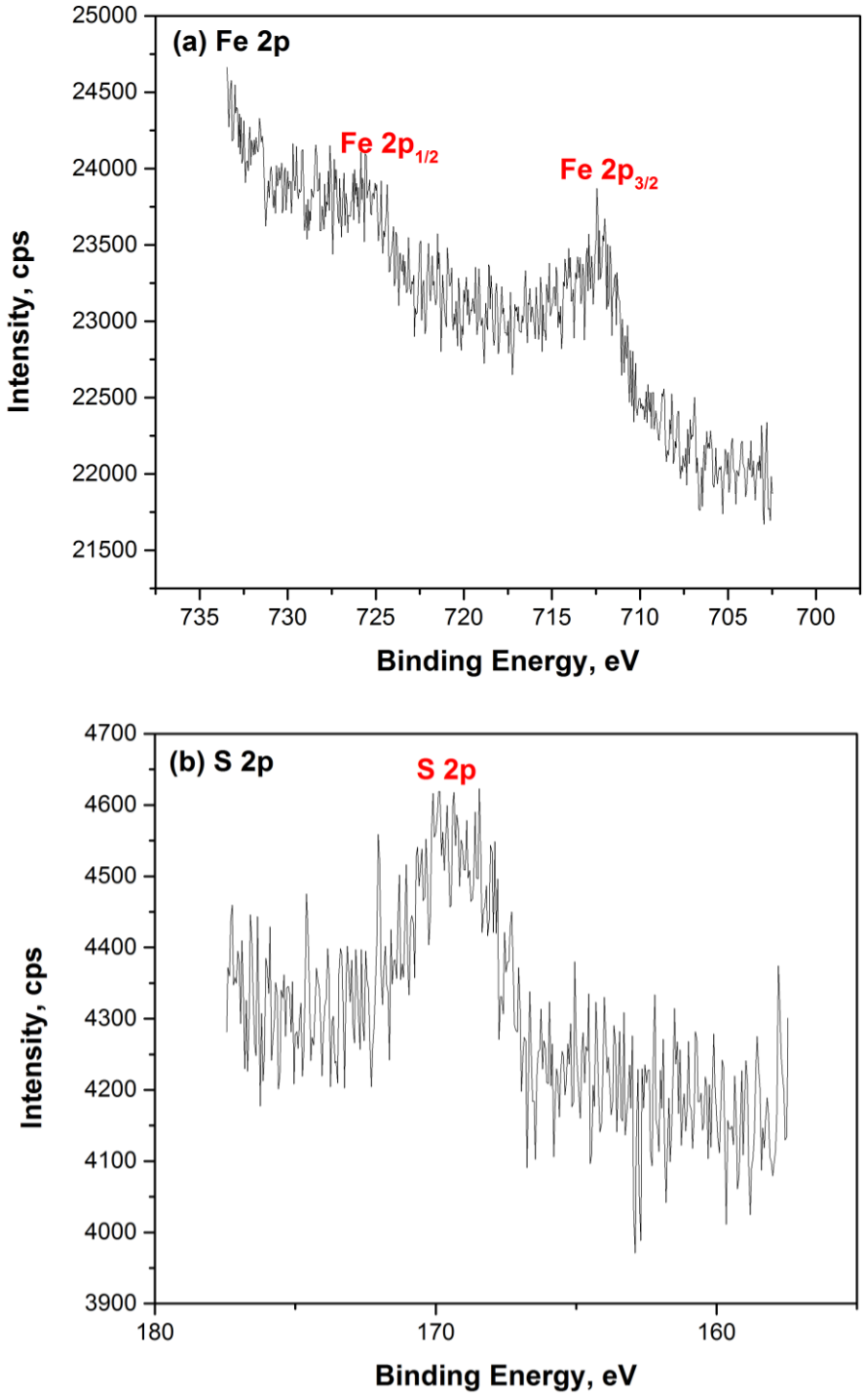

Figure 4.20 Narrow scans for pyrite coated sand after flow with 1 mg/L Hg at pH 7. (a) Fe 2p spectra; (b) S 2p spectra.

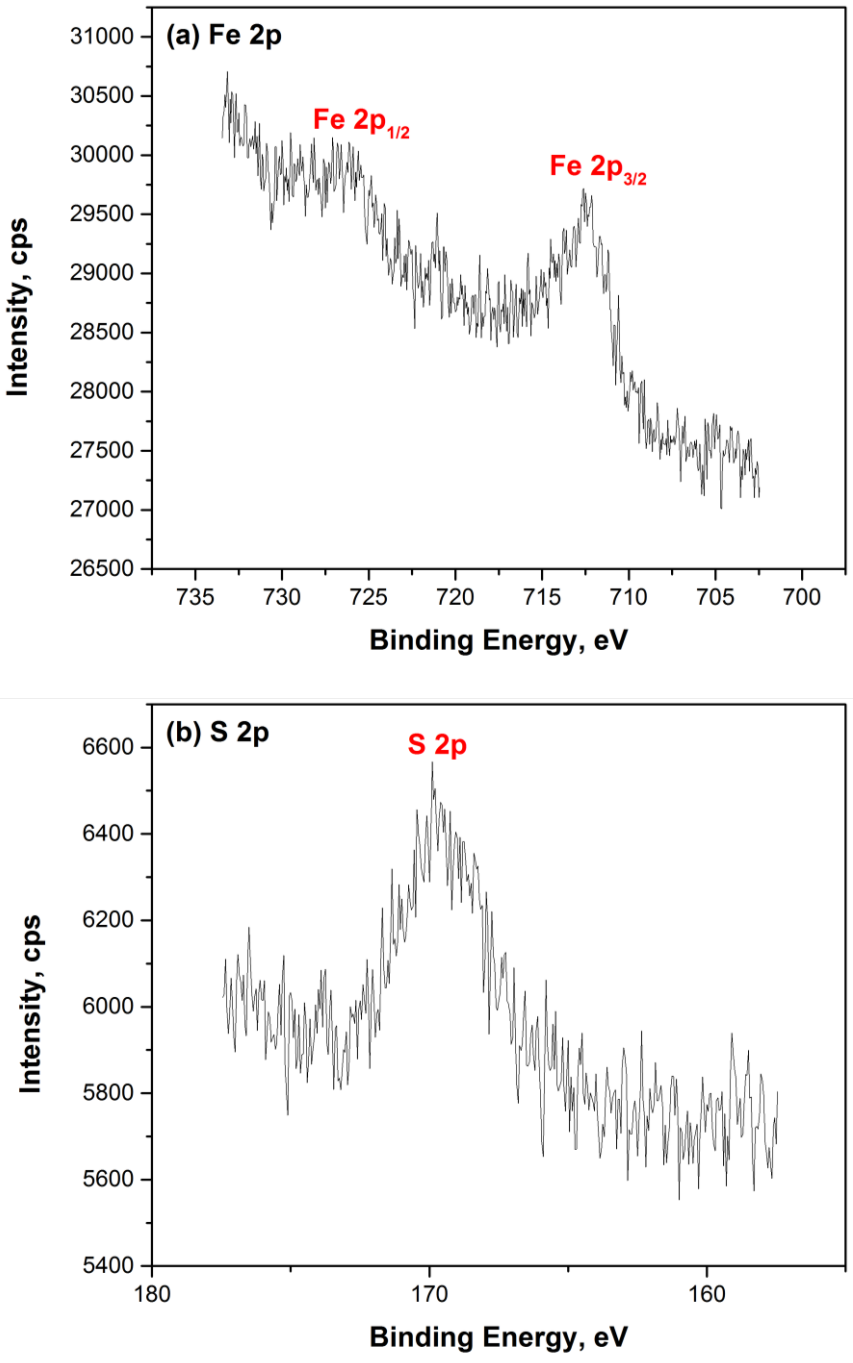

Figure 4.21 Narrow scans for pyrite coated sand after flow with 1 mg/L Hg with 10 mg/L HAs at pH 7. (a) Fe 2p spectra; (b) S 2p spectra.

4.4 Conclusion

Chemically-treated sand with P/S ratio of 1 mg/g at pH 7 has been chosen for electrostatic attraction coating of pyrite onto sand and the average amount of pyrite on sand was found to be 0.82 mg FeS_2/g sand. The removal capacity of mercury decreases as influent pH decreases, while the kinetics were faster when the pH was lower. This may be due to a layer of Fe (III) oxyhydroxide formed at higher pH that could present more adsorption sites for mercury. Faster kinetics was found with low HRT, which is consistent with external film transfer limiting removal kinetics. The presence of salts may desorb mercury from pyrite and result in decreased removal capacity but increased rate of mercury removal. The presence of HAs would slow mercury removal kinetics, but the removal capacity increases as the concentration of HAs increases. HAs may contain sulfur groups that complex with Hg(II). Differences in concentration between the filtered and unfiltered samples in the presence of HAs were large, which means most mercury in the effluent could be in a solid phase or in a form that can be adsorbed by the filter. Mercury could react with soluble HAs to produce mercury containing solid complexes. Both SEM/EDS and XPS did not detect any mercury compounds due to the low concentration of mercury compared to the other elements and the fact that silica peaks in XPS overlapped mercury peaks. However, Hg 4d peaks were identified by XPS and it could represent HgS, based on batch experiments presented in Chapter III.

For polymer/pyrite-coated sand, the removal capacity was much higher than that of pyrite-coated sand. The presence of salts increased the rate of mercury removal, but slightly decreased the amount of mercury removed. The presence of salts also increased

the differences between concentrations of Hg in filtered and unfiltered samples. The presence of HAs slower the mercury removal kinetics and lower the total removal capacity of Hg(II). Most mercury removal appeared to be associated with formation of solids or macromolecular complexes.

CHAPTER V

CONCLUSIONS

In this study, the feasibility of using synthesized near nano-scale pyrite particles as a reactive adsorbent for mercury removal was studied in both batch reactor system and column system. Pyrite has been demonstrated to be an excellent absorbent for removing mercury in many studies. However, most of them used natural pyrites that had been ground to particle sizes on the scale of microns or larger.

In Chapter II, near nano-sized pyrite was successfully synthesized within one minute. $FeCl_3$ and NaSH were used as the source chemicals to synthesize pyrite at pH 4.5 under anoxic conditions. Different aging methods, including hydrothermal, a variety of ultrasonic, and microwave irradiation were investigated to develop a fast and reliable method for synthesizing near nano-scale pyrite crystals that have high surface areas. Hydrothermal and ultrasonic methods generated more pyrite particles, but with longer aging times and larger particle sizes than methods using microwave irradiation. Microwave irradiation successfully synthesized pyrite particles between 100-200 nm with specific surface area of 20.1 m^2/g in only one minute with full irradiation power. The surface characteristic analyses demonstrated that the synthetic particles were mainly pyrite with lesser amounts of marcarsite. Results of SEM/EDS and XPS analyses indicate that polysulfides or elemental sulfur exists even after washing with acetone and carbon disulfide and that pyrite is formed by the reaction between iron monosulfide and polysulfides. Therefore, pyrite crystals were most likely formed via a FeS precursor.

In Chapter III, two types of batch experiments were performed. One measured the kinetics of the removal of mercury from solution and the other one measured mercury loading onto synthesized pyrite. Results of the kinetic experiments reveal an initially fast kinetics for mercury removal that is followed by either release/resorption pattern with high pyrite dose (0.1 g/L) or slower removal with lower pyrite dose (0.01 g/L). About 90% of 5 μmol /L Hg(II) was removed by 0.1 g/L pyrite in 5 minutes or less. However, mercury was then released, before being readsorbed to give substantially complete mercury removal after 12 hours. Release of mercury could be described by a reaction with sulfides and elemental sulfur to form soluble Hg-polysulfide-sulfide complexes, which would increase the concentration of total mercury in solution. Resorption of Hg could be caused by changes in the surface due to surface reactions or by changes in the soluble complexes that result in complexes that are more likely to be adsorbed by pyrite. The drop of pH observed in all kinetic experiments could be affected by the hydrogen ions released from the pyrite surface and the adsorption reaction of the pyrite surface with Hg(II). Addition of 0.01 mol/L sodium nitrate and sodium sulfate decreased mercury removal by about 20%.

Chapter III also addresses the effect of mercury loading on mercury removal. The results revealed that the maximum uptake of mercury on pyrite was 900 μmol Hg/g FeS_2. The amount of mercury adsorbed generally decreased in the presence of salts or humic acids. In each mercury loading experiment, pH followed a similar pattern. pH was observed to initially drop and then rise as more Hg(II) is added and removed from solution. The hydrogen ions released from the pyrite surface and the adsorption reaction

of the pyrite surface with Hg(II) would result in an initial pH drop with low mercury loading. The existence of two different sorption sites that have different affinities for Hg(II) and different effects on pH may explain the pH rising at high mercury loading. The pyritic sites are stronger than the hydroxide sites, so adsorption on pyritic sites would occur first until they were fully occupied. The acidity of the pyritic sites could lead to the release of protons during adsorption that lead to a pH drop. Hydroxide sites adsorb mercury less strongly and that reaction might consume protons. Furthermore, formation of soluble Hg-sulfide complexes and mercury sulfide solid phases would consume hydrogen ions resulting in pH increasing. Both salts and humic acids inhibit removal of Hg(II) by pyrite. The presence of salts may desorb mercury from pyrite surface to some extent. The inhibition by HAs was observed at the lowest concentration of HAs and was not observed to increase at higher concentrations. HAs could compete with Hg(II) for the binding sites on pyrite or could form soluble Hg-HAs complexes. The presence of HgS on the surface was revealed by XPS Hg 4f spectra, suggesting a surface precipitation process occurred.

In Chapter IV, the development of an optimum coating procedure of pyrite on sand through electrostatic attraction and polymer-based coating was presented. The results demonstrated that rinsing does not have a substantial effect on the amount of coating, but to reduce the variability, chemically-treated sand was chosen for further study. Higher mass of pyrite of coating on chemically-treated sand occurred at pH 7, which is close to pH_{pzc} of pyrite, than that at pH 4. The amount of coating was found to increase, when greater masses of pyrite were added. Therefore, chemically-treated sand

with P/S ratio of 1 mg/g at pH 7 was chosen for electrostatic attraction coating of pyrite onto sand and the average amount of pyrite on sand was found to be 0.82 mg FeS_2/g sand. The SEM results indicate a patchwise surface coating, where pyrite particles aggregated at indentations on the surface rather than on smooth surfaces. Polymer-based coating (0.36 mg/g) results in less than half of the pyrite concentration on sand achieved by the electrostatic attraction method (0.82 mg/g). But the polymer may have an effect on removal of Hg(II), so polymer/pyrite-coated sand was also used in column tests for comparison. Another method examined was to form pyrite on sand directly, but the efficiency of this method was much lower than the electrostatic attraction coating and any further development of this method was abandoned.

Chapter IV also examined the stability of pyrite-coated sand by electrostatic attraction. Pyrite would dissolve as water flow through the column, but the amount of pyrite lost is relatively small compared to the total amount of pyrite attached to the sand. It would take more than 4 days to consume all of the pyrite on sand surface by assuming the pyrite loss rate remains constant. Tracer tests with chemically-treated sand and pyrite-coated sand show that none of them represent an ideal plug flow system. But the HRT and the mean residence time are very close for both cases. A blank test with chemically-treated sand verified that chemically-treated sand itself would not remove any Hg(II).

Chapter IV also addresses the kinetics of mercury removal by the RACS system under different pH, HRT, and in the presence or absence of salts or HAs. For pyrite-coated sand by electrostatic attraction, the removal capacity of mercury decreases but

kinetics of removal are faster, as influent pH decreases. Decreasing HRT leads to faster kinetics, which is consistent with external film transfer limiting removal kinetics. The presence of salts decreased removal capacity but increased the rate of mercury removal. However, the presence of HAs slowed mercury removal kinetics, but the removal capacity increased as the concentration of HAs increased. None of mercury species were identified under SEM/EDS and XPS because of the low concentration of mercury compared to the other elements and the fact that silica peaks in XPS overlapped mercury peaks. However, Hg 4d peaks were identified by XPS and it could represent HgS, based on the results of batch experiments.

For polymer/pyrite-coated sand, the removal capacity was much higher than that of pyrite-coated sand. The presence of salts increased the rate of mercury removal, but slightly decreased the removal capacity. In contrast, the presence of HAs slowed mercury removal kinetics, but also lowered the total removal capacity of Hg(II). Most mercury removal appeared to be associated with formation of solids or macromolecular complexes.

An important result of this study is that it demonstrated how near nano-scale pyrite particles can be synthesized that have extremely high removal capacity for mercury. It also provided fundamental information that could be used to scale-up a column to produce high quality water from mercury-contaminated wastewater. Furthermore, because of the strong bond between mercury and pyrite, this system would produce residuals that are more stable during disposal than conventional adsorbents, such as activated carbon.

REFERENCES

1. USEPA. *Treatment technologies for mercury in soil, waste, and water*; EPA 542-R-07-003; USEPA, Office of Superfund Remediation and Technology Innovation: Washington, DC, 2007; http://www.epa.gov/tio/download/remed/542r07003.pdf.
2. USEPA. *Cleaner power plant* Website; http://www.epa.gov/mats/powerplants.html.
3. Vieira, R. S.; Beppu, M. M., Dynamic and static adsorption and desorption of Hg(II) ions on chitosan membranes and spheres. *Water Research* **2006,** *40*, (8), 1726-1734.
4. Weisener, C. G.; Sale, K. S.; Smyth, D. J. A.; Blowes, D. W., Field column study using zerovalent iron for mercury removal from contaminated groundwater. *Environmental Science & Technology* **2005,** *39*, (16), 6306-6312.
5. Nriagu, J. O., *The biogeochemistry of mercury in the environment*. Elsevier/North-Holland Biomedical Press: Amsterdam, North-Holland, 1979.
6. Sadiq, M., *Toxic metal chemistry in marine environments*. Marcel Dekker Inc.: New York, 1992.
7. Dyrssen, D.; Wedborg, M., The sulphur-mercury(II) system in natural waters. *Water, Air, and Soil Pollution* **1991,** *56*, (1), 507-519.
8. Ravichandran, M.; Aiken, G. R.; Ryan, J. N.; Reddy, M. M., Inhibition of precipitation and aggregation of metacinnabar (mercuric sulfide) by dissolved

organic matter isolated from the Florida Everglades. *Environmental Science & Technology* **1999,** *33*, (9), 1418-1423.

9. Skyllberg, U.; Bloom, P. R.; Qian, J.; Lin, C.-M.; Bleam, W. F., Complexation of mercury(II) in soil organic matter: EXAFS evidence for linear two-coordination with reduced sulfur groups. *Environmental Science & Technology* **2006,** *40*, (13), 4174-4180.

10. Jeong, H. Y.; Klaue, B.; Blum, J. D.; Hayes, K. F., Sorption of mercuric ion by synthetic nanocrystalline mackinawite (FeS). *Environmental Science & Technology* **2007,** *41*, (22), 7699-7705.

11. Kaneko, K., Dynamic Hg(II) adsorption characterization of iron oxide-dispersed activated carbon fibers. *Carbon* **1988,** *26*, (6), 903-905.

12. USEPA. *National primary drinking water regulations*; EPA 816-F-09-004; USEPA: Washington, DC, 2009; http://water.epa.gov/drink/contaminants/upload/mcl-2.pdf.

13. USEPA. *Integrated risk information system (IRIS) on elemental mercury*. National Center for Environmental Assessment, Office of Research and Development: Washington, DC, 1999.

14. USEPA. *Integrated risk information system (IRIS) on mercury chloride*. National Center for Environmental Assessment, Office of Research and Development: Washington, DC, 1999.

15. USEPA. *Integrated risk information system (IRIS) on methyl mercury*. National Center for Environmental Assessment, Office of Research and Development: Washington, DC, 1999.

16. USEPA. *2011 Edition of the drinking water standards and health advisories*; EPA 820-R-11-002; USEPA: Office of Water: Washington, DC, 2011; http://water.epa.gov/action/advisories/drinking/upload/dwstandards2011.pdf.

17. USEPA. *Standard operating procedures-determination of mercury by cold-vapor atomic absorption (CVAA)-revision 3.0*; EPA/SW-846 Methods 7000A/7470A/7471A; USEPA: Washington, DC, 2006; https://clu-in.org/download/ert/1832-r30.pdf.

18. von Canstein, H.; Li, Y.; Timmis, K. N.; Deckwer, W. D.; Wagner-Döbler, I., Removal of mercury from chloralkali electrolysis wastewater by a mercury-resistant pseudomonas putida strain. *Applied and Environmental Microbiology* **1999,** *65*, (12), 5279-5284.

19. Kiyono, M.; Omura, H.; Omura, T.; Murata, S.; Pan-Hou, H., Removal of inorganic and organic mercurials by immobilized bacteria having mer-ppk fusion plasmids. *Appl Microbiol Biotechnol* **2003,** *62*, (2-3), 274-278.

20. Daughney, C. J.; Siciliano, S. D.; Rencz, A. N.; Lean, D.; Fortin, D., Hg(II) adsorption by bacteria: A surface complexation model and its application to shallow acidic lakes and wetlands in Kejimkujik National Park, Nova Scotia, Canada. *Environmental Science & Technology* **2002,** *36*, (7), 1546-1553.

21. Wang, J.; Feng, X.; Anderson, C. W. N.; Xing, Y.; Shang, L., Remediation of mercury contaminated sites – A review. *Journal of Hazardous Materials* **2012,** *221–222*, 1-18.

22. Yan, R.; Yang, F.; Wu, Y.; Hu, Z.; Nath, B.; Yang, L.; Fang, Y., Cadmium and mercury removal from non-point source wastewater by a hybrid bioreactor. *Bioresource Technology* **2011,** *102*, (21), 9927-9932.

23. Rao, M. M.; Reddy, D. H. K. K.; Venkateswarlu, P.; Seshaiah, K., Removal of mercury from aqueous solutions using activated carbon prepared from agricultural by-product/waste. *Journal of Environmental Management* **2009,** *90*, (1), 634-643.

24. Mohan, D.; Gupta, V. K.; Srivastava, S. K.; Chander, S., Kinetics of mercury adsorption from wastewater using activated carbon derived from fertilizer waste. *Colloids and Surfaces A: Physicochemical and Engineering Aspects* **2001,** *177*, (2–3), 169-181.

25. Hsi, H.; Rood, M.; Rostam-Abadi, M.; Chen, S.; Chang, R., Mercury Adsorption Properties of Sulfur-Impregnated Adsorbents. *Journal of Environmental Engineering* **2002,** *128*, (11), 1080-1089.

26. Oubagaranadin, J. U. K.; Sathyamurthy, N.; Murthy, Z. V. P., Evaluation of Fuller's earth for the adsorption of mercury from aqueous solutions: A comparative study with activated carbon. *Journal of Hazardous Materials* **2007,** *142*, (1–2), 165-174.

27. Pérez-Quintanilla, D.; Hierro, I. d.; Fajardo, M.; Sierra, I., 2-Mercaptothiazoline modified mesoporous silica for mercury removal from aqueous media. *Journal of Hazardous Materials* **2006,** *134*, (1–3), 245-256.

28. De Canck, E.; Lapeire, L.; De Clercq, J.; Verpoort, F.; Van Der Voort, P., New ultrastable mesoporous adsorbent for the removal of mercury ions. *Langmuir* **2010,** *26*, (12), 10076-10083.

29. Bäckström, M.; Dario, M.; Karlsson, S.; Allard, B., Effects of a fulvic acid on the adsorption of mercury and cadmium on goethite. *Science of The Total Environment* **2003,** *304*, (1–3), 257-268.

30. Wang, Y.; Li, B.; Zhang, L.; Li, P.; Wang, L.; Zhang, J., Multifunctional magnetic mesoporous silica nanocomposites with improved sensing performance and effective removal ability toward Hg(II). *Langmuir* **2012,** *28*, (2), 1657-1662.

31. Lo, S.-I.; Chen, P.-C.; Huang, C.-C.; Chang, H.-T., Gold nanoparticle–aluminum oxide adsorbent for efficient removal of mercury species from natural waters. *Environmental Science & Technology* **2012,** *46*, (5), 2724-2730.

32. Song, B. Y.; Eom, Y.; Lee, T. G., Removal and recovery of mercury from aqueous solution using magnetic silica nanocomposites. *Applied Surface Science* **2011,** *257*, (10), 4754-4759.

33. Dou, B.; Chen, H., Removal of toxic mercury(II) from aquatic solutions by synthesized TiO2 nanoparticles. *Desalination* **2011,** *269*, (1–3), 260-265.

34. Hyland, M. M.; Jean, G. E.; Bancroft, G. M., XPS and AES studies of Hg(II) sorption and desorption reactions on sulphide minerals. *Geochimica et Cosmochimica Acta* **1990,** *54*, (7), 1957-1967.

35. Belzile, N.; Lebel, J., Capture of arsenic by pyrite in near-shore marine sediments. *Chemical Geology* **1986,** *54*, (3–4), 279-281.

36. Moore, J. N.; Ficklin, W. H.; Johns, C., Partitioning of arsenic and metals in reducing sulfidic sediments. *Environmental Science & Technology* **1988,** *22*, (4), 432-437.

37. Bower, J.; Savage, K. S.; Weinman, B.; Barnett, M. O.; Hamilton, W. P.; Harper, W. F., Immobilization of mercury by pyrite (FeS2). *Environmental Pollution* **2008,** *156*, (2), 504-514.

38. Liu, J.; Valsaraj, K. T.; Devai, I.; DeLaune, R. D., Immobilization of aqueous Hg(II) by mackinawite (FeS). *Journal of Hazardous Materials* **2008,** *157*, (2–3), 432-440.

39. Svensson, M.; Allard, B.; Düker, A., Formation of HgS—mixing HgO or elemental Hg with S, FeS or FeS2. *Science of The Total Environment* **2006,** *368*, (1), 418-423.

40. Behra, P.; Bonnissel-Gissinger, P.; Alnot, M.; Revel, R.; Ehrhardt, J. J., XPS and XAS study of the sorption of Hg(II) onto pyrite. *Langmuir* **2001,** *17*, (13), 3970-3979.

41. Han, D. S.; Orillano, M.; Khodary, A.; Duan, Y.; Batchelor, B.; Abdel-Wahab, A., Reactive iron sulfide (FeS)-supported ultrafiltration for removal of mercury (Hg(II)) from water. *Water Research* **2014,** *53*, 310-321.

42. Han, D. S.; Kim, E. J.; Batchelor, B.; Abdel-Wahab, A., Sorption of Hg(II) to synthesized pyrite (FeS2) and stabilization via surface reactions. In *Pyrite: synthesis, characterization and uses*, Whitley, N.; Vinsen, P. T., Eds. Nova Science Publishers: New York, 2012; pp 93-122.

43. Kim, E. J.; Batchelor, B., Synthesis and characterization of pyrite (FeS2) using microwave irradiation. *Materials Research Bulletin* **2009,** *44*, (7), 1553-1558.

44. Ehrhardt, J.-J.; Behra, P.; Bonnissel-Gissinger, P.; Alnot, M., XPS study of the sorption of Hg(II) onto pyrite FeS2. *Surface and Interface Analysis* **2000,** *30*, (1), 269-272.

45. Jay, J. A.; Morel, F. M. M.; Hemond, H. F., Mercury speciation in the presence of polysulfides. *Environmental Science & Technology* **2000,** *34*, (11), 2196-2200.

46. Liu, J.; Valsaraj, K. T.; Delaune, R. D., Inhibition of mercury methylation by iron sulfides in an anoxic sediment. *Environmental Engineering Science* **2009,** *26*, (4), 833-840.

47. Slowey, A. J.; Brown Jr, G. E., Transformations of mercury, iron, and sulfur during the reductive dissolution of iron oxyhydroxide by sulfide. *Geochimica et Cosmochimica Acta* **2007,** *71*, (4), 877-894.

48. Perdicakis, M.; Grosselin, N.; Bessière, J., Interaction of pyrite pulps with Ag+ and Hg2+ ions. Electrochemical characterization of micrometric grains. *Analytica Chimica Acta* **1999,** *385*, (1–3), 467-485.

49. Scheidegger, A.; Borkovec, M.; Sticher, H., Coating of silica sand with goethite: preparation and analytical identification. *Geoderma* **1993,** *58*, (1–2), 43-65.

50. Han, Y.-S.; Gallegos, T. J.; Demond, A. H.; Hayes, K. F., FeS-coated sand for removal of arsenic(III) under anaerobic conditions in permeable reactive barriers. *Water Research* **2011,** *45*, (2), 593-604.

51. Xu, Y.; Axe, L., Synthesis and characterization of iron oxide-coated silica and its effect on metal adsorption. *Journal of Colloid and Interface Science* **2005,** *282*, (1), 11-19.

52. Jaber, J. A.; Schlenoff, J. B., Mechanical properties of reversibly cross-linked ultrathin polyelectrolyte complexes. *Journal of the American Chemical Society* **2006,** *128*, (9), 2940-2947.

53. Dotzauer, D. M.; Bhattacharjee, S.; Wen, Y.; Bruening, M. L., Nanoparticle-containing membranes for the catalytic reduction of nitroaromatic compounds. *Langmuir* **2009,** *25*, (3), 1865-1871.

54. Dotzauer, D. M.; Dai, J.; Sun, L.; Bruening, M. L., Catalytic membranes prepared using layer-by-layer adsorption of polyelectrolyte/metal nanoparticle films in porous supports. *Nano Letters* **2006,** *6*, (10), 2268-2272.

55. Wei, D.; Osseo-Asare, K., Particulate pyrite formation by the Fe3+/HS− reaction in aqueous solutions: effects of solution composition. *Colloids and Surfaces A: Physicochemical and Engineering Aspects* **1996,** *118*, (1–2), 51-61.

56. Han, D. S.; Song, J. K.; Batchelor, B.; Abdel-Wahab, A., Removal of arsenite(As(III)) and arsenate(As(V)) by synthetic pyrite (FeS2): Synthesis, effect of contact time, and sorption/desorption envelopes. *Journal of Colloid and Interface Science* **2013,** *392*, 311-318.

57. Bonnissel-Gissinger, P.; Alnot, M.; Ehrhardt, J.-J.; Behra, P., Surface oxidation of pyrite as a function of pH. *Environmental Science & Technology* **1998,** *32*, (19), 2839-2845.

58. Roberts, W. M. B.; Walker, A. L.; Buchanan, A. S., The chemistry of pyrite formation in aqueous solution and its relation to the depositional environment. *Mineral. Deposita* **1969,** *4*, (1), 18-29.

59. Schoonen, M. A. A.; Barnes, H. L., Reactions forming pyrite and marcasite from solution: II. Via FeS precursors below 100°C. *Geochimica et Cosmochimica Acta* **1991,** *55*, (6), 1505-1514.

60. Murowchick, J. B.; Barnes, H. L., Marcasite precipitation from hydrothermal solutions. *Geochimica et Cosmochimica Acta* **1986,** *50*, (12), 2615-2629.

61. Huang, J. H.; Rowson, N. A., Heating characteristics and decomposition of pyrite and marcasite in a microwave field. *Minerals Engineering* **2001,** *14*, (9), 1113-1117.

62. Berner, R. A., Sedimentary pyrite formation. *Amer. J. Sci.* **1970,** *268*, 1-23.

63. Berner, R. A., Sedimentary pyrite formation: An update. *Geochimica et Cosmochimica Acta* **1984,** *48*, (4), 605-615.

64. Schoonen, M. A. A.; Barnes, H. L., Reactions forming pyrite and marcasite from solution: I. Nucleation of FeS2 below 100°C. *Geochimica et Cosmochimica Acta* **1991,** *55*, (6), 1495-1504.

65. Wilkin, R. T.; Barnes, H. L., Pyrite formation by reactions of iron monosulfides with dissolved inorganic and organic sulfur species. *Geochimica et Cosmochimica Acta* **1996,** *60*, (21), 4167-4179.

66. Rickard, D. T., Kinetics and mechanism of pyrite formation at low temperatures. *American Journal of Science* **1975,** *275*, (6), 636-652.

67. Wang, Q.; Morse, J. W., Pyrite formation under conditions approximating those in anoxic sediments I. Pathway and morphology. *Marine Chemistry* **1996,** *52*, (2), 99-121.

68. Luther III, G. W., Pyrite synthesis via polysulfide compounds. *Geochimica et Cosmochimica Acta* **1991,** *55*, (10), 2839-2849.

69. Butler, I.; Grimes, S.; Rickard, D. Pyrite formation in an anoxic chemostatic reaction system. *Journal of Conference Abstracts* **2000**, *5*, 274-275.

70. Schoonen, M. A. A.; Barnes, H. L., Mechanisms of pyrite and marcasite formation from solution: III. Hydrothermal processes. *Geochimica et Cosmochimica Acta* **1991,** *55*, (12), 3491-3504.

71. Naumkin, A. V.; Kraut-Vass, A.; Gaarenstroom, S. W.; Powell, C. J., NIST X-ray photoelectron spectroscopy database: NIST standard reference database 20, version 4.1. NIST, 2012.

72. Pratt, A. R.; Muir, I. J.; Nesbitt, H. W., X-ray photoelectron and Auger electron spectroscopic studies of pyrrhotite and mechanism of air oxidation. *Geochimica et Cosmochimica Acta* **1994,** *58,* (2), 827-841.

73. Bostick, B. C.; Fendorf, S., Arsenite sorption on troilite (FeS) and pyrite (FeS2). *Geochimica et Cosmochimica Acta* **2003,** *67*, (5), 909-921.

74. Nesbitt, H. W.; Muir, I. J., X-ray photoelectron spectroscopic study of a pristine pyrite surface reacted with water vapour and air. *Geochimica et Cosmochimica Acta* **1994,** *58*, (21), 4667-4679.

75. Namasivayam, C.; Periasamy, K., Bicarbonate-treated peanut hull carbon for mercury (II) removal from aqueous solution. *Water Research* **1993,** *27*, (11), 1663-1668.

76. Kim, C. S.; Rytuba, J. J.; Brown Jr, G. E., EXAFS study of mercury(II) sorption to Fe- and Al-(hydr)oxides: I. Effects of pH. *Journal of Colloid and Interface Science* **2004,** *271*, (1), 1-15.

77. Watson, J. H. P.; Ellwood, D. C.; Deng, Q.; Mikhalovsky, S.; Hayter, C. E.; Evans, J., Heavy metal adsorption on bacterially produced FeS. *Minerals Engineering* **1995,** *8*, (10), 1097-1108.

78. Jean, G. E.; Bancroft, G. M., Heavy metal adsorption by sulphide mineral surfaces. *Geochimica et Cosmochimica Acta* **1986,** *50,* (7), 1455-1463.

79. Liang, P.; Li, Y.-C.; Zhang, C.; Wu, S.-C.; Cui, H.-J.; Yu, S.; Wong, M. H., Effects of salinity and humic acid on the sorption of Hg on Fe and Mn hydroxides. *Journal of Hazardous Materials* **2013,** *244–245*, 322-328.

80. Deonarine, A.; Hsu-Kim, H., Precipitation of mercuric sulfide nanoparticles in NOM-containing water: implications for the natural environment. *Environmental Science & Technology* **2009,** *43*, (7), 2368-2373.

81. Skyllberg, U.; Drott, A., Competition between disordered iron sulfide and natural organic matter associated thiols for mercury(II)—An EXAFS study. *Environmental Science & Technology* **2010,** *44*, (4), 1254-1259.

82. Trost, P. B. Effects of humic-acid-type organics on secondary dispersion of mercury. Ph.D. Dissertation, Colorado School of Mines, Golden, CO, 1970.

83. Reimers, R. S.; Krenkel, P. A.; Eagle, M.; Tragitt, G., Sorption phenomenon in the organics of bottom sediments. In *Heavy Metals in the Aquatic Environment: An International Conference*, Krenkel, P. A., Ed. Pergamon Press: Oxford 1975; p 117.

84. Han, D. S., Removal of mercury from wastewater using reactive adsorbent/membrane (RAM) hydrid filtration process. Unpublished data.

85. Ruthven, D. M., Dynamics of adsorption columns: single-transition systems. In *Principles of adsorption and adsorption processes*, Ruthven, D. M., Ed. John Wiley & Sons, Inc.: New York, 1984; pp 220-273.

86. Xia, K.; Skyllberg, U. L.; Bleam, W. F.; Bloom, P. R.; Nater, E. A.; Helmke, P. A., X-ray absorption spectroscopic evidence for the complexation of Hg(II) by

reduced sulfur in soil humic substances. *Environmental Science & Technology* **1999,** *33*, (2), 257-261.

87. Zhang, J.; Dai, J.; Wang, R.; Li, F.; Wang, W., Adsorption and desorption of divalent mercury (Hg2+) on humic acids and fulvic acids extracted from typical soils in China. *Colloids and Surfaces A: Physicochemical and Engineering Aspects* **2009,** *335*, (1–3), 194-201.

88. Chaufer, B.; Deratani, A., Removal of metal ions by complexation-ultrafiltration using water-soluble macromolecules: Perspective of application to wastewater treatment. *Nuclear and Chemical Waste Management* **1988,** *8*, (3), 175-187.

89. Uludag, Y.; Özbelge, H. Ö.; Yilmaz, L., Removal of mercury from aqueous solutions via polymer-enhanced ultrafiltration. *Journal of Membrane Science* **1997,** *129*, (1), 93-99.

90. Pederson, E. D.; Stone, M. E.; Ovsey, V. G., The removal of mercury from dental-operatory wastewater by polymer treatment. *Environmental Health Perspectives* **1999,** *107*, (1), 3-8.

91. Cheng, H.; Yu, J.; Zeng, K.; Hou, G., Application of poly(acrylic acid)-multiwalled carbon nanotube composite for enrichment of rrace Hg(II). *Plasma Processes and Polymers* **2013,** *10*, (11), 931-937.

APPENDIX A

ADDITIONAL FIGURES

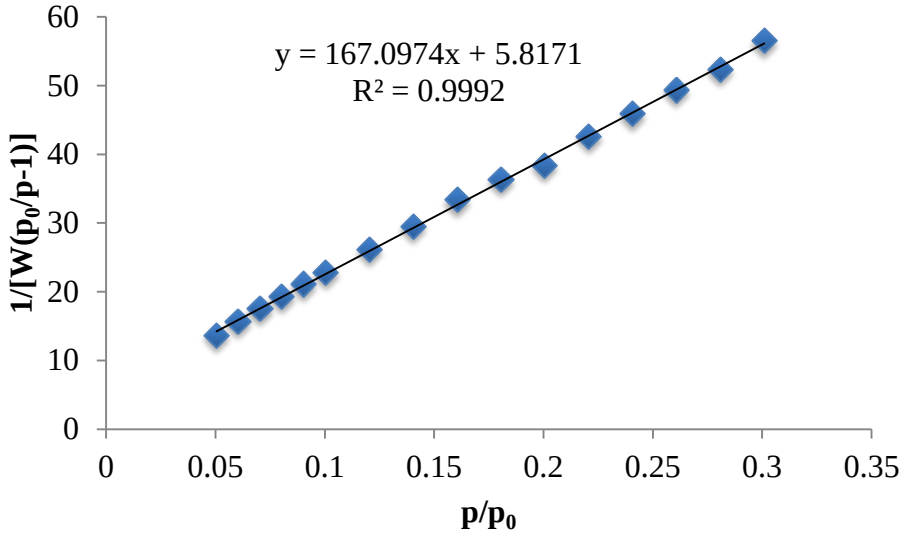

Figure A.1 Multipoint BET plot.

Slope (s) = 167.10

Intercept (i) = 5.82

Wm = 1/(s+i) = 0.0058 (weight of mass adsorbed as monolayer / weight of sample)

Avogadro's number (N) = 6.023×10^{23} mol^{-1}

Adsorbate cross sectional area (A) = 16.2 $Å^2$ = 0.162×10^{-18} m^2

Molecular weight of adsorbate (M) = 28 g/mol

Specific surface Area (S) = $\frac{W_m N A}{M}$ = 20.1 m^2/g

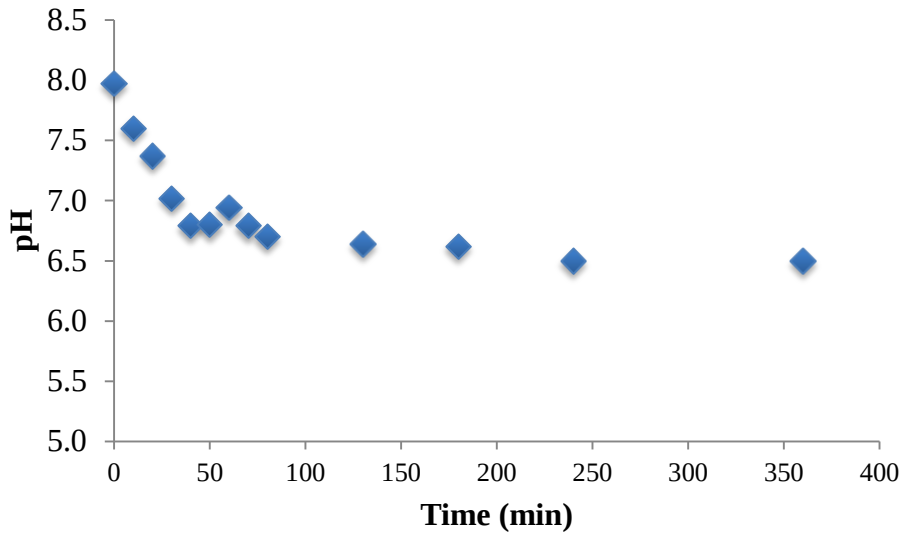

Figure A.2 pH of 0.1 g/L pyrite suspension over time after adjustment to pH 8 with NaOH.

APPENDIX B

MATLAB CODES

B.1 Computer Program (MATLAB) to Predict Model Parameters of Saturation Function Relationship and Power Law Relationship

```
% This script m-file calculate model values and is used by nlinfit.m
function cmod=calcmod1(beta,t,testdata)
a=beta(1);
b=beta(2);
cmod=a.*b.*c/(1+b.*c); or cmod=a.*c.^b;

% This script m-file inputs data and calls nlinfit.m to conduct non-linear least squares regression, and calls nlparic.m to calculate confidence intervals
data = load('data.txt');   % data.txt is the name of a text file that contains the data used in the regression.
                % It is a matrix with the first column holding the values of the independent variable (e.g. time)
                % The subsequent columns hold values of the dependent variables (e.g. concentration)
                % The data file must be in a directory accessible to MATLAB
t = data(:,1);          % measured values of time
cmeas = data(:,2);      % measured values of concentration
beta0 = [#, #];      % initial guesses for values of parameters to be determined
[beta,resid,j]=nlinfit(t,cmeas,@calcmod,beta0);
                % call nlinfit.m to do least-squares regression
                % calcmod.m is function that returns values of
                % model concentrations given values of time and
```

```
                    % parameters beta.  Uses format
                    % cmod=calcmod(beta,t), where cmod is vector of
                    % model values of independent variable (e.g.
                    % concentration)
betaci=nlparci(beta,resid,j);   %  call function to calculate confidence intervals
beta                % print to screen values of parameters
betaci              % print to screen confidence intervals for parameters
```

APPENDIX C

FERROZINE METHOD FOR IRON ANALYSIS

General idea: Dissolved Fe(II) concentrations in waters are commonly determined by a colorimetric technique using a ferrozine complexing reagent. If samples are colored or turbid, carry a sample set with ferrozine and another sample set without ferrozine. Read each sample developed with ferrozine against the corresponding blank without ferrozine. The difference can be applied to get iron concentration.

C.1 Apparatus

1) Spectrophotometer: (UV-visible spectrophotometer we use in our lab, for use at 562 nm, with light path of 1 cm.)

2) Volumetric Flask, 50 mL, 100 mL

3) Pipettes: 0.5 mL, 1.0 mL, 5.0 mL, 10mL

4) Amber glass bottles: 100mL, 250mL

5) Centrifuge tube: 15mL

Note: All glassware should be acid washed with dilute nitric acid (2%) and then rinsed with deionized water at least three times prior to use.

C.2 Reagents

1) Ferrous ammonium sulfate ($Fe(NH_4)_2(SO4)_2 \cdot 6H_2O$,purity 99.997%)

2) Ferrozine (3-(2-pyridyl)-5,6-diphenyl-1,2,4-triazine-p,p'-disulfonic acid)

3) Ammonium acetate, $NH_4C_2H_3O_2$

4) Hydroxylamine hydrochloride, $NH_2OH \cdot HCl$

5) HCl, concentrated

6) HNO_3, concentrated

7) H_2SO_4, concentrated

C.3 Reagents preparation

1) 1000 ppm Ferrous Iron stock solution (commercial standard solution or make as follows)

Step1: Slowly add 2 mL of concentrated H_2SO_4 to 5 mL of DI water

Step2: Dissolve 0.7020 g of $Fe(NH_4)_2(SO4)_2 \cdot 6H_2O$

Step3: Dilute to 100 mL with DI water and mix well

Step4: Store the ferrous iron stock solution in a amber glass bottle

2) Ferrous Iron standard solution (Prepare daily for use)

a) 50 ppm standard solution

Take 5 mL of stock solution and dilute to 100 mL with 1.2 N HCl (using volumetric flask)

Or take 0.5 mL of stock solution and dilute to 10 mL with 1.2 N HCl (using centrifuge tube)

b) 0.5, 2.5, 5, 7.5 and 10 ppm standard solution

Take 1, 5, 10, 15 and 20 mL of 50 ppm standard solution and dilute to 100 mL with 1.2 N HCl

Or take 0.1, 0.5, 1, 1.5 and 2 mL of 50 ppm standard solution and dilute to 10 mL with 1.2 N HCl

3) 1.2 N HCl

900 ml of DI water + 100 ml of Concentrated HCl into 1 L bottle

4) Ferrozine Solution

Step1: Place 0.15 g of Ferrozine in a 50 mL volumetric flask

Step2: Dissolve it with DI water containing 1 drop of concentrated HCl

Step3: Dilute to 50 mL

Step4: Store the Ferrozine solution in amber glass bottle

5) Acetate Buffer Solution

We use concentrated ammonium acetate buffer solution (for iron analysis) obtained commercially

Or it can be prepared as described in page 451 of *Standard Methods for the Examination of Water and Wastewater*, 20^{th} edition

6) Acid Quench Solution (0.7 M HNO_3)

955 mL of DI water + 45 mL of concentrated HNO_3. Store in glass bottle.

8) Reductant Solution (10% of hydroxylamine hydrochloride Solution)

Dilute 10 g of $NH_2OH{\cdot}HCl$ in 100 mL of water. Store in an amber glass bottle.

C.4 Procedures of ferrous iron and total iron analysis

1) Instrument setup

Step1: Turn on Software (software name: UV-visible Chemstation)

Step2: Load method: (we can choose spectrum/peaks method or quantification method)

Note: If we use spectrum/peaks, the results will show three biggest peaks; if we use quantification method, we need set up wavelength at 562 nm.

Step3: Turn on the lamp. (Instrument -> lamp on)

Step4: Wait for about 30minutes before absorbance measurement

2) Calibration standard

Step1: Transfer 1 mL of each standard ferrous iron solution to a spectrophotometer cell

Step2: Add 0.2 mL of DI water and 0.8 mL of Acetate Buffer Solution

Step3: Add 1 mL of Acid Quench solution

Step4: Mix well and allow 5 to 10 minutes for full color development

Step5: Measure the absorbance of iron-ferrozine complex and plot the standard curve

Step6: Transfer 1 mL of each standard ferrous iron solution to a spectrophotometer cell

Step7: Add 0.2 mL of Ferrozine Solution and 0.8 mL of Acetate Buffer Solution

Step8: Add 1 mL of Acid Quench solution

Step9: Mix well and allow 5 to 10 minutes for full color development

Step10: Measure the absorbance of iron-ferrozine complex

Step11: Reduce the absorbance with ferrozine by the absorbance without ferrozine and plot the standard curve

3) Samples blank for Ferrous Iron Analysis

Step1: Transfer 1 mL of sample to a spectrophotometer cell

Step2: Add 0.2 mL of DI water and 0.8 mL of Acetate Buffer Solution

Step3: Add 1 mL of Acid Quench solution

Step4: Mix well and allow 5 to 10 minutes for full color development

Step5: Measure the absorbance of iron-ferrozine complex

4) Samples for Ferrous Iron Analysis

Step1: Transfer 1 mL of sample to a spectrophotometer cell

Step2: Add 0.2 mL of Ferrozine Solution and 0.8 mL of Acetate Buffer Solution

Step3: Add 1 mL of Acid Quench solution

Step4: Mix well and allow 5 to 10 minutes for full color development

Step5: Measure the absorbance of iron-ferrozine complex

Step6: Reduce the sample absorbance by the sample blank absorbance

Step7: Determine the concentration of ferrous iron in sample using standard curve

5) Samples for Total Iron Analysis

Step1: Transfer 1 mL of sample to a spectrophotometer cell

Step2: Add 1 mL of Reductant solution

Step3: Add 0.2 mL of Ferrozine Solution and 0.8 mL of Acetate Buffer Solution

Step4: Mix well and allow 5 to 10 minutes for full color development

Step5: Measure the absorbance of iron-ferrozine complex

Step6: Determine the concentration of ferrous iron in sample using standard curve

Reference:

1. Clesceri, L. S.; Greenberg, A. E.; Eaton, A. D. *Standard methods for the examination of water and wastewater, 20th Edition*; American Public Health Association, Washington, DC, **1999**, pp 450-455.

APPENDIX D

DATA SETS

Table D.1 Experimental data for batch kinetic test with 0.1 g/L pyrite.

	Hg Concentration (µmol/L)		pH	
Time (min)	Without salts	With salts	Without salts	With salts
0	5.27	5.25		
5	0.54	1.46	4.96	5.70
10	0.57	1.40	4.94	5.73
20	0.64	1.43	4.88	5.63
30	0.70	1.42	4.88	5.66
60	0.77	1.74	4.87	5.58
120	0.90	2.18	4.79	5.81
180	0.91	2.62	4.86	5.75
360	0.31	3.37	4.81	4.76
720	0.05	2.94	4.46	4.96
1440	0.01	1.02	4.56	4.64

Table D.2 Experimental data for batch kinetic test with 0.01 g/L pyrite.

	Hg Concentration (µmol/L)		pH	
Time (min)	Without salts	With salts	Without salts	With salts
0	5.50	5.56		
5	2.19	4.76	5.39	6.25
10	2.60	4.68	5.76	6.17
20	2.24	4.60	5.54	6.18
30	2.07	4.58	5.01	6.16
60	2.62	4.39	5.71	6.18
120	2.14	4.06	5.09	6.06
180	2.23	4.01	5.39	5.98
360	2.11	3.17	5.33	6.1
720	1.64	2.84	5.7	6.13
1440	0.98	1.93	5.28	6.09

Table D.3 Experimental data for batch mercury loading test without salts.

1 day		3 days		7 days	
Aqueous concentration (µmol/L)	q (µmol Hg/g FeS2)	Aqueous concentration (µmol/L)	q (µmol Hg/g FeS2)	Aqueous concentration (µmol/L)	q (µmol Hg/g FeS2)
0.01	52.59	0.23	50.48	0.07	52.02
0.00	105.76	0.26	102.95	0.23	103.20
1.19	251.82	1.21	251.67	0.97	253.95
20.91	318.25	17.54	352.18	14.00	387.39
70.54	349.38	60.89	446.04	52.11	533.64
172.58	383.71	151.50	594.86	143.58	673.78
275.04	413.97	256.32	601.40	234.02	824.16
374.80	471.07	350.39	715.50	332.23	896.83
437.68	369.67	400.33	743.48	383.69	909.63
485.01	423.82	458.88	685.39	441.18	862.03

Table D.4 pH for batch mercury loading test without salts.

Initial Hg concentration (µmol/L)	1 day	3 days	7 days
5.27	4.77	4.88	4.68
10.55	4.68	4.49	4.29
26.37	4.93	4.86	4.82
52.74	5.74	5.57	5.18
105.48	6.72	6.65	6.28
210.95	7.27	7.15	6.98
316.43	7.42	7.41	7.31
421.91	7.48	7.52	7.52
474.65	7.62	7.56	7.59
527.39	7.60	7.68	7.65

Table D.5 Experimental data for batch mercury loading test with 0.01 mol/L salts.

1 day		3 days		7 days	
Aqueous concentration (µmol/L)	q (µmol Hg/g FeS2)	Aqueous concentration (µmol/L)	q (µmol Hg/g FeS2)	Aqueous concentration (µmol/L)	q (µmol Hg/g FeS2)
3.27	19.78	0.69	45.61	0.13	51.20
0.81	96.83	0.20	103.02	0.08	104.16
3.75	224.82	2.52	237.30	2.04	241.94
23.88	285.86	20.88	316.01	17.86	346.11
74.84	300.99	72.12	328.33	66.67	382.68
177.55	323.35	171.71	381.90	173.65	362.29
277.03	377.90	278.71	361.32	267.66	471.61
381.16	386.03	380.90	388.82	376.70	430.64
438.17	340.64	428.25	440.08	427.90	443.38
481.11	435.95	482.71	420.17	488.04	366.67

Table D.6 pH for batch mercury loading test with 0.01 mol/L salts.

Initial Hg concentration (µmol/L)	1 day	3 days	7 days
5.25	5.32	4.88	4.72
10.49	5.15	4.91	4.64
26.24	5.41	5.48	5.43
52.47	5.99	5.91	5.85
104.94	6.51	6.40	6.38
209.88	6.91	6.86	7.01
314.82	7.18	7.13	7.22
419.76	7.38	7.35	7.44
472.24	7.48	7.42	7.53
524.71	7.54	7.49	7.57

Table D.7 Experimental data for batch mercury loading test with 5 mg/L HAs.

1 day		3 days		7 days	
Aqueous concentration (µmol/L)	q (µmol Hg/g FeS2)	Aqueous concentration (µmol/L)	q (µmol Hg/g FeS2)	Aqueous concentration (µmol/L)	q (µmol Hg/g FeS2)
2.08	29.29	3.20	18.08	3.34	16.66
0.70	93.11	0.57	94.45	0.38	96.27
4.89	201.39	2.52	225.08	1.53	234.97
27.17	228.82	19.27	307.90	18.97	310.87
76.14	239.75	65.29	348.22	62.54	375.73
173.37	268.55	157.81	424.13	161.50	387.24
270.52	298.08	257.49	428.37	258.42	419.08
374.31	261.29	354.82	456.22	357.43	430.11
414.50	359.97	402.45	480.49	407.94	425.59

Table D.8 pH for batch mercury loading test with 5 mg/L HAs.

Initial Hg concentration (µmol/L)	1 day	3 days	7 days
5.01	5.70	4.62	4.18
10.01	5.72	5.08	4.42
25.03	5.85	5.23	4.53
50.06	6.39	5.95	5.54
100.11	6.88	6.62	6.11
200.22	7.20	7.04	6.40
300.33	7.31	7.16	6.71
400.44	7.46	7.30	6.90
450.50	7.53	7.37	6.90

Table D.9 Experimental data for batch mercury loading test with 10 mg/L HAs.

1 day		3 days		7 days	
Aqueous concentration (µmol/L)	q (µmol Hg/g FeS2)	Aqueous concentration (µmol/L)	q (µmol Hg/g FeS2)	Aqueous concentration (µmol/L)	q (µmol Hg/g FeS2)
2.47	25.40	3.79	12.11	3.94	10.66
1.25	87.57	0.94	90.76	1.82	81.88
5.88	191.44	3.03	220.00	2.43	225.93
26.54	235.12	17.71	323.44	16.45	336.07
74.47	256.37	60.26	398.47	59.83	402.76
167.19	330.33	151.43	487.86	153.53	466.93
268.38	319.52	256.47	438.65	259.07	412.59
371.67	287.68	347.97	524.74	350.53	499.14
422.67	278.26	393.35	571.50	416.17	343.30

Table D.10 pH for batch mercury loading test with 10 mg/L HAs.

Initial Hg concentration (µmol/L)	1 day	3 days	7 days
5.01	6.77	4.99	4.51
10.01	6.60	5.40	4.90
25.03	6.52	5.77	5.40
50.06	6.52	6.18	5.54
100.11	6.86	6.57	6.23
200.22	7.13	6.92	6.59
300.33	7.30	7.18	6.80
400.44	7.50	7.29	6.96
450.50	7.52	7.26	7.02

Table D.11 Experimental data for batch mercury loading test with 20 mg/L HAs.

1 day		3 days		7 days	
Aqueous concentration (µmol/L)	q (µmol Hg/g FeS2)	Aqueous concentration (µmol/L)	q (µmol Hg/g FeS2)	Aqueous concentration (µmol/L)	q (µmol Hg/g FeS2)
3.91	10.58	4.53	4.34	3.99	9.83
3.15	67.86	5.66	42.82	6.82	31.15
5.76	190.81	4.57	202.74	3.85	209.93
25.10	245.88	22.06	276.32	17.92	317.75
73.88	255.07	65.48	339.04	57.64	417.42
172.80	259.62	169.25	295.10	149.64	491.25
269.30	288.51	269.71	284.33	247.00	511.49
371.71	258.25	368.61	289.17	347.25	502.82
419.83	273.93	418.16	290.57	396.75	504.74

Table D.12 pH for batch mercury loading test with 20 mg/L HAs.

Initial Hg concentration (µmol/L)	1 day	3 days	7 days
4.97	6.12	4.42	4.33
9.94	6.32	5.11	4.38
24.85	6.61	5.99	6.39
49.69	6.95	6.41	6.53
99.38	7.27	6.83	6.98
198.76	7.60	7.12	7.30
298.15	7.78	7.29	7.52
397.53	7.74	7.36	7.59
447.22	7.91	7.43	7.69

Table D.13 Experimental data for column solubility test.

Average time (min)	Effluent Fe Concentration (mg/L)		
	pH 5.10	pH 6.98	pH 8.90
15	2.82	1.65	2.17
25	2.66	1.67	2.03
35	2.49	1.67	2.02
45	2.38	1.68	2
55	2.28	1.68	1.95
65	2.14	1.64	1.92
75	2.16	1.66	1.92
85	2.13	1.58	1.84
95	2.09	1.68	1.8
105	2.04	1.59	1.75
115	1.94	1.55	1.69
125	1.93	1.53	1.65
135	1.91	1.51	1.61
145	1.85	1.48	1.57
155	1.8	1.45	1.55
165	1.77	1.51	1.49
175	1.73	1.45	1.45

Table D.14 Experimental data for column tests at pH 5.

Average time (min)	Ct/C0*100 %	Average time (min)	pH	Filtrate	
95	0	95	4.36	Average time(min)	Ct/C0*100%
195	0	195	4.44	895	21.92
295	0	295	4.48	945	36.55
395	0	395	4.52	995	50.94
495	0	495	4.54	1045	58.66
595	0	595	4.58	1245	70.78
695	0	695	4.50	1495	79.97
745	0	745	4.48	1795	86.66
795	0	795	4.44	2095	91.94
845	5.53	845	4.44		

Table D.14 Continued.

Average time (min)	Ct/C0*100 %	Average time (min)	pH	Filtrate	
895	19.5	895	4.56		
945	37.4	945	4.56		
995	49.44	995	4.6		
1045	62.87	1045	4.62		
1095	67.29	1095	4.55		
1145	70.06	1145	4.63		
1195	73.52	1195	4.67		
1245	77.17	1245	4.75		
1295	80.81	1295	4.74		
1345	80.29	1345	4.75		
1395	84.16	1395	4.79		
1445	85.51	1445	4.93		
1495	90.33	1495	4.95		
1545	90.33	1545	4.94		
1595	91.2	1595	4.92		
1645	92.85	1645	4.89		
1695	92.17	1695	4.94		
1745	92.63	1745	4.95		
1795	95.66	1795	5.01		
1845	95.12	1845	5.03		
1895	96.71	1895	4.97		
1945	98.46	1945	5.01		
1995	97.07	1995	4.98		
2045	98.04	2045	5.01		
2095	98.04	2095	5.07		
2145	100.24	2145	5		

Table D.15 Experimental data for column tests at pH 7.

Average time (min)	Ct/C0*100%	Average time (min)	pH	Filtrate	
95	0	95	4.12	Average time(min)	Ct/C0*100%
195	0	195	4.24	795	0.00
295	0	295	4.32	895	0.00
395	0	395	4.4	995	14.90
495	0	495	4.44	1095	25.90
595	0	595	4.49	1195	35.69
695	0	695	4.53	1345	47.41
795	1.56	745	4.56	1495	56.15
895	12.68	795	4.59	1645	65.28
995	28.93	845	4.62	1845	61.76
1095	40.96	895	4.7	2295	69.76
1145	41.63	945	4.82	2695	72.75
1195	51.56	995	4.89		
1245	51.4	1045	5.02		
1295	58.69	1095	5.53		
1345	61.3	1145	5.32		
1405	65.8	1195	5.39		
1445	68.57	1245	5.53		
1495	71.56	1295	5.85		
1545	75.75	1345	5.83		
1595	78.04	1405	5.95		
1645	80.66	1445	5.89		
1695	82.4	1495	5.92		
1745	86.84	1545	5.88		
1795	86.24	1595	6.01		
1845	88.64	1645	6.06		
1895	86.3	1695	6.07		
1945	88.46	1745	6.06		
1995	88.43	1795	6.09		
2045	88.95	1845	6.11		
2095	89.42	1895	6		
2145	91.4	1945	6.07		
2195	91.59	1995	6.09		

Table D.15 Continued.

Average time (min)	Ct/C0*100%	Average time (min)	pH	Filtrate	
2245	90.68	2045	6.1		
2295	96.39	2095	6.11		
2345	95.53	2145	6.12		
2395	95.53	2195	6.14		
2445	97.28	2245	6.15		
2495	96.43	2295	6.21		
2545	98.24	2345	6.14		
2595	95.65	2395	6.14		
2645	95.6	2445	6.08		
2695	98.59	2495	6.12		
2715	98.36	2545	6.08		
		2595	6.14		
		2645	6.17		
		2695	6.16		
		2715	6.14		

Table D.16 Experimental data for column tests at pH 9.

Average time (min)	Ct/C0*100%	Average time (min)	pH	Filtrate	
95	0	95	4.1	Average time(min)	Ct/C0*100%
195	0	195	4.18	1095	9.06
295	0	295	4.27	1245	20.05
395	0	395	4.27	1445	32.37
495	0	495	4.36	1695	39.55
595	0	595	4.48	1995	49.62
695	0	695	4.57	2295	57.92
795	0	745	4.61	2545	65.69
895	0	795	4.66	2695	63.69
995	1.17	845	4.81		
1045	1.49	895	4.68		
1095	9.95	945	5.06		

Table D.16 Continued.

Average time (min)	Ct/C0*100%	Average time (min)	pH	Filtrate	
1145	12.5	995	5.23		
1195	18.22	1045	5.47		
1245	21.87	1095	5.72		
1295	27.62	1145	6.01		
1345	28.34	1195	5.97		
1395	34.22	1245	6		
1445	36.73	1295	6.07		
1495	40.76	1345	6.13		
1545	42.74	1395	6.24		
1595	44.54	1445	6.21		
1645	45.03	1495	6.27		
1695	48.51	1545	6.2		
1745	48.99	1595	6.2		
1795	50.5	1645	6.29		
1845	51.29	1695	6.29		
1895	55.2	1745	6.29		
1945	56.25	1795	6.36		
1995	59.71	1845	6.38		
2045	58.8	1895	6.35		
2095	58.23	1945	6.36		
2145	59.75	1995	6.47		
2195	61.45	2045	6.46		
2245	61.9	2095	6.4		
2295	64.3	2145	6.44		
2345	65.32	2195	6.49		
2395	63.69	2245	6.52		
2445	64.3	2295	6.42		
2495	70.67	2345	6.4		
2545	70.81	2395	6.42		
2595	74.53	2445	6.51		
2645	72.41	2495	6.45		
2695	78.46	2545	6.43		
2725	75.89	2595	6.46		
		2645	6.43		

Table D.16 Continued.

Average time (min)	Ct/C0*100%	Average time (min)	pH	Filtrate	
		2695	6.44		
		2725	6.45		

Table D.17 Experimental data for column tests at pH 7 with low HRT.

Average time (min)	Ct/C0*100%	Average time (min)	pH	Filtrate	
57	0	57	4.5	Average time(min)	Ct/C0*100%
117	0	117	4.56	417	17.84
177	0	177	4.6	477	40.96
237	0	237	4.63	507	52.48
297	0	297	4.7	567	61.31
357	0	357	4.74	657	73.13
417	14.31	417	4.72	747	76.29
447	27.82	447	4.72	867	78.76
477	37.77	477	4.78	1317	86.71
507	50.42	507	4.82		
537	59.37	537	4.88		
567	66.21	567	5.01		
597	70.52	597	5		
627	77.19	627	4.91		
657	77.64	657	5.18		
687	83.36	687	5.2		
717	79.75	717	5.27		
747	83.89	747	5.36		
777	81.33	777	5.46		
807	82.49	807	5.51		
837	86.82	837	5.56		
867	89.30	867	5.65		
897	89.30	897	5.64		
927	93.03	927	5.74		
957	90.62	957	5.79		

Table D.17 Continued.

Average time (min)	Ct/C0*100%	Average time (min)	pH	Filtrate	
987	93.37	987	5.81		
1017	92.46	1017	5.73		
1077	94.09	1077	5.92		
1137	97.79	1137	5.92		
1197	96.59	1197	6.01		
1257	90.77	1257	6.04		
1317	99.49	1317	6.1		
1377	97.74	1377	6.08		

Table D.18 Experimental data for column tests at pH 7 with 0.01 mol/L salts.

Average time (min)	Ct/C0*100%	Average time (min)	pH	Filtrate	
95	0	95	5.06	Average time(min)	Ct/C0*100%
195	0	195	5.28	1045	21.22
295	0	295	5.42	1095	37.70
395	0	395	5.36	1145	50.58
495	0	495	5.38	1245	62.43
595	0	595	5.44	1395	70.20
695	0	695	5.53	1695	78.50
795	0.16	795	5.6	2195	83.21
895	0.98	895	5.78	2695	85.01
995	5.65	995	5.89		
1045	27.73	1045	6.02		
1095	43.76	1095	6.13		
1145	58.73	1145	6.12		
1195	68.44	1195	6.15		
1245	76.17	1245	6.19		
1295	80.51	1295	6.16		
1345	83.71	1345	6.13		
1395	86.47	1395	6.11		
1445	87.57	1445	6.26		

Table D.18 Continued.

Average time (min)	Ct/C0*100%	Average time (min)	pH	Filtrate	
1495	89.37	1495	6.19		
1545	89.00	1545	6.25		
1595	90.73	1595	6.23		
1645	92.10	1645	6.2		
1695	94.60	1695	6.22		
1745	94.63	1745	6.16		
1795	92.97	1795	6.24		
1845	94.53	1845	6.26		
1895	96.31	1895	6.26		
1945	95.29	1945	6.21		
1995	95.40	1995	6.25		
2095	96.51	2095	6.28		
2195	97.12	2195	6.26		
2295	98.85	2295	6.27		
2395	99.50	2395	6.16		
2495	101.99	2495	6.32		
2695	102.15	2695	6.26		

Table D.19 Experimental data for column tests with 10 mg/L HAs.

Average time (min)	Ct/C0*100%	Average time (min)	pH	Filtrate	
95	0	95	4.52	Average time(min)	Ct/C0*100%
195	2.80	195	4.6	395	1.27
295	11.14	295	4.65	895	6.41
395	14.94	395	4.78	1095	21.14
495	16.07	495	4.69	1395	35.18
595	16.59	595	4.77	1795	43.84
695	16.57	695	4.78	2195	45.25
795	18.59	795	4.79	2595	42.63
895	24.22	895	4.89	2845	47.04
995	33.60	995	4.85		

Table D.19 Continued.

Average time (min)	Ct/C0*100%	Average time (min)	pH	Filtrate	
1095	43.81	1095	4.97		
1195	51.05	1195	4.93		
1295	58.95	1295	4.91		
1395	62.08	1395	5		
1495	68.34	1495	4.97		
1595	74.39	1595	4.92		
1695	75.28	1695	4.97		
1795	77.53	1795	5.07		
1895	77.06	1895	4.97		
1995	80.62	1995	4.96		
2095	79.69	2095	4.97		
2195	81.89	2195	5.08		
2295	83.38	2295	5.05		
2395	81.42	2395	4.93		
2495	83.82	2495	5.08		
2595	85.49	2595	5.09		
2695	87.24	2695	4.99		
2795	85.23	2795	5.03		
2845	77.63	2845	5		

Table D.20 Experimental data for column tests with 20 mg/L HAs.

Average time (min)	Ct/C0*100%	Average time (min)	pH	Filtrate	
45	1.63	95	4.55	Average time(min)	Ct/C0*100%
95	20.07	195	4.65	95	0
195	29.18	295	4.77	495	0
295	31.18	395	4.78	995	4.92
395	29.07	495	4.76	1395	5.77
495	32.42	595	4.73	1895	4.28
595	35.09	695	4.71	2195	3.15
695	35.92	795	4.86	2495	5.41

Table D.20 Continued.

Average time (min)	Ct/C0*100%	Average time (min)	pH	Filtrate	
795	37.14	895	4.91	2795	4.47
895	39.89	995	4.85		
995	42.03	1095	4.84		
1095	42.90	1195	4.87		
1195	45.74	1295	4.81		
1295	48.55	1395	4.87		
1395	50.34	1495	4.86		
1495	53.06	1595	5.01		
1595	47.32	1695	4.97		
1695	50.02	1795	4.87		
1795	51.19	1895	4.98		
1895	53.12	1995	4.92		
1995	53.96	2095	4.89		
2095	55.24	2195	4.98		
2195	57.15	2295	4.94		
2295	59.51	2395	4.91		
2395	60.22	2495	4.56		
2495	69.72	2595	4.91		
2595	68.42	2695	4.95		
2695	68.56	2795	4.95		
2795	69.14	2845	4.93		
2845	68.74				

Table D.21 Experimental data for column tests at pH 7 with polymer/pyrite-coated sand.

Average time (min)	Ct/C0*100%	Average time (min)	pH	Filtrate	
95	0.00	95	5.50	Average time(min)	Ct/C0*100%
195	0.00	195	5.73	1695	10.26
295	0.00	295	5.89	1795	20.16
395	0.00	395	5.90	1895	27.12
495	0.00	495	5.96	1995	38.36
595	0.00	595	5.97		
695	0.00	695	5.97		
795	0.00	795	6.00		
895	0.00	895	5.99		
995	0.00	995	5.94		
1095	0.00	1095	6.16		
1195	0.00	1195	6.15		
1295	0.00	1295	6.31		
1395	0.00	1395	6.36		
1495	3.63	1495	6.35		
1595	7.80	1595	6.37		
1695	16.39	1695	6.49		
1745	21.64	1745	6.28		
1795	26.65	1795	6.46		
1895	34.89	1895	6.46		
1995	48.93	1995	6.46		
2045	50.74	2045	6.30		
2095	57.69	2095	6.41		
2195	67.43	2195	6.38		
2295	72.40	2295	6.34		
2395	76.54	2395	6.40		
2495	80.41	2495	6.38		
2595	83.06	2595	6.43		
2645	84.86	2645	6.41		

Table D.22 Experimental data for column tests at pH 7 with polymer/pyrite-coated sand in the presence of 0.01 mol/L salts.

Average time (min)	Ct/C0*100%	Average time (min)	pH	Filtrate	
95	0.00	95	4.80	Average time(min)	Ct/C0*100%
195	0.00	195	5.00	1695	21.61
295	0.00	295	5.08	1995	48.02
395	0.00	395	5.08	2395	63.03
495	0.00	495	5.15	2695	69.80
595	0.00	595	5.14		
695	0.00	695	5.15		
795	0.00	795	5.22		
895	0.00	895	5.26		
995	0.00	995	5.37		
1095	0.00	1095	5.32		
1195	0.00	1195	5.43		
1295	0.00	1295	5.47		
1395	0.00	1395	5.55		
1495	0.15	1495	5.61		
1595	11.59	1595	5.69		
1695	26.76	1695	5.66		
1795	44.34	1795	5.71		
1895	54.28	1895	5.73		
1995	60.91	1995	5.76		
2095	66.10	2095	5.73		
2195	75.46	2195	5.78		
2295	77.92	2295	5.80		
2395	76.52	2395	5.79		
2495	81.26	2495	5.81		
2595	84.15	2595	5.81		
2695	85.82	2695	5.81		

Table D.23 Experimental data for column tests at pH 7 with polymer/pyrite-coated sand in the presence of 10 mg/L HAs.

Average time (min)	Ct/C0*100%	Average time (min)	pH	Filtrate	
95	30.37	95	5.26	Average time(min)	Ct/C0*100%
195	32.51	195	5.50	795	8.46
295	32.11	295	5.57	1595	9.90
395	34.58	395	5.66	2395	10.17
495	35.39	495	5.70	2695	10.27
595	36.32	595	5.73		
695	36.33	695	5.82		
795	37.84	795	5.83		
895	40.21	895	5.87		
995	41.81	995	5.90		
1095	43.68	1095	5.91		
1195	46.24	1195	5.91		
1295	48.09	1295	5.94		
1395	50.50	1395	5.98		
1495	50.93	1495	5.89		
1595	53.01	1595	5.87		
1695	54.67	1695	5.90		
1795	55.73	1795	5.89		
1895	58.46	1895	5.92		
1995	60.10	1995	5.95		
2095	62.29	2095	5.97		
2195	62.32	2195	5.99		
2295	65.94	2295	5.97		
2395	66.25	2395	5.99		
2495	67.17	2495	6.01		
2595	70.80	2595	6.07		
2695	71.72	2695	6.06		
2745	72.28	2745	6.10		